This document is downloaded from DR-NTU (https://dr.ntu.edu.sg)
Nanyang Technological University, Singapore.

A study of dilute nitride-antimonide semiconductors for near infrared optoelectronics devices

Tan, Kian Hua

2010

Tan, K. H. (2010). A study of dilute nitride-antimonide semiconductors for near infrared optoelectronics devices. Doctoral thesis, Nanyang Technological University, Singapore.

https://hdl.handle.net/10356/42311

https://doi.org/10.32657/10356/42311

Downloaded on 21 Aug 2022 01:48:54 SGT

ATTENTION: The Singapore Copyright Act applies to the use of this document. Nanyang Technological University Library

.

A STUDY OF DILUTE NITRIDE-ANTIMONIDE SEMICONDUCTORS FOR NEAR INFRARED OPTOELECTRONICS DEVICES

TAN KIAN HUA

School of Electrical and Electronic Engineering

A thesis submitted to the Nanyang Technological University

in partial fulfillment of the requirement for the degree of
Doctor of Philosophy

2010

ATTENTION: The Singapore Copyright Act applies to the use of this document. Nanyang Technological University Library

Statement of Originality

I hereby certify that the work embodied in this thesis is the result of original research and has not been submitted for a higher degree to any other University or Institution.

Date

Tan Kian Hua

ATTENTION: The Singapore Copyright Act applies to the use of this document. Nanyang Technological University Library

Acknowledgement

I would like to express my greatest appreciation to my supervisor, Prof. Yoon Soon Fatt, for giving me this precious opportunity to pursue graduate study in the field of III-V compound semiconductor optoelectronic. I would also like to sincerely express my gratitude for the group members: Dr. Loke Wan Khai, Dr. Satrio Wicaksono, Dr. Ng Tien Khee and Mr. Xu Zhe for their friendship and unselfish cooperation. Dr. Loke's help in fabricating and measuring 1.55µm GaNAsSb-based WGPD is greatly appreciated.

I would also like to take this opportunity to thank all collaborators in this project. Special thank to Dr. Andreas Stöhr, Mr. Sascha Fedderwitz and their group members from University of Duisburg-Essen Germany, for their efforts in helping me to measure RF performance, eye diagram and bit error rate of photodetectors. Their hospitality during my brief stay in Duisburg for the photodetector measurement is also greatly appreciated.

Furthermore, the collaboration work with THALES@NTU and IEMN, Lille has provided valuable results for the optical waveguide. Special thanks to Prof. Didier Decoster and his group members, Naima Saadsaoud and Dr. Malek Zegaoui for their efforts in GaNAsSb waveguide fabrication and measurement using the

ATTENTION: The Singapore Copyright Act applies to the use of this document. Nanyang Technological University Library

samples grown using MBE by me in NTU. Further thanks to Prof. Decoster for his assist in my analysis of waveguide performance.

Special thanks to Prof. Charlotte Tripon-Canseliet of Pierre and Marie Curie University for her efforts in measuring the performance of photoconductive switch using the samples grown using MBE by me in NTU. My sincerest gratitude is extended to Dr. Jean Chazelas of THALES Airborne Systems, Dr. Jean Pierre Vilcot for their support in my experiments. The partial financial support of the European Commission within the European Network of Excellence ISIS under grant no. 26592 is duly appreciated.

Moreover, I would like to thank the technicians of Clean Room and Characterization Laboratory, particularly, Ms. Seet Lye Ping, Mr. Mohamad Shamsul bin Mohamad and Mr. Muhammad Fauzi bin Abdullah for their efforts in managing the laboratory.

Finally, I would like my appreciation to the love of my life, my wife, Re Har for her support and patience.

ATTENTION: The Singapore Copyright Act applies to the use of this document. Nanyang Technological University Library

Table of content

Acknowledgement i

Table of content iii

Summary v

List of figure captions viii

Author's publications from this research xix

Chapter 1 Introduction 1

1.1 Background 1
1.2 Motivation and objective 6
1.2.1 GaNAsSb-based p-i-n photodetector 6
1.2.2 GaNAsSb-based photoconductive switch 11
1.2.3 GaNAsSb optical waveguide 13
1.3 Major contributions of the thesis 15
1.4 Organization of thesis 18

Chapter 2 Bandgap of GaNAsSb and device principles 21

2.1 Bandgap of GaNAsSb 21
2.2 Device principles 25
2.2.1 p-i-n photodetector 25
2.2.2 Uni-traveling carrier photodetector 31
2.2.3 Photoconductive switch 33
2.2.4 Semiconductor-based optical waveguide 36

Chapter 3 Growth and characterization of GaNAsSb 40

3.1 Growth of GaNAsSb material using molecular beam epitaxy system 40
3.2 Determination of N and Sb content in GaNAsSb using x-ray diffraction 44
3.3 Modification of the nitrogen RF plasma source 47

Chapter 4 GaNAsSb-based p-i-n photodetector 52

4.1 Photodetector responsivity 52
4.1.1 Introduction 52
4.1.2 Growth of GaNAsSb-based p-i-n photodetectors 53
4.1.3 Results of Photoresponsivity measurement 54
4.1.4 Photocurrent multiplication in GaNAsSb-based p-i-n photodetectors 56
4.1.5 Carrier avalanche process at low electric field 60
4.1.6 Summary 62
4.2 High frequency performance of the photodetectors 63
4.2.1 Introduction 63
4.2.2 Growth and fabrication of GaNAsSb-based p-i-n photodetectors 63
4.2.3 Spectral response and dark current density 66

ATTENTION: The Singapore Copyright Act applies to the use of this document. Nanyang Technological University Library

4.2.4 Temporal response and 3dB cutoff frequency 68
4.2.5 Summary 71
4.3 Fiber optic data transmission 71
4.3.1 Introduction 71
4.3.2 Frequency response measurement using 1.3μm laser 72
4.3.3 Eye diagram and bit-error rate at 5Gb/s 73
4.3.4 Summary 78
4.4 Extension of photo-response to 1.55μm 79
4.4.1 Introduction 79
4.4.2 Growth and fabrication of GaNAsSb-based waveguide photodetector 80
4.4.3 X-ray diffraction characterization 81
4.4.4 Dark current density 82
4.4.5 Spectral response and photoresponsivity at 1.55μm 83
4.4.6 Summary 86
Chapter 5 GaNAsSb-based uni-traveling carrier photodetector 87
5.1 Introduction 87
5.2 Growth and fabrication of GaNAsSb-based UTC photodetectors 88
5.3 Dark current density 90
5.4 Temporal response and 3dB cutoff frequency 92
5.5 Bandwidth limiting factor of GaNAsSb-based UTC photodetectors 98
5.6 Eye diagram and bit-error rate 100
5.7 Summary 104
Chapter 6 GaNAsSb-based photoconductive switch 105
6.1 Introduction 105
6.2 Growth of GaNAsSb-based photoconductive switch 106
6.3 Photoluminescence and refractive index measurement 107
6.4 Switch fabrication and resistivity 110
6.5 Pulsed response measurement and carrier lifetime 113
6.6 Microwave switching performance 116
6.7 Improvement of ON/OFF ratio at 1.55μm 120
6.8 Summary 128
Chapter 7 GaAs/GaNAsSb/GaAs 1.55μm optical waveguide system 129
7.1 Introduction 129
7.2 Growth and fabrication of waveguide 130
7.3 Near-field optical intensity distribution pattern measurement 131
7.4 Propagation loss 133
7.5 Summary 138
Chapter 8 Conclusions and recommendations 139
8.1 Conclusions 139
8.2 Recommendations for future research 144
Bibliography 147

ATTENTION: The Singapore Copyright Act applies to the use of this document. Nanyang Technological University Library

Summary

In this thesis, GaNAsSb-based optoelectronic device structures were grown using a solid-source molecular beam epitaxy (MBE) system in conjunction with a radio frequency (RF) plasma N source and Sb valved-cracker source. To reduce the nitrogen plasma induced defects, an ion deflection plate has been installed.

Four p-i-n GaNAsSb-based photodetectors have been grown using MBE for photoresponsivity measurement. The devices have shown photo-response up to a wavelength of 1380nm in the spectral response. The device with GaNAsSb layer grown at 350°C shows the highest DC responsivity of 12A/W. This high value of responsivity indicates a carrier avalanche process in the devices, even at reverse bias as low as 1V. In temporal response measurement, the device shows a pulse minimum full-width at half maximum (FWHM) of 40.5ps, corresponding to 3dB cutoff frequency of 4.5GHz. This frequency response is the highest ever reported for dilute nitride-based p-i-n photodetector. Furthermore, high speed data transmission at 5Gb/s has been demonstrated using this GaNAsSb-based p-i-n photodetector at wavelength of 1300nm.

To further extend the photo-response from 1380nm to 1600nm, a GaNAsSb-based p-i-n waveguide photodetector has been grown using the molecular beam epitaxy. The device consists of a strained GaNAsSb photon-absorption layer, which has

ATTENTION: The Singapore Copyright Act applies to the use of this document. Nanyang Technological University Library

3.5% of N and 18% of Sb. The device shows photo-response up to at least 1600nm in the spectral response. Moreover, photoresponsivity of 0.29A/W of the device at 1550nm was demonstrated.

A GaNAsSb-based uni-traveling carrier (UTC) photodetector was grown using MBE to further improve the high frequency performance of the photodetector. The UTC photodetector has a short response time for hole carriers, leading to increase in 3dB cutoff frequency of the photodetector The GaNAsSb-based UTC photodetector has shown a 3dB cutoff frequency value of 14GHz. Fiber optic data transmission over a 10km fiber at a data rate of up to 12.5Gb/s has been successfully demonstrated with this device.

The high electrical resistance and short carrier lifetimes of the GaNAsSb material make it an ideal candidate for the active material in a photoconductive switch. The use of GaNAsSb-based photoconductive switch in microwave switching application has been demonstrated. The switch exhibits pulsed response with FWHM of 30ps and photo-response up to 1.6µm. The switch shows an ON/OFF ratio of 11dB at 1GHz and response up to 15GHz in microwave switching application at the wavelength of 790nm.

The bandgap of the GaNAsSb was reduced to ~0.8eV to increase the efficiency of the photon-absorption at wavelength of 1.55µm. The GaNAsSb-based

ATTENTION: The Singapore Copyright Act applies to the use of this document. Nanyang Technological University Library

photoconductive switch with a GaNAsSb layer, which has the bandgap energy of 0.8eV, shows an ON/OFF ratio of 9dB at the wavelength of 1.55μm. Further analysis suggests that the high contact resistance limits the performance of the GaNAsSb-based photoconductive switch.

A 1.55μm GaAs/GaNAsSb/GaAs optical waveguide grown by molecular beam epitaxy as an alternative to the AlGaAs/GaAs system has been demonstrated. The GaNAsSb layer has a refractive index value of 3.42 at wavelength of 1.55μm. The propagation loss measured using the Fabry-Perot resonance method was found to be affected by nitrogen-related defect absorption.

ATTENTION: The Singapore Copyright Act applies to the use of this document. Nanyang Technological University Library

List of figure captions

Figure 1.1 Attenuation of light traveling in silica fiber at different wavelengths [1]. 2

Figure 1.2 The change of refractive index (n) and group refractive index (n_g) in the silica at different wavelengths [2]. 3

Figure 1.3 Transmission distances of 850nm, 1310nm and 1550nm lasers in optical fiber at different bit rates [3]. 4

Figure 2.1 Band diagram illustration of formation of two energy levels E_- and E_+, by interaction between the nitrogen state (E^N) and the GaAs conduction band (E^C) [54]. 22

Figure 2.2 Calculated bandgap energy of GaNAs as function of nitrogen fraction, x, (a) from the BAC model (solid curve), (b) using the variable bowing parameter (dashed curve), (c) using a constant bowing parameter (dotted curve) and (d) experimental data (solid circle) [54]. 23

Figure 2.3 Bandgap energy of GaNAsSb material system which is lattice-matched to GaAs *vs.* nitrogen composition. 24

Figure 2.4 Schematic diagram of a p-i-n photodetector. 25

ATTENTION: The Singapore Copyright Act applies to the use of this document. Nanyang Technological University Library

Figure 2.5 Band diagram of a p-i-n photodetector under reverse biased condition. 27

Figure 2.6 Absorption coefficients of several semiconductors at different wavelengths. Adopted from [56].. 28

Figure 2.7 Photoresponsivity of different photodetectors materials. 30

Figure 2.8 Schematic band diagram of uni-traveling carrier photodetector...... 33

Figure 2.9 Schematic diagram of a photoconductive switch. *l* and *w* are the width and length of the semiconductor, respectively. *d* and d_o are the height of the semiconductor and optical penetration depth, respectively. 34

Figure 2.10 Schematic diagram of a planar type of photoconductive switch. 36

Figure 2.11 Different types of semiconductor channel optical waveguides. 38

Figure 3.1 Schematic diagram of a typical Solid source molecular beam epitaxy system equipped with RF plasma N source, As and Sb valved-cracker cells. 41

Figure 3.2 The product distribution of an antimony cracker cell is shown as function of cracker zone temperature. Experimentally measured values are indicated by solid symbols: Sb (triangles), Sb_2 (bow ties) and Sb_4 (circles) [61]... 44

ATTENTION: The Singapore Copyright Act applies to the use of this document. Nanyang Technological University Library

Figure 3.3 Schematic diagram of calibration sample used to determine concentration of N and Sb atoms in GaNAsSb material................. 46

Figure 3.4 XRD (004) rocking curve of calibration sample. The red simulation curve is used to determine the concentration of Sb and N in the material... 46

Figure 3.5 Schematic diagram of the ion deflection plates. Nitrogen ions are deflected towards the negatively biased plate................................ 48

Figure 3.6 PL spectra (5K) of GaNAs samples under different bias voltages. . 49

Figure 3.7 Plot of PL intensity at 5K (■) and at room temperature (•) of GaNAs samples *vs.* deflection plate bias voltages.......................... 50

Figure 3.8 XRD rocking curve of GaNAs samples grown under different bias voltages. 51

Figure 4.1 Schematic diagram of GaNAsSb-based p-i-n photodetector structure.. 54

Figure 4.2 (a) Spectral response of devices with i-GaNAsSb layer grown at 350°C, 400°C, 440°C and 480°C, measured at reverse bias voltage of 3V. (b) Plot of photoresponsivity *vs.* reverse bias for devices with i-GaNAsSb layer grown at 350°C, 400°C, 440°C and 480°C measured at 1300nm. 55

ATTENTION: The Singapore Copyright Act applies to the use of this document. Nanyang Technological University Library

Figure 4.3 Unintentional doping concentration in GaNAsSb at different growth temperatures.. 57

Figure 4.4 Plot of multiplication factor *M* as function of reverse bias voltage measured at 1300nm for devices with i-GaNAsSb layer grown at 350°C, 400°C, 440°C and 480°C... 58

Figure 4.5 Plot of multiplication factor *M* as function of average electric field measured at 1300nm for devices with i-GaNAsSb layer grown at 350°C, 400°C, 440°C and 480°C... 59

Figure 4.6 Cross section schematic diagram of the GaNAsSb-based p-i-n photodetector mesa structure. 63

Figure 4.7 (a) Optical micrographs of three fabricated GaNAsSb-based p-i-n photodetector with optical illumination window diameters of 10µm, 15µm and 40µm. (b) Scanning electron micrographs of a GaNAsSb photodetector with air-bridge metallization. ` 65

Figure 4.8 Relative spectral response of the GaNAsSb-based p-i-n photodetector... 66

Figure 4.9 Plot of dark current characteristic of the GaNAsSb-based p-i-n photodetector... 67

ATTENTION: The Singapore Copyright Act applies to the use of this document. Nanyang Technological University Library

Figure 4.10 (a) Normalized temporal response of GaNAsSb-based p-i-n photodetectors of different diameters at -8V applied bias and (b) normalized temporal response of a 10μm diameter GaNAsSb photodetector at different reverse biases. Insets show the corresponding normalized frequency responses derived by fast Fourier transform. 69

Figure 4.11 Experimental setup of the frequency response measurement. 72

Figure 4.12 Frequency response characteristic of the GaNAsSb-based p-i-n photodetector at 1.3μm wavelength at reverse bias of 12V. 73

Figure 4.13 Closed eye diagram of GaNAsSb-based photodetector with i-GaNAsSb layer grown at 440°C at the data rate of 300MHz 74

Figure 4.14 Plot of dark current density of the GaNAsSb-based photodetector with i-GaNAsSb layer grown at different temperatures *vs*. bias voltage. 75

Figure 4.15 Eye diagram of the output signal from a 1.3μm GaNAsSb-based p-i-n photodetector with 30μm illumination window diameter at data rate of 5Gb/s. 76

Figure 4.16 Dependence of the bit-error rate on the optical input power of the GaNAsSb-based p-i-n photodetector (30μm window diameter) at data rates of 2.5Gb/s and 5Gb/s, respectively. BER measurements were carried out at 1.3μm wavelength. 77

ATTENTION: The Singapore Copyright Act applies to the use of this document. Nanyang Technological University Library

Figure 4.17 Schematic diagram of a GaNAsSb-based waveguide photodetector. 80

Figure 4.18 X-ray diffraction (004) rocking curve of GaNAsSb layer with 3.5% of N and 18% of Sb. 81

Figure 4.19 X-ray reciprocal (224) space map of GaNAsSb-based p-i-n waveguide photodetector. S and L denote the GaAs substrate peak and GaNAsSb layer peak, respectively. 82

Figure 4.20 Current-voltage characteristics of a GaNAsSb-based p-i-n waveguide photodetector with 6.5µm ridge width and 500µm ridge length. 83

Figure 4.21 Normalized spectral response of GaNAsSb-based p-i-n waveguide photodetector with 6.5µm ridge width and 500µm ridge length. The data of top-illuminated photodetector is taken from Figure 4.2. 84

Figure 5.1 (a) Cross section schematic of a GaNAsSb-based UTC photodetector structure. (b) SEM photograph of a GaNAsSb-based UTC photodetector with an illumination window diameter of 25µm. 88

Figure 5.2 Schematic band diagram of a GaNAsSb-based UTC photodetector. 90

ATTENTION: The Singapore Copyright Act applies to the use of this document. Nanyang Technological University Library

Figure 5.3 Dark current characteristic of the GaNAsSb-based UTC photodetector. 91

Figure 5.4 Normalized temporal response of GaNAsSb-based UTC photodetectors of different diameters at 9V reverse bias. 93

Figure 5.5 Temporal response of the 10µm diameter GaNAsSb-based p-i-n photodetector and the 10µm GaNAsSb-based UTC photodetector. 94

Figure 5.6 Frequency response characterization of the GaNAsSb-based UTC photodetector measured using a 1.3µm laser. 94

Figure 5.7 Normalized temporal response at different reverse biases for GaNAsSb-based UTC photodetectors with (a) 10µm, (b) 25µm and (c) 40µm illumination window diameters. 97

Figure 5.8 Eye diagrams of the output signal from a 1.3µm GaNAsSb-based UTC photodetector with 25µm illumination window diameter at data rate of (a) 7.5Gb/s (b) 10.3125Gb/s and (c) 12.5Gb/s for the data transmission over a 10km single mode fiber.. 102

Figure 5.9 Bit-error rate *vs.* the optical input power at 1.3µm wavelength of the GaNAsSb-based UTC photodetector (25µm diameter) at data rates of 10.3125Gb/s and 12.5Gb/s for data transmission over a 10km single mode fiber. 103

ATTENTION: The Singapore Copyright Act applies to the use of this document. Nanyang Technological University Library

Figure 6.1 Schematic diagram of a GaNAsSb-based photoconductive switch structure... 107

Figure 6.2 n-k plot *vs.* wavelength of the GaNAsSb material from refractive index measurement. 108

Figure 6.3 Absorption coefficient derived from the extinction coefficient (k) data set. 108

Figure 6.4 PL spectrum at 4K of the GaNAsSb material. The dashed lines are two Gaussian peaks used to fit the spectrum. Band-to-band transition gives rise to the main PL peak at 0.875eV. The shoulder peak at 0.825eV is attributed to transitions related to defects. 109

Figure 6.5 Plot of electrical resistance of GaNAsSb *vs*. electrode gap. 110

Figure 6.6 Resistivity of the GaNAsSb at different laser powers. 111

Figure 6.7 Resistivity of the GaNAsSb at different laser excitation wavelengths. The laser power is 23mW. The squares represent the dark resistivity of the GaNAsSb. 112

Figure 6.8 Top view of sub-miniature version A (SMA) alumina carrier of the GaNAsSb-based photoconductive switch with gap of 2µm. 113

Figure 6.9 Pulsed response of GaNAsSb-based photoconductive switch at different laser excitation wavelengths. Inset shows carrier lifetimes of the GaNAsSb layer derived from pulsed measurement at different wavelengths...114

ATTENTION: The Singapore Copyright Act applies to the use of this document. Nanyang Technological University Library

Figure 6.10 Plot of ON/OFF ratio and RF insertion losses of the GaNAsSb-based photoconductive switch at different frequencies. 117

Figure 6.11 Plot of ON/OFF ratio of the GaNAsSb-based photoconductive switch at different frequencies under a 80mW laser excitation at 1.3µm. 119

Figure 6.12 Plot of ON/OFF ratio of the GaNAsSb-based photoconductive switch at different frequencies under a 80mW laser excitation at 1.55µm. 119

Figure 6.13 a) Schematic diagram of the GaNAsSb-based photoconductive switch structure. b) Optical microscope picture of the GaNAsSb-based photoconductive switch with different electrode shapes. 121

Figure 6.14 Schematic diagram of the switches with different electrode shapes. The electrode gap, a and the width of electrode, b are 1µm. 122

Figure 6.15 Plot of ON/OFF ratio of the GaNAsSb-based photoconductive switch with different electrode shapes as function of frequency. .. 123

Figure 6.16 Plot of ON/OFF ratio of the GaNAsSb-based photoconductive switch with linear tapered electrode and electrode gaps of 1µm, 2µm and 5µm as function of frequency. 124

ATTENTION: The Singapore Copyright Act applies to the use of this document. Nanyang Technological University Library

Figure 6.17 Plot of insertion loss of the GaNAsSb-based photoconductive switch with tapered electrode and electrode gaps of 1μm, 2μm and 5μm as function of frequency.. 125

Figure 6.18 Plot of insertion loss of the GaNAsSb-based photoconductive switch with tapered electrode and electrode gaps of 1μm, 2μm and 5μm as function of frequency at the low frequency range (<500MHz). 125

Figure 6.19 Equivalent circuit of a photoconductive switch. 126

Figure 6.20 Plot of the calculated insertion loss of a photoconductive switch at different switch resistances, R as a function of frequency............ 126

Figure 7.1 Cross section schematic of the GaAs/GaNAsSb/GaAs waveguide structure. The ridge widths of the waveguide are 4μm, 6.5μm and 8μm, respectively. The length of the waveguide is 2.1mm. 130

Figure 7.2 Schematic diagram of the experimental setup for the near-field optical intensity distribution pattern measurement....................... 131

Figure 7.3 Near-field optical intensity distribution pattern of the waveguides with (a) 4μm, (b) 6.5μm and (c) 8μm ridge widths, respectively.. 131

Figure 7.4 Near-field optical intensity distribution pattern of the waveguides with (a) 4μm, (b) 6.5μm and (c) 8μm ridge widths, respectively measured using an input laser with lower light intensity.. 132

ATTENTION: The Singapore Copyright Act applies to the use of this document. Nanyang Technological University Library

Figure 7.5 Schematic diagram of the experimental setup for the propagation loss measurement using the Fabry-Perot resonance. 133

Figure 7.6 Fabry Perot resonance results of GaAs/GaNAsSb/GaAs waveguides with ridge width of (a) 4µm, (b) 6.5µm and (c) 8µm, respectively. 134

ATTENTION: The Singapore Copyright Act applies to the use of this document. Nanyang Technological University Library

Author's publications from this research

Main author

1. **K. H. Tan**, S. F. Yoon, W. K. Loke, S. Wicaksono, K. L. Lew, A. Stohr, O. Ecin, A. Poloczek, A. Malcoci, and D. Jager, "High-speed picosecond pulse response GaNAsSb p-i-n photodetectors grown by rf plasma-assisted nitrogen molecular beam epitaxy," *Applied Physics Letters*, vol. 90, pp. 183515-1, 2007.

2. **K. H. Tan**, S. F. Yoon, W. K. Loke, S. Wicaksono, Z. Xu, T. K. Ng, K. L. Lew, N. Saadsaoud, M. Zegaoui, D. Decoster, and J. Chazelas, "1.55μm GaAs/GaNAsSb/GaAs optical waveguides grown by radio frequency nitrogen plasma-assisted molecular beam epitaxy," *Applied Physics Letters*, vol. 92, pp. 113513, 2008.

3. **K. H. Tan**, S. F. Yoon, W. K. Loke, S. Wicaksono, T. K. Ng, K. L. Lew, A. Stohr, S. Fedderwitz, M. Weiss, D. Jager, N. Saadsaoud, E. Dogheche, D. Decoster, and J. Chazelas, "High responsivity GaNAsSb p-i-n photodetectors at 1.3μm grown by radio-frequency nitrogen plasma-assisted molecular beam epitaxy," *Optics Express*, vol. 16, pp. 7720-7725, 2008.

4. **K.H. Tan**, S.F. Yoon, W.K. Loke, S. Wicaksono, C. Tripon-Canseliet, S. Faci, N. Saadsaoud, J. F. Lampin, D. Decoster and J. Chazelas, "GaNAsSb material for ultrafast microwave photoconductive switching application," *Applied Physics Letters*, vol. 93, pp. 063509, 2008

ATTENTION: The Singapore Copyright Act applies to the use of this document. Nanyang Technological University Library

5. **K. H. Tan**, S. F. Yoon, S. Fedderwitz, A. Stöhr, W. K. Loke, S. Wicaksono, T. K. Ng, M. Weiß, A. Poloczek, V. Rymanov, A .S. Patra, E. Tangdiongga and D. Jäger, “14GHz GaNAsSb uni-traveling carrier 1.3µm photodetectors grown by RF plasma-assisted nitrogen molecular beam epitaxy,” *IEEE Electron Device Letters*, vol. 30, pp. 590-592, 2009

Co-author

6. S. Fedderwitz, A. Stöhr, S.F. Yoon, **K.H. Tan,** M. Weiß, A. Poloczek, D. Jäger, W.K. Loke, and S. Wicaksono, “Multi-Gigabit 1.3µm GaNAsSb/GaAs Photodetectors” *Applied Physics Letters*, vol. 93, pp. 033509, 2008

7. S. Fedderwitz, A. Stöhr, **K. H. Tan**, S. F. Yoon, M. Weiß, A. Poloczek, W. K. Loke, S. Wicaksono, T. K. Ng, V. Rymanov, A. S. Patra, E. Tangdiongga, and D. Jäger, “1.3µm GaNAsSb-GaAs UTC-Photodetectors for 10 Gigabit Ethernet Links,” *IEEE Photonic Technology Letters*, vol. 21, pp. 911-913, 2009

8. W.K. Loke, S.F. Yoon, Z. Xu , **K.H. Tan** , T.K. Ng , Y.K. Sim, S. Wicaksono, N. Saadsaoud, D. Decoster, and J. Chazelas, “GaNAsSb/GaAs waveguide photodetector with response up to 1.6µm grown by molecular beam epitaxy,” *Applied Physics Letters*, vol. 93, pp. 081102, 2008

9. W. K. Loke, S. F. Yoon, **K. H. Tan**, S. Wicaksono, and W. J. Fan, "Improvement of GaInNAs p-i-n photodetector responsivity by antimony incorporation," *Journal of Applied Physics*, vol. 101, pp. 33122-1, 2007.

ATTENTION: The Singapore Copyright Act applies to the use of this document. Nanyang Technological University Library

10. W. K. Loke, S. F. Yoon, S. Wicaksono, **K. H. Tan**, and K. L. Lew, "Defect-induced trap-assisted tunneling current in GaInNAs grown on GaAs substrate," *Journal of Applied Physics*, vol. 102, pp. 054501-6, 2007.

11. S. Wicaksono, S. F. Yoon, W. K. Loke, **K. H. Tan**, K. L. Lew, M. Zegaoui, J. P. Vilcot, D. Decoster, and J. Chazelas, "Effect of growth temperature on defect states of GaAsSbN intrinsic layer in GaAs/GaAsSbN/GaAs photodiode for 1.3µm application," *Journal of Applied Physics*, vol. 102, pp. 044505-7, 2007.

12. H. T. Pham, S. F. Yoon, **K. H. Tan**, and D. Boning, "Effects of nitrogen incorporation in $InSb_{1-x}N_x$ grown using radio frequency plasma-assisted molecular beam epitaxy," *Applied Physics Letters*, vol. 90, pp. 92115-1, 2007.

ATTENTION: The Singapore Copyright Act applies to the use of this document. Nanyang Technological University Library

Chapter 1 Introduction

1.1 Background

Devices sensitive to wavelengths between 0.9 to 1.6µm have attracted great interests for optical communication system. A typical optical communication system consists of 3 major components: signal transmitter (e.g. laser), signal transportation medium (e.g. optical fiber) and signal receiver (e.g. photodetector). For a signal to be detectable at the receiver, the signal intensity has to be above a threshold value. Hence, it will be ideal for a signal to travel along the optical fiber without losing its intensity. However, far from ideal, the optical fiber, which is typically made of silica material, is absorptive to the signal (laser light). Signal intensity traveling along the optical fiber will be decreased due to the absorption of laser light by the silica. To ensure the signal is detectable at the receiver side, a repeater/amplifier has to be implemented along the optical fiber to amplify the signal, leading to the increase in cost.

The amount of light absorbed by the silica is dependent on the wavelength of the transmitted light (e.g. laser). As shown in Figure 1.1, it can be seen that the loss of signal intensity is minimal at 1.3µm and 1.55µm. Operating at these wavelengths leads to a longer transmission distance of the light signal in the silica fiber [1].

Furthermore, devices sensitive to wavelengths between 0.9 to 1.6µm are also of

ATTENTION: The Singapore Copyright Act applies to the use of this document. Nanyang Technological University Library

interested because of the light dispersion nature of the silica in that range of wavelengths. Dispersion occurs because the refractive index of silica changes as a function of the wavelength of incident light. The change in the refractive index (n) and group refractive index (n_g) in silica for different wavelengths can be seen in Figure 1.2. Due to the changes in the group refractive index, light of different wavelengths will travel at different speeds in the silica. This leads to broaden of the optical signal pulse width and severely decreases the maximum bit rate transmitted through the fiber [2].

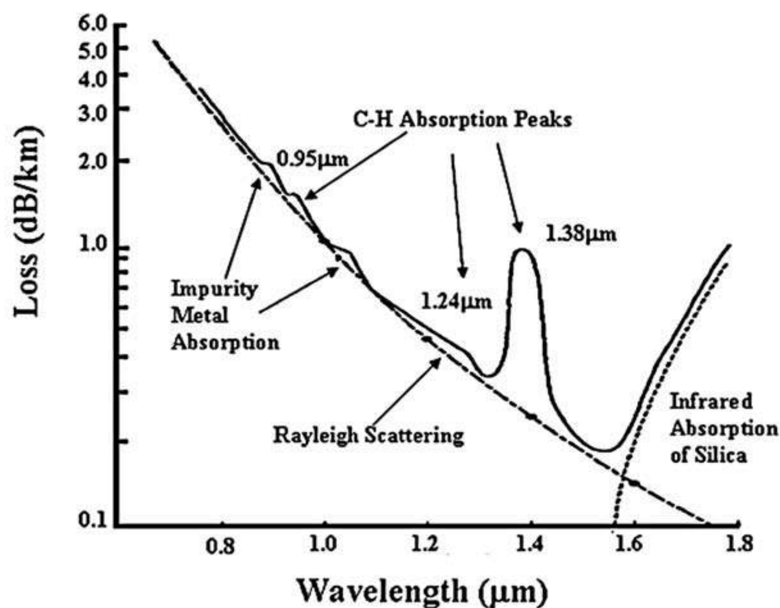

Figure 1.1 Attenuation of light traveling in silica fiber at different wavelengths [1].

Material dispersion (D_M) is related to n_g by:

$$D_M = \frac{1}{c}\frac{dn_g}{d\lambda} \tag{1.1}$$

ATTENTION: The Singapore Copyright Act applies to the use of this document. Nanyang Technological University Library

where c is the speed of light and λ is the operating wavelength. From Figure 1.2, it can be seen that the value of $\frac{dn_g}{d\lambda}$ is smaller at the wavelength range between 0.9 to 1.6μm compared to that at shorter wavelength range. Zero dispersion occurs at wavelength of 1.3μm.

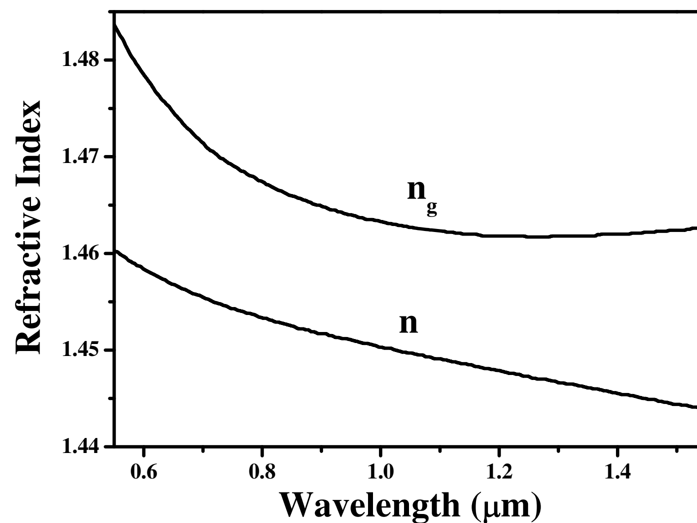

Figure 1.2 The change of refractive index (n) and group refractive index (n_g) in the silica at different wavelengths [2].

Taking into account the effect of absorption and dispersion, the maximum transmission distance and its corresponding maximum bit rate at different wavelengths [3] are shown in Figure 1.3. At bit rate of 10Gb/s, which is needed in the next generation of telecommunication systems, optical fiber systems operating at wavelengths of 1.3μm and 1.55μm increase the maximum transmission distance by 2 to 3 orders, compared to those operating at shorter wavelengths.

ATTENTION: The Singapore Copyright Act applies to the use of this document. Nanyang Technological University Library

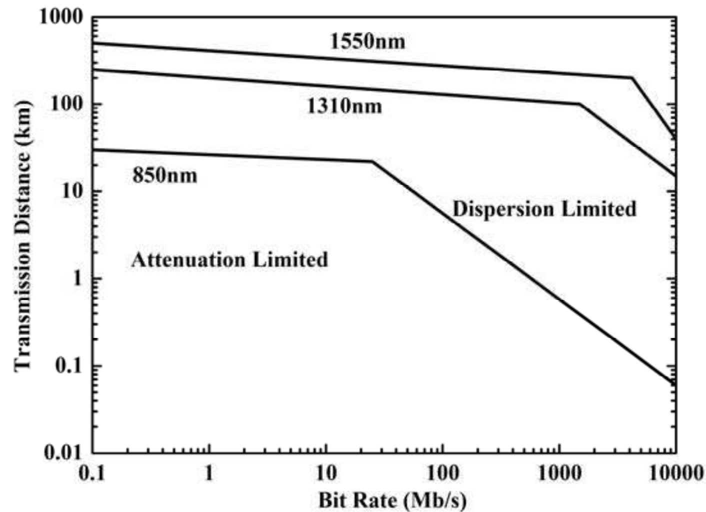

Figure 1.3 Transmission distances of 850nm, 1310nm and 1550nm lasers in optical fiber at different bit rates [3].

Another advantage of using the near infrared wavelength for fiber system is eye safety. Optical fiber system employs a laser as the transmitter. Eye damage can occur under excessive laser exposure. The degree of risk posed by laser radiation to the eye depends on the wavelength of the laser. As the human eye cannot focus the long wavelength laser radiation onto the retina, infrared lasers pose less risk to the eye. Laser operating at wavelength from 0.9 to 1.6µm can be safely used at power level up to 0.3mW because of its low risk to the eye. For short wavelength laser (<0.8µm), the device is only considered eye safe at the power level less than 0.0004mW [4].

Optoelectronic devices require an active layer material with the energy bandgap of 0.9eV and 0.8eV to operate at wavelength of 1.3µm and 1.55µm, respectively. Previously, III-V material with the bandgap less than 1eV could not be realized on

ATTENTION: The Singapore Copyright Act applies to the use of this document. Nanyang Technological University Library

the GaAs substrate platform and is only available on InP substrate platform. This is due to the lack of small bandgap material which is lattice-matched to GaAs. However, with the introduction of GaNAs material in 1992 [5], incorporation of a small amount of nitrogen (N) (0% to 4%) was found to reduce the bandgap of GaAs. Kondow *et al.* [6] has reported the GaInNAs material as the first material, which is lattice-matched to GaAs and has small bandgap of 1eV in 1996.

GaNAsSb was firstly proposed by Ungaro *et al.* [7] in 1999 as a potential GaAs-based material for near infrared applications. In their report, a strained GaNAsSb layer with bandgap of ~0.8eV was grown on GaAs using the molecular beam epitaxy (MBE) system. In the GaInNAs material system, indium (In) atoms are used to counter-balance the tensile strain induced by the incorporation of nitrogen. However, in the GaNAsSb material system, antimony (Sb) atoms are used to counter-balance the tensile strain, instead of the indium atoms. Thus, it is interesting to compare the bandgap shrinkage induced by In and Sb under the same amount of compressive strain. Harmand *et al.* [8] reported that Sb induces larger bandgap reduction compared to In at the same amount of compressive strain. Therefore, under lattice-matched conditions to GaAs and with the same amount of nitrogen, the bandgap of GaNAsSb is smaller compared to that of GaInNAs. In other words, the GaNAsSb system needs fewer nitrogen atoms to achieve bandgap of 0.8eV (corresponding to the wavelength of 1.55μm) compared to GaInNAs. Furthermore, the comparison between GaNAs, GaInNAs and GaNAsSb shows

ATTENTION: The Singapore Copyright Act applies to the use of this document. Nanyang Technological University Library

that the presence of Sb atoms promotes the incorporation of N atoms and decreases the nitrogen-related defects [9].

1.2 Motivation and objective

1.2.1 GaNAsSb-based p-i-n photodetector

Photodetectors operating at wavelength of 0.9 to 1.6µm have been extensively studied [10, 11]. In this thesis, 1.3µm and 1.55µm photodetectors have been investigated. The 1.3µm photodetectors reported in this thesis are entirely surface illuminated. However, the 1.55µm photodetectors reported in this thesis are edge illuminated. The reason for designing the 1.55µm GaNAsSb-based photodetector as an edge illuminated device is discussed in chapter four.

The role of 1.3µm photodetectors is strategically important due to the expansion of fiber optic systems into mid haul (<10km) data communication networks. Most of the mid haul fiber optic systems operate at wavelength of 1.3µm. Conventionally, fiber optic systems are implemented in long haul data communication systems, such as intercontinental networks and intercity networks. Due to the increasing demand on bandwidth and the bandwidth limitation in copper wires, the usage of the fiber optic has been expanded to metro networks. One example is fiber to the home (FTH) concept, which targets to use optical fiber to replace all or part of the usual copper wire local loop used for last mile data communication. For the mid

ATTENTION: The Singapore Copyright Act applies to the use of this document. Nanyang Technological University Library

haul network, 10GBASE-LR fiber optic system has been specified by IEEE802.3 protocol and operating at wavelength of 1310nm. It delivers data over single-mode fiber at a data rate of 10.3125Gb/s for up to distance of 10km.

To date, most of the 0.9 to 1.6μm photodetectors are fabricated on InP substrate. InP-based near infrared photodetectors have achieved cutoff frequency higher than 10GHz, which is sufficient for use in future optical communication systems. However, the main challenge of InP-based near infrared photodetector is the cost. Current commercially available InP-based photodetectors are expensive because of the high substrate cost and expensive process technology. A more economical solution for near infrared photodetectors is to fabricate the photodetector structure on GaAs substrates, which are not only cheaper than InP substrate, but available in larger wafer size. The largest commercially available InP substrate is four inches in diameter, while the largest GaAs substrate is eight inches in diameter. Larger substrate allows more devices to be processed in a single process run, leading to lower fabrication cost.

Besides the issue of cost, the low refractive index contrast of the InP-based materials poses difficulties for designing mirror systems, which are important in optoelectronic devices such as resonant cavity enhanced (RCE) photodetector. The mirror system traps the incoming light within the cavity and increases the light absorption efficiency of the photodetector. The most common mirror systems in

ATTENTION: The Singapore Copyright Act applies to the use of this document. Nanyang Technological University Library

InP-based material are GaInAsP/InP, AlGaInAs/AlInAs and AlGaAsSb system. The refractive index contrast of GaInAsP/InP and AlGaInAs/AlInAs systems are very small and more than 50 mirror pairs are needed to contain sufficient light in the cavity [12]. For the AlGaAsSb system, even though it has higher refractive index contrast, its high resistivity and poor thermal conductivity lead to heat generation and dissipation problems in the active region [12]. On the other hand, a GaAs-based mirror system does not have these problems. The AlAs/GaAs mirror system has a high refractive index contrast. Confinement of the incident light within the cavity only requires 20-30 pairs of AlAs/GaAs mirrors. Furthermore, the AlAs/GaAs system has a high thermal conductivity compared to quaternary alloys, such as AlGaAsSb.

Although the GaAs-based material system has advantages as mentioned above, the materials which are lattice-matched to GaAs and have absorption wavelengths of between 0.9 to 1.6μm are previously not available. Historically, alloys which are lattice-matched to GaAs have an absorption wavelength of less than 1μm. This drawback can be overcome by introducing nitrogen atom into the GaAs-based material. Introduction of N atoms into the GaAs lattice can extend the absorption wavelength of the material to the range of 0.9 to 1.6μm. There are two types of N containing GaAs-based material systems, which are lattice-matched to GaAs substrate and have absorption wavelengths lying between 0.9 to 1.6μm, namely GaInNAs [6] and GaNAsSb [7]. GaNAsSb is chosen over GaInNAsSb because it

ATTENTION: The Singapore Copyright Act applies to the use of this document. Nanyang Technological University Library

has a smaller conduction band offset with GaAs. Smaller conduction band offset will reduce the electron trapping at the GaNAsSb/GaAs junction and improve the high frequency performance. Furthermore, in the absence of In atoms, lower level of nitrogen-related defects can be expected in GaNAsSb compared to GaInNAsSb.

Reported results [13, 14] of dilute nitride-based photodetector have shown cutoff frequency below 1GHz. This cutoff frequency value is insufficient for high speed fiber optic communication system where higher GHz levels are needed. Furthermore, most reported results were based on quantum well i–layer structure [14-16]. The quantum well structure is inferior in absorption efficiency and high speed performance compared to the p-i-n structure. A minimum light absorption layer thickness of 100nm is required to have efficient light absorption. The quantum well structure has very thin (<10nm) light absorption layer, leading to low absorption efficiency. The barrier layer of the quantum well structure also leads to carrier trapping. Instead of sweeping away by the electric field to the electrodes, the carriers generated by the light absorption are trapped inside the quantum well. This leads to the deterioration in high frequency performance.

Compared to 1.3μm photodetectors, which have been implemented in mid haul (<10km) fiber communication systems, the 1.55μm photodetectors play a more important role in long haul fiber optic communication systems. In 10Gigabit Ethernet systems, components operating at wavelength of 1.55μm have been

ATTENTION: The Singapore Copyright Act applies to the use of this document. Nanyang Technological University Library

utilized in 10GBASE-ER (up to 40km) and 10GBASE-ZR (up to 80km) systems. In this context, it is potentially possible to make GaNAsSb-based devices suitable for 1.55μm wavelength detection if the nitrogen and antimony contents are increased to reduce the energy bandgap while keeping the crystal lattice-matched to GaAs. However, it was also found that by increasing the nitrogen and antimony contents, more nitrogen-related defects will be incorporated, which degrades the crystal quality and device performance. An alternative approach is to use lattice mismatch systems by increasing the Sb content only. However, the quantum efficiency of the photodetectors will be constrained by the critical layer thickness of the strained photon-absorption GaNAsSb layer. This constraint can be overcome by coupling the incident light directly into the edge of the device based on the concept of a waveguide photodetector (WGPD), where light absorption is independent of the thickness of the photon-absorption layer and dependent on the length of the device.

Thus, in this thesis, near infrared 1.3μm p-i-n photodetectors incorporated with an active GaNAsSb layer were investigated. In addition to p-i-n conventional photodetectors, a GaNAsSb-based uni-traveling carrier (UTC) photodetector was also grown and fabricated to improve the high frequency performance. It is desirable to demonstrate bandwidth of 10GHz and high responsivity capability in GaNAsSb-based photodetector to fulfill the requirements of 10GBASE-LR fiber optic communication systems. The performance of the photodetectors was

ATTENTION: The Singapore Copyright Act applies to the use of this document. Nanyang Technological University Library

characterized by their temporal response, spectral response, photoresponsivity and 3dB cutoff frequency. Fiber optic data transmission using the GaNAsSb-based photodetectors was also demonstrated. Furthermore, to extend the photo-response to the wavelength of 1.55μm, a waveguide photodetector with an active strained GaNAsSb layer was demonstrated.

1.2.2 GaNAsSb-based photoconductive switch

Photoconductive switches are potential devices for THz optoelectronic applications due to its picosecond response to optical excitation. The photoconductive switch was first reported by Auston *et al*. [17] in 1975. Smith *et al.* [18] demonstrated picosecond response in photoconductive switches based on low temperature grown gallium arsenide (LT-GaAs) as the active material in 1988. The LT-GaAs material is an ideal material for photoconductive switch applications due to its subpicosecond carrier lifetime and electrically semi-insulating property. Besides LT-GaAs, ion implanted GaAs has also been demonstrated in photoconductive switch application and has similar properties compared to LT-GaAs [19, 20].

However, GaAs-based photoconductive switches have one major drawback, which is GaAs has optical bandgap of 1.43eV. This prohibits the GaAs-based photoconductive switches to operate at common optical communication wavelengths of 1.3μm and 1.55μm. Efforts such as utilization of the trap assisted

ATTENTION: The Singapore Copyright Act applies to the use of this document. Nanyang Technological University Library

two-step absorption to produce photo-response at 1.55μm in LT-GaAs photoconductive switches [21] has been reported. However, the resulting photoresponsivity produced by such two-step absorption process is rather weak. To extend the photo-response to 1.3μm and 1.55μm, small bandgap material such as LT-InGaAs has been demonstrated as the active material of the photoconductive switch. However, unlike LT-GaAs, the concentration of arsenic antisite-related deep states in LT-InGaAs grown at 200°C is low (~0.4% compared to ~2% in LT-GaAs) [22, 23], leading to relatively long carrier lifetimes [24]. To reduce the carrier lifetime, irradiation of the InGaAs material using various types of energetic ions has been reported [25].

GaNAsSb can be tailored to lattice match to GaAs and has bandgap from 1.43eV to 0.8eV, depending on the concentration of nitrogen and antimony atoms. At 3.5% of nitrogen and 9% of antimony, GaNAsSb is lattice-matched to GaAs and has bandgap of 0.88eV. Apart from its small bandgap, GaNAsSb is attractive for photoconductive switch application because of its short carrier lifetimes. The growth of dilute nitride materials, such as GaNAsSb and GaInNAs at low temperature (<500°C) and the disparity between the size of nitrogen atoms and the size of replaced group-V atoms lead to the formation of mid-gap arsenic antisite and nitrogen-related defects [26-30]. These defects contribute to such materials having short carrier lifetimes [31, 32] and low photoluminescence efficiency [33]. In this thesis, the application of GaNAsSb as active material for photoconductive

ATTENTION: The Singapore Copyright Act applies to the use of this document. Nanyang Technological University Library

switching was demonstrated. The pulsed response measurement of the GaNAsSb-based photoconductive switch has shown photo-response at wavelengths up to 1.6μm. Furthermore, the ON/OFF ratio was used to evaluate the performance of the GaNAsSb-based photoconductive switch in microwave switching application.

1.2.3 GaNAsSb optical waveguide

The use of optical waveguides based on III-V compound semiconductors is motivated by the applications of monolithically integrated optoelectronic components. For optical waveguide systems on GaAs substrate, there have been numerous studies [34-41] on the AlGaAs/GaAs material system, where GaAs and AlGaAs are used as the guiding layer and cladding layer, respectively.

For an ideal optical waveguiding material on GaAs substrate, three requirements must be fulfilled. Firstly, the guiding layer must be lattice-matched to GaAs to enable the growth of a sufficiently thick layer. Secondly, there should be a sufficiently large optical bandgap difference between the guiding and cladding layer (*i.e.* high refractive index contrast) and thirdly, the guiding layer should have low absorption of the transmitted light at the desired wavelength. The dilute nitride-antimonide material, GaNAsSb fulfills these requirements. The GaNAsSb material has been reported [42-44] for application in photodetector at 1.3μm. At

ATTENTION: The Singapore Copyright Act applies to the use of this document. Nanyang Technological University Library

~3.5% of N and 9% of Sb, GaNAsSb is lattice-matched to GaAs substrate and has optical bandgap of ~0.9eV. Under the lattice-matched condition, the growth of a thick layer of GaNAsSb >0.5μm can be achieved on GaAs. Its bandgap of 0.9eV will ensure minimal absorption at transmission wavelength of 1.55μm. Furthermore, the 0.5eV bandgap difference between GaNAsSb and GaAs should give a high refractive index contrast between the two materials, leading to good optical confinement.

Compared to the AlGaAs/GaAs/AlGaAs optical waveguide system, the GaAs/GaNAsSb/GaAs system has two distinguishing features. Firstly, unlike the AlGaAs/GaAs/AlGaAs system, which is capable of transmitting light of wavelength >1μm, the GaAs/GaNAsSb/GaAs system only transmits light of wavelength >1.4μm. This is useful for applications where the selectivity between light with wavelengths of 1.3μm and 1.5μm is important. Secondly, the GaAs/GaNAsSb/GaAs system uses GaAs substrate as the bottom cladding layer. In the AlGaAs/GaAs/AlGaAs waveguide system, a thick (>4μm) bottom AlGaAs cladding layer is needed to reduce the propagation loss [37, 40]. However, in the GaAs/GaNAsSb/GaAs waveguide system, the GaAs substrate acts as the bottom cladding layer, thus eliminating the need for another material to make up the thick bottom cladding layer. Furthermore, as the substrate thickness is >300μm, better light confinement can be achieved.

ATTENTION: The Singapore Copyright Act applies to the use of this document. Nanyang Technological University Library

In this thesis, a GaAs/GaNAsSb/GaAs waveguide system was grown using a MBE system. The performance of the waveguide was characterized by its propagation loss. The propagation loss of the waveguides was measured using Fabry Perot method. Furthermore, the performance of the waveguide system was analyzed and correlated to the material properties of the GaNAsSb system.

1.3 Major contributions of the thesis

In this thesis, the GaNAsSb materials were grown using the solid-source MBE system in conjunction with an antimony valved cracker source and a radio frequency (RF) plasma nitrogen source. An ion deflection plate has been installed into the nitrogen plasma source to improve the quality of the dilute nitride material. Reduction of defects in the dilute nitride material was demonstrated after such modification of the plasma source,

P-i-n GaNAsSb-based photodetectors have been grown using the molecular beam epitaxy system in conjunction with the modified N plasma source and Sb valved cracker source. The spectral response shows photo-response up to 1380nm. DC responsivity of up to 12A/W has been demonstrated. This indicates the occurrence of a carrier avalanche process in the devices [45]. The high responsivity shown in this work is the highest value of responsivity ever reported for dilute nitride-based photodetectors. High speed performance of the p-i-n GaNAsSb-based

ATTENTION: The Singapore Copyright Act applies to the use of this document. Nanyang Technological University Library

photodetectors was characterized using temporal response and frequency response measurements. From the measurements, the device shows 3dB cutoff frequency of 4.5GHz, a record 3dB cutoff frequency for dilute nitride-based photodetectors at the time it was reported [43]. It was found that slow carrier diffusion in the undepleted region of the i-GaNAsSb layer limits the high speed performance. Fiber optic data communication and clear opened eye diagram has been successfully demonstrated at data rate of 5Gb/s with the GaNAsSb-based p-i-n photodetector [46].

The GaNAsSb-based UTC photodetector structure was grown and fabricated to further improve the high frequency performance of the GaNAsSb-based photodetector. The GaNAsSb-based UTC photodetector shows 3dB cutoff frequency of 14GHz [47]. Low electron mobility in the GaNAsSb material limits the bandwidth of the GaNAsSb-based UTC photodetector material. The eye diagram was clearly opened at data rate of 12.5Gb/s. Moreover, data transmission over a 10km fiber was successfully demonstrated using this UTC photodetector at data rate of up to 12.5Gb/s. The performance of the GaNAsSb-based UTC photodetector fulfills the requirements of 10GBASE-LR fiber optic systems in 10GB Ethernet applications.

A 1.55µm GaNAsSb-based p-i-n waveguide photodetector was grown using molecular beam epitaxy. The device consists of a 0.4µm-thick active strained

ATTENTION: The Singapore Copyright Act applies to the use of this document. Nanyang Technological University Library

GaNAsSb layer. This GaNAsSb layer contains 3.5% of N and 18% of Sb. The X-ray reciprocal space map of the GaNAsSb layer shows strain relaxation of 1% in the GaNAsSb material. The photodetector exhibits photo-response of up to at least 1.6µm in the spectral response. Photoresponsivity of up to 0.29A/W at wavelength of 1550nm was demonstrated [48].

The high electrical resistance and short carrier lifetimes in the GaNAsSb material make it an ideal candidate for the active material in a photoconductive switch. The application of GaNAsSb material in photoconductive switching was demonstrated in this thesis. The switch structure was grown using MBE and has a 0.5µm-thick GaNAsSb photon-absorption layer on top of a semi-insulating GaAs substrate. The switch exhibits pulsed response with FWHM of 30ps and photo-response of up to 1.6µm [49]. The GaNAsSb-based photoconductive switch shows an ON/OFF ratio of 11dB at 1GHz and exhibits a response up to 15GHz [49] in the microwave switching operation at wavelength of 790nm. The GaNAsSb-based photoconductive switch shows a negligible ON/OFF ratio at wavelengths of 1.3µm and 1.55µm. This is due to the inefficient photon-absorption process in the GaNAsSb layer at these wavelengths.

The bandgap of the GaNAsSb was reduced to ~0.8eV to increase the efficiency of the photon-absorption at wavelength of 1.55µm. The GaNAsSb-based photoconductive switch with a GaNAsSb layer, which has the bandgap energy of

ATTENTION: The Singapore Copyright Act applies to the use of this document. Nanyang Technological University Library

0.8eV, shows an ON/OFF ratio of 9dB at the wavelength of 1.55µm. This is the first demonstration of a photoconductive switch in the 1.55µm microwave switching application.

Apart from photon-detection, the GaNAsSb material has also been applied to optical waveguide application. A 1.55µm GaAs/GaNAsSb/GaAs optical waveguide was fabricated as an alternative device to the AlGaAs/GaAs optical waveguide [50]. The waveguide consists of a 0.4µm-thick GaNAsSb guiding layer, which contains ~3.5% of N and 9% of Sb, resulting in optical bandgap of 0.88eV. The GaNAsSb layer has a refractive index value of 3.42 at the wavelength of 1.55µm. The refractive index value of GaAs at 1.55µm is 3.37. The confinement and guiding of the 1.55µm light using this GaAs/GaNAsSb/GaAs optical waveguide was successfully demonstrated. The propagation loss measured using the Fabry-Perot resonance method was found to be affected by nitrogen-related defect absorption.

1.4 Organization of thesis

Chapter one is the introduction of this thesis, in which the background of the fiber optic communication systems and the GaNAsSb material are presented. This is followed by the motivation for the work reported in this thesis. This chapter also presents the research objective, major contributions and organization of this thesis.

ATTENTION: The Singapore Copyright Act applies to the use of this document. Nanyang Technological University Library

Chapter two presents the theoretical calculation of the GaNAsSb bandgap. Furthermore, chapter two also covers the background of the p-i-n photodetector, uni-traveling carrier photodetector, photoconductive switch and optical waveguide. Chapter three covers the MBE growth of the GaNAsSb material. The determination of N and Sb content in the GaNAsSb using the x-ray diffraction technique is explained. This chapter also presents the significant improvement in the dilute nitride material quality by modifying the nitrogen plasma source. A pair of ion deflection plates has been installed into the nitrogen plasma source.

Chapter four presents the results of the GaNAsSb-based p-i-n photodetector. The DC and high frequency performance of p-i-n photodetector are presented. Extension of photo-response to 1.6µm using the GaNAsSb-based waveguide p-i-n photodetector is also reported. Chapter five presents the results of the GaNAsSb-based uni-traveling carrier photodetector. The temporal response, 3dB cutoff frequency and eye diagram results of the photodetector are shown and discussed. This chapter also covers the data transmission results of the GaNAsSb-based UTC photodetector.

Chapter six presents the results of the GaNAsSb-based photoconductive switch. The pulsed response of the switch and its performance in the microwave switching application is discussed. Chapter seven presents the results of the GaNAsSb-based

ATTENTION: The Singapore Copyright Act applies to the use of this document. Nanyang Technological University Library

optical waveguide system. This chapter covers the light confinement and propagation loss of the GaNAsSb/GaAs waveguide. Chapter eight summarizes the results of the research in this thesis and recommends some directions for future research work.

ATTENTION: The Singapore Copyright Act applies to the use of this document. Nanyang Technological University Library

Chapter 2 Bandgap of GaNAsSb and device principles

2.1 Bandgap of GaNAsSb

As previously mentioned, the incorporation of N and Sb into GaAs decreases its bandgap. The bandgap reduction attributed to the incorporation of Sb atoms into GaAs mostly affects the valence band. On the other hand, the bandgap reduction due to N atoms affects the conduction band. The bandgap energy of III-V ternary and quaternary materials can be extrapolated using the bandgap energy of the constituent binary materials and a parameter known as the bowing coefficient. For $GaAs_{1-x}Sb_x$, the bandgap, E_g can be described as [51]:

$$E_g = 1.43 - 2.24x + 1.97x^2 eV \quad (2.1)$$

For GaNAs, the bandgap extrapolation can be written as follows [52]:

$$E_g(GaN_xAs_{1-x}) = xE_g(GaN) + (1-x)E_g(GaAs) - x(1-x)C \quad (2.2)$$

where x is the nitrogen atomic concentration, $E_g(GaN)$ and $E_g(GaAs)$ are the binaries bandgap energy and C is the bowing factor. However, the prediction using this method was found to be relatively inaccurate for N concentration > 2%. Subsequently, the band anti-crossing (BAC) model [53] was proposed to predict and explain the reduction of the bandgap in dilute nitride materials with greater accuracy.

ATTENTION: The Singapore Copyright Act applies to the use of this document. Nanyang Technological University Library

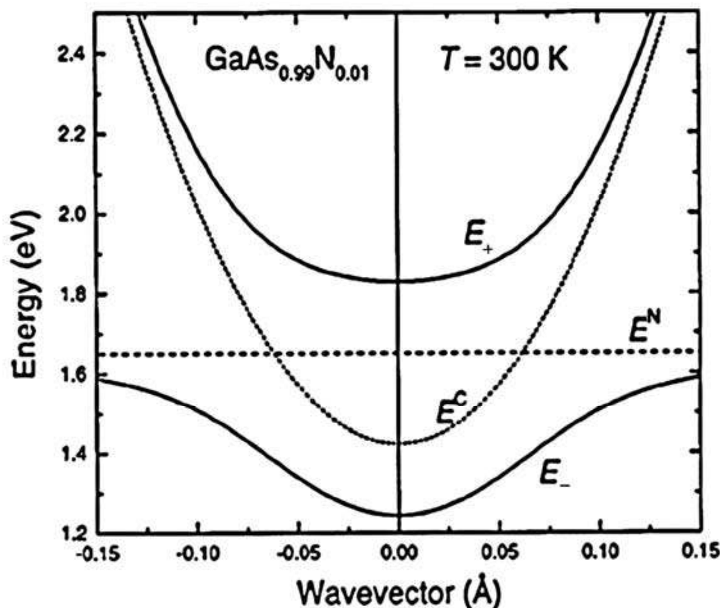

Figure 2.1 Band diagram illustration of formation of two energy levels E_- and E_+, by interaction between the nitrogen state (E^N) and the GaAs conduction band (E^C) [54].

In the BAC model, introduction of small atomic concentration of N to GaAs induces a highly localized nitrogen iso-electronic impurity energy level (E^N). The E^N energy state is located above the GaAs conduction band minima, due to the large electro-negativity of N atoms (3.0eV). As shown in Figure 2.1, E^N appears to intersect with the conduction band of GaAs. As the Pauli's exclusion principle prohibits two states to have the same energy level, the two states "anti-cross" and form two new energy levels (E_+ and E_-) with E_- as the new conduction band minimum. With the increase in atomic N concentration, the repulsion between the E_+ and E_- levels increases, leading to a further reduction in the new bandgap energy, which is the difference between the E_- states and the valence band maximum.

ATTENTION: The Singapore Copyright Act applies to the use of this document. Nanyang Technological University Library

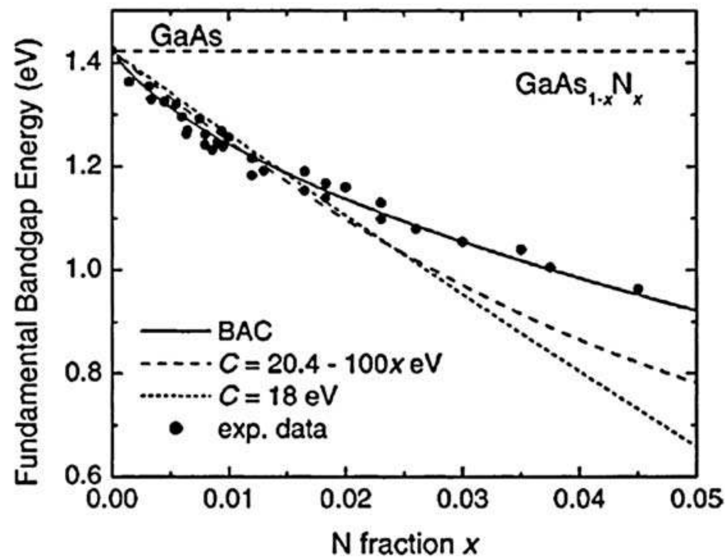

Figure 2.2 Calculated bandgap energy of GaNAs as function of nitrogen fraction, *x*, (a) from the BAC model (solid curve), (b) using the variable bowing parameter (dashed curve), (c) using a constant bowing parameter (dotted curve) and (d) experimental data (solid circle) [54].

Figure 2.2 shows the experimental bandgap energy for GaNAs compared to the calculated value of the bandgap using Eq. (2.2) (using constant and N concentration-dependent bowing coefficients) and the BAC model. Figure 2.2 clearly shows that the bandgap calculated using the BAC model fits the experimental value over a wider range of N concentration as compared to the calculation results of Eq. (2.2).

Incorporation of Sb or N contributes to the reduction in the bandgap. Thus, modification of the BAC model is required to estimate the bandgap of GaNAsSb.

ATTENTION: The Singapore Copyright Act applies to the use of this document. Nanyang Technological University Library

Modification of the BAC model ensures that the effects of Sb and N are taken into account in the bandgap calculation. The combined effect of Sb and N on the bandgap has been reported by Dang *et al.* [55]. The level of E_- states with reference to valence band maximum (e.g. bandgap) for $GaN_xAs_{1-y-x}Sb_y$ can be described as:

$$E_- = \frac{1}{2}\left(\left[E^C + E^N\right] - \sqrt{\left(E^C - E^N\right)^2 + 4V^2x}\right) \quad (2.3)$$

where

$$E^N = 1.65(1-y) + 1.44y - 0.38y(1-y) \quad (2.4)$$

$$E^C = (1-y)E_g(GaAs) + yE_g(GaSb) - 1.43y(1-y) \quad (2.5)$$

$$V = 2.7\text{eV} \quad (2.6)$$

Using equations above, the calculated bandgap of the GaNAsSb which is lattice-matched to GaAs for different nitrogen composition can be seen in Figure 2.3.

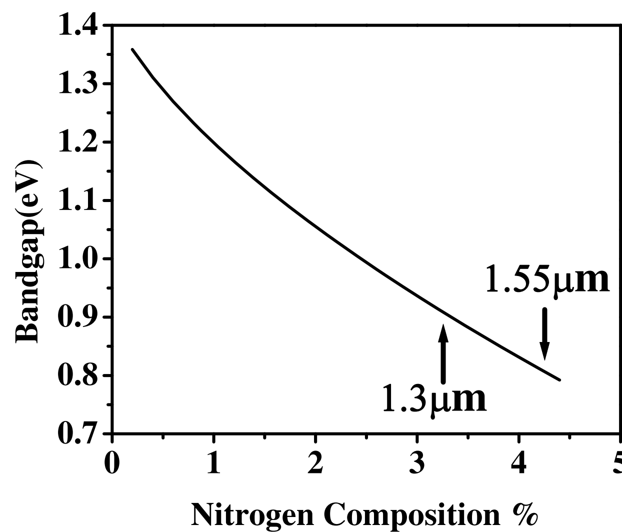

Figure 2.3 Bandgap energy of GaNAsSb material system which is lattice-matched to GaAs *vs.* nitrogen composition.

ATTENTION: The Singapore Copyright Act applies to the use of this document. Nanyang Technological University Library

2.2 Device principles

2.2.1 p-i-n photodetector

A typical photodetector consists of three layers: highly p-doped layer, undoped photon-absorption i-layer and highly n-doped layer as shown in Figure 2.4. The p and n layers are typically made of wider bandgap materials, which are transparent to the incident light.

The n layer is firstly grown on the substrate. It is followed by the growth of i-layer and p layer. There are two advantages for designing the p layer on top of the device, *i.e.* (1) minimizing transit time of hole carrier and (2) minimizing the effect of the gap between the mesa and the n contact.

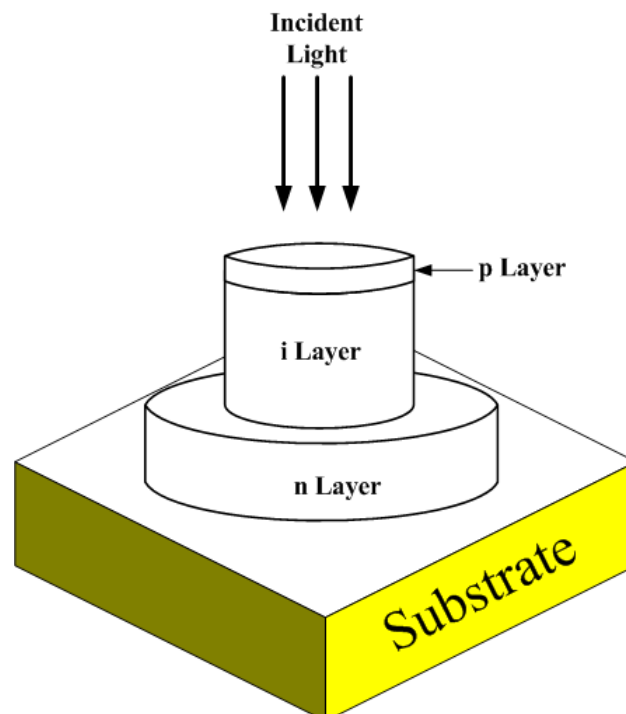

Figure 2.4 Schematic diagram of a p-i-n photodetector.

ATTENTION: The Singapore Copyright Act applies to the use of this document. Nanyang Technological University Library

In a top surface illuminated photodetector, the absorption of light and thus, the creation of electron-hole pairs mostly occurs near the top section of the i-layer. Since hole mobility is much lower than electron mobility, minimum hole transit distance is preferred in order to have minimum hole transit time for the hole carriers. By putting the p layer on top of the p-i-n structure, most of the hole carriers will be created near the p layer and thus, will have shorter transit distance as they drift towards the p layer. Moreover, there is a lateral gap between the mesa structure and n contact metal in most of the p-i-n photodetectors. The gap, usually >1μm, leads to the increase in the carrier transit time. To minimize this effect, the carrier, which has higher velocity, *i.e.* electrons, is preferred to traverse across this gap. Therefore, it is favorable for the top-illuminated p-i-n photodetectors to adopt p layer on top design.

The band diagram of a top-illuminated p-i-n photodetector under a reverse bias condition is shown in Figure 2.5. The incident light in the depleted i-layer region generates electron and hole pairs which are quickly swept away by the electric field. The electric field empties the states in the valence and conduction bands and ensures that the subsequent efficiency in photon-absorption is unaffected. Furthermore, a higher electric field across the junction as a result of the reverse bias voltage provides a higher drift velocity for electrons and holes, leading to shorter response time of the devices.

ATTENTION: The Singapore Copyright Act applies to the use of this document. Nanyang Technological University Library

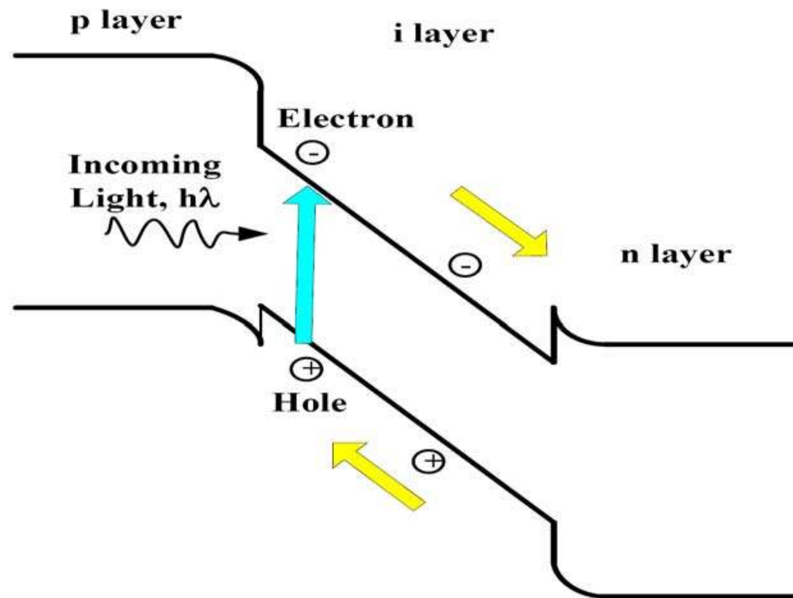

Figure 2.5 Band diagram of a p-i-n photodetector under reverse biased condition.

As light travels across the i-layer, the light intensity decreases as a result of the photon-absorption. The change in light intensity depends on the absorption coefficient of the i-layer material, which can be described as:

$$P(x) = p_o \exp(-\alpha(\lambda)x) \quad (2.7)$$

where $P(x)$ is the attenuated light power in the semiconductor material. x is the length of semiconductor material that the light transverses. p_o is the initial power of the incident light. $\alpha(\lambda)$ is the material dependent absorption coefficient. Figure 2.6 [56] shows the absorption coefficient for a few common semiconductor materials.

ATTENTION: The Singapore Copyright Act applies to the use of this document. Nanyang Technological University Library

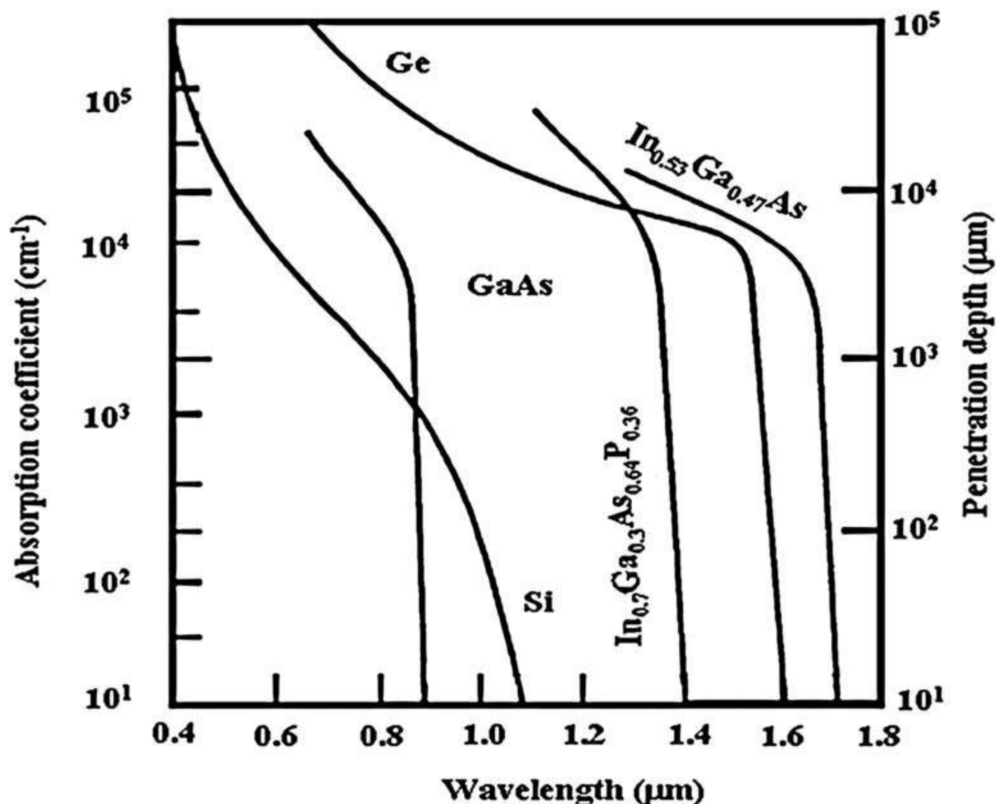

Figure 2.6 Absorption coefficients of several semiconductors at different wavelengths. Adopted from [56].

Taking into account the reflection of the incoming light on the p layer surface, Eq. (2.7) becomes:

$$P(x) = p_o \exp(-\alpha(\lambda)x)(1 - R_f) \tag{2.8}$$

$$R_f = \left(\frac{n_p - n_{air}}{n_{air} + n_p} \right)^2 \tag{2.9}$$

where R_f is the surface reflectance. n_p and n_{air} are the refractive indices of the p layer and air, respectively. For the GaAs/air interface, R_f has a value of 0.28.

ATTENTION: The Singapore Copyright Act applies to the use of this document. Nanyang Technological University Library

The photocurrent of the p-i-n photodetector, I_p can be described as:

$$I_p = \frac{q}{h\nu} P_0 (1 - e^{-\alpha(\lambda)x})(1 - R_f) \qquad (2.10)$$

where q is the electron charge and $h\nu$ is the energy of a single incoming photon.

The quantum efficiency of a photodetector, η can be defined as:

$$\eta = \frac{\text{Number of photogenerated electron - hole pairs}}{\text{Number of incident photons}} = \frac{I_P / q}{P_0 / h\nu} \qquad (2.11)$$

Furthermore, the efficiency and sensitivity of photodetectors can also be characterized by using the photoresponsivity, $\Re$ of the photodetector:

$$\Re = \frac{I_P}{P_0} = \frac{\eta q}{h\nu} \ \text{[A/W]} \qquad (2.12)$$

Figure 2.7 shows the maximum photoresponsivity of conventional photodetectors with different photon-absorption materials at different wavelengths. InGaAs-based photodetector has photoresponsivities of ~0.9A/W and 1A/W at wavelengths of 1.3µm and 1.55µm, respectively.

3dB cutoff frequency is an important parameter to evaluate the high frequency performance of the p-i-n photodetectors. There are two factors, which limit the 3dB cutoff frequency of the photodetector; (1) resistance-capacitance (RC) delay and (2) carrier transit time delay.

ATTENTION: The Singapore Copyright Act applies to the use of this document. Nanyang Technological University Library

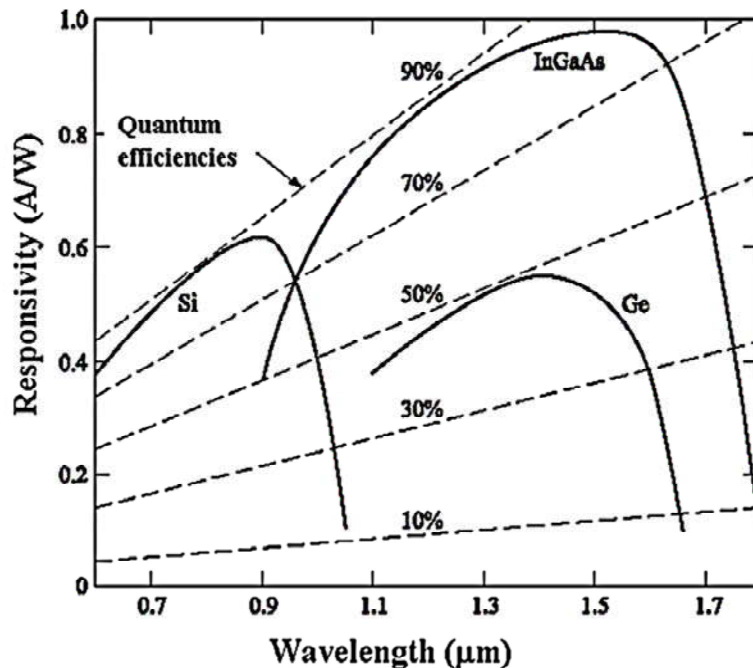

Figure 2.7 Photoresponsivity of different photodetectors materials.

When RC delay dominates, the RC delay limited cutoff frequency, f_{RC} can be expressed as:

$$f_{RC} = \frac{1}{2\pi RC} \tag{2.13}$$

$$C = \frac{\varepsilon_r \varepsilon_o A}{w} \tag{2.14}$$

where R is the shunt resistance and C is the junction capacitance of the photodetector. A is the surface cross section area of the i-layer, w is the width of the depletion region, ε_o is the permittivity of vacuum and ε_r is the dielectric constant of the i-layer.

Combining Eq. (2.13) and (2.14), f_{RC} can be expressed as:

$$f_{RC} = \frac{w}{2\pi R \varepsilon_o \varepsilon_r A} \tag{2.15}$$

ATTENTION: The Singapore Copyright Act applies to the use of this document. Nanyang Technological University Library

On the other hand, the transit time of the carriers (especially holes) across the i-layer limits the high frequency response of the photodetectors when the transit time delay dominates. In this case, the saturated drift velocity of the slower carrier, *i.e.* hole saturated drift velocity, v_{hs} becomes the key parameter to determine the high frequency response of the photodetectors. Thus, the transit time limited cutoff frequency, f_{tr}, can be expressed as:

$$f_{tr} = \frac{0.45 v_{hs}}{w} \tag{2.16}$$

In the condition where neither the RC delay nor the carrier transit time delay dominates, the 3dB cutoff frequency, f_{total} of a p-i-n photodetector can be expressed as:

$$f_{total} = \frac{1}{\sqrt{\left(\frac{1}{f_{RC}}\right)^2 + \left(\frac{1}{f_{tr}}\right)^2}} \tag{2.17}$$

2.2.2 Uni-traveling carrier photodetector

As mentioned in the previous section, there are two major factors, which limit the 3dB cutoff frequency of photodetectors; (1) carrier transit time delay and (2) RC delay. In ultrafast p-i-n photodetectors, the RC delay can be made negligible by having a small junction area. Thus, the 3dB cutoff frequency of these photodetectors is limited by the carrier transit time delay. As the drift velocity of electrons is faster than that of holes, the carrier transit time of ultrafast

ATTENTION: The Singapore Copyright Act applies to the use of this document. Nanyang Technological University Library

photodetectors is approximately equal to the transit time of holes. Ishibashi *et al.* [57, 58] proposed the concept of the uni-traveling carrier photodetector in 1997 to improve the high speed performance of the photodetector by eliminating the slow carriers (holes) in the operation of the photodetectors.

Figure 2.8 shows the band diagram of a UTC photodetector. In principle, a UTC photodetector consists of a p-type narrow bandgap photon-absorption layer, a lightly n-type doped wide bandgap collector layer and a p-type doped wide bandgap diffusion blocker layer. Since the photon-absorption layer is p-type doped and quasi-neutral, the majority carriers in this layer, *i.e.* holes, have a very short response time, *i.e.* within their dielectric relaxation time. On the other hand, photogenerated electrons which diffuse towards the diffusion blocker layer (left side in Figure 2.8) are reflected back due to the conduction band offset at the interface. Those electrons which diffuse towards the collector layer are swept away into the collector layer by the electric field. Consequently, the carrier transit of the UTC photodetector will not involve any holes and only involve electrons, leading to a higher 3dB cutoff frequency.

Unlike conventional p-i-n photodetectors, the depletion region width and the thickness of the photon-absorption layer in UTC photodetectors can be chosen independently. Thus, a very thin absorption layer (<100nm) can be used to attain high 3dB cutoff frequency without affecting the RC delay time constant.

ATTENTION: The Singapore Copyright Act applies to the use of this document. Nanyang Technological University Library

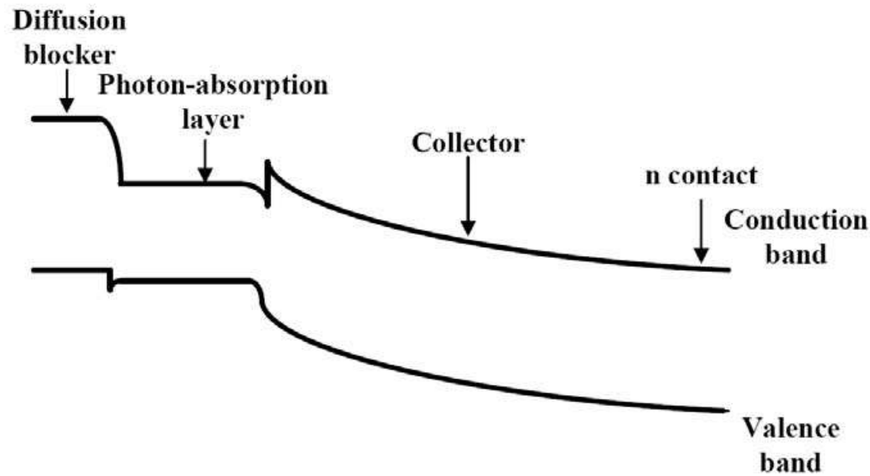

Figure 2.8 Schematic band diagram of uni-traveling carrier photodetector.

The 3dB cutoff frequency of a UTC photodetector is mostly electron transit time limited. There are two components in the electron transit time of the UTC photodetector that governs its 3dB cutoff frequency, namely electron diffusion in the photon-absorption layer and electron drift in the collector layer. The electron drift velocity is higher than its diffusion velocity. Thus, the diffusion velocity of the electrons and the thickness of the photon-absorption layer dominate the electron transit time in the UTC photodetectors. The diffusion velocity of the electrons is proportional to the electron mobility in the photon-absorption layer, according to Einstein's diffusion-mobility relation. In other words, the electron mobility and the thickness of the photon-absorption layer are the two key parameters that determine the 3dB cutoff frequency of the UTC photodetector.

2.2.3 Photoconductive switch

The photoconductive switch was first demonstrated by Auston *et al.* in 1975 [17].

ATTENTION: The Singapore Copyright Act applies to the use of this document. Nanyang Technological University Library

It is basically an optically controlled semiconductor switch to connect two isolated conductors. Figure 2.9 shows the simplest form of a photoconductive switch where a highly resistive semiconductor layer is sandwiched by two conductors, which are biased with an electrical voltage. The incident light into the semiconductor surface reduces the electrical resistance of the semiconductor and increases the magnitude of current flowing through the semiconductor.

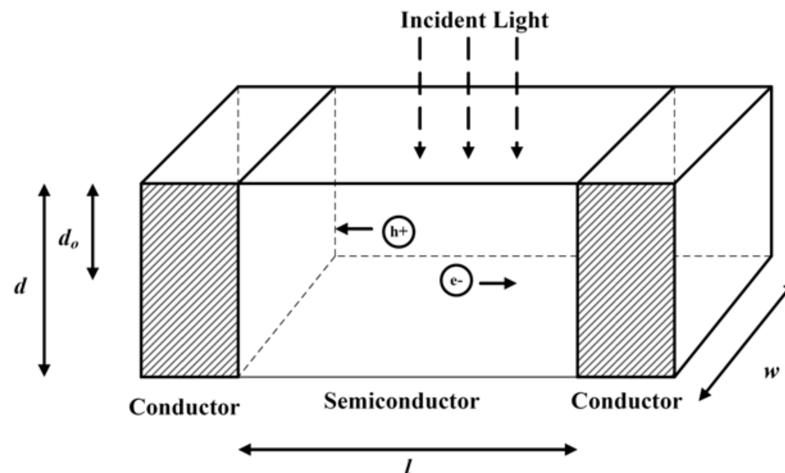

Figure 2.9 Schematic diagram of a photoconductive switch. l and w are the width and length of the semiconductor, respectively. d and d_o are the height of the semiconductor and optical penetration depth, respectively.

The photoconductive switch has two modes of operations: linear mode and non-linear mode. In linear mode operation, each absorbed photon produces an electron-hole pair. In non-linear mode operation, each absorbed photon produces more than one electron-hole pairs by the avalanche process. Hence, this mode of operation requires a high electric field. In this thesis, the study is limited to the linear mode of the photoconductive switch operation.

ATTENTION: The Singapore Copyright Act applies to the use of this document. Nanyang Technological University Library

For photoconductive switch application, the semiconductor region must be highly resistive. The electrical resistance of the photoconductive switch without the incident light or dark electrical resistance, R_{dark} can be expressed as:

$$R_{dark} = \frac{\rho_{dark} l}{wd} \tag{2.18}$$

where ρ_{dark} is the dark electrical resistivity:

With the incident light, the semiconductor absorbs photons and generates electron-hole pairs, leading to a reduction in the electrical resistance of the semiconductor. Assuming the carrier recombination time in the semiconductor is longer than the electrical pulse, the electrical resistance of the semiconductor when the semiconductor is excited by an incident light, R_{light} can be described as [59]:

$$R_{light} = \frac{l^2 E_p}{(1 - R_f)\mu_s q_e E_o} \tag{2.19}$$

where E_p is the energy of the photon, R_f is the surface reflectance, q_e is the electron charge, μ_s is the sum of the electron and hole mobility and E_o is the total optical energy incident on the switch surface. If the electrical pulse is longer than the carrier recombination time in the semiconductor, T_r, R_{light} can be expressed as [60]:

$$R_{light} = \frac{l^2 E_p}{(1 - R_f)\mu_s q_e E_o} \frac{1}{T_r} \tag{2.20}$$

Most of the today's semiconductor photoconductive switches are realized in the planar form as shown in Figure 2.10. In this thesis, the planar type of photoconductive switch was used for microwave switching application. For the application of the photoconductive switch in microwave switching application, a

ATTENTION: The Singapore Copyright Act applies to the use of this document. Nanyang Technological University Library

transmission line which consists of two metal micro strip-lines with a gap between them is deposited on a semiconductor. The microwave signal can transmit across the transmission line when the semiconductor at the gap between the two metal lines becomes conductive by the introduction of the incident light. The absence of the incident light leads to a highly resistive semiconductor material at the gap and thus switches off the transmission of the microwave signal.

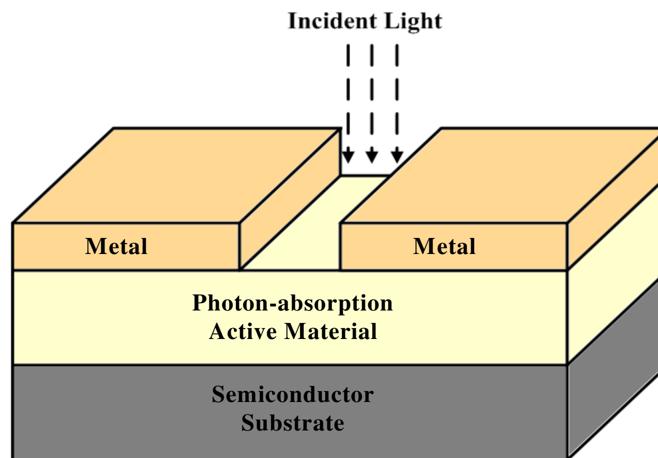

Figure 2.10 Schematic diagram of a planar type of photoconductive switch.

2.2.4 Semiconductor-based optical waveguide

Waveguides are used to confine and guide the light signals to propagate in a pre-determined direction with minimal loss. A waveguide consists of a region with higher refractive index or guiding layer where the light is confined and propagated. The guiding layer is sandwiched by regions of lower refractive index or cladding layer. Semiconductor optical waveguides is one of the most important waveguide which can be realized on various substrates, such as silicon, GaAs and InP. It forms the backbone in many optoelectronic applications. Semiconductor optical

ATTENTION: The Singapore Copyright Act applies to the use of this document. Nanyang Technological University Library

waveguides enable the monolithic integration of various optical devices on a single substrate (chip).

There are basically two types of semiconductor optical waveguides: planar waveguide and channel waveguide. A planar semiconductor optical waveguide is only capable of confining propagated light in one dimension. On the other hand, a channel semiconductor optical waveguide is capable of confining the propagated light in horizontal and vertical directions. In this thesis, the experiment and discussion are confined to the channel semiconductor optical waveguide. There are three types of semiconductor channel optical waveguides, namely rib, ridge and buried waveguides. Figure 2.11 shows the examples of the different channel waveguide structures on an AlGaAs/GaAs/AlGaAs platform grown on GaAs substrates.

The lateral confinement of a rib waveguide is weak as the effective refractive index under the rib is only slightly higher compared to the effective refractive index outside the rib. The confinement of the buried waveguide is ineffective due to the small refractive index differences between the AlGaAs cladding layer and GaAs guiding layer. On the other hand, a ridge waveguide is capable of providing better light confinement in the lateral direction by utilizing the large refractive index difference between the semiconductor (e.g. refractive index of GaAs is 3.3) and air (refractive index of air is 1), or the dielectric materials (e.g. refractive index of SiO_2 or polyimide is ~1.5).

ATTENTION: The Singapore Copyright Act applies to the use of this document. Nanyang Technological University Library

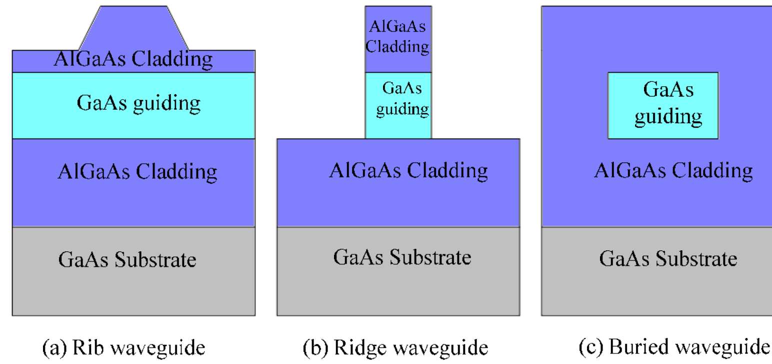

Figure 2.11 Different types of semiconductor channel optical waveguides.

The principle of optical waveguide operation is based on the concept of total internal reflection (TIR). For light traversing from a high refractive index medium to a low refractive index medium, the incident light will be totally reflected back if the incident angle is greater than "critical angle", θ_c. The value of "critical angle" is dependent on the refractive index of the medium and can be expressed as:

$$\sin\theta_C = \frac{n_2}{n_1} \tag{2.21}$$

where n_1 and n_2 are the refractive index of the high refractive index medium and the low refractive index medium, respectively. Therefore, if a high refractive index medium is sandwiched by two low refractive index mediums and the incident light angle is greater than the critical angle, the incident light will be trapped and guided inside the high refractive index medium.

The guiding of light does not occur at all the angles above the critical angle. Due to the constructive and destructive interference of the light inside the guiding medium, the guiding of light occurs only at a few discrete angles. This leads to the presence of different waveguide modes. Each waveguide mode corresponds to a specific

ATTENTION: The Singapore Copyright Act applies to the use of this document. Nanyang Technological University Library

value of the incident angle. The value of incident angle, θ_m that allows the guiding of light, can be expressed as:

$$\left(\frac{2\pi n_1 d}{\lambda}\right)\cos\theta_m - \phi_m = m\pi \tag{2.22}$$

where d is the thickness of the high refractive index medium, λ is the wavelength of the guided light, ϕ_m is the phase change of the light induced by the TIR and m is an integer.

Generally, the refractive index of a semiconductor material is inversely proportional to its bandgap. Thus, two wide bandgap cladding layers and a narrow bandgap guiding layer are needed to form a semiconductor waveguide. Apart from the bandgap, the refractive index is also affected by the free-carrier concentration in the semiconductor layer. The free carriers reduce the refractive index at the photon energy below and near the bandgap energy. The change in the refractive index due to the free carriers, Δn is ~-1×10^{-20} N cm^{-3} for N of up to 1×10^{18} cm^{-3}. N is free carrier concentration.

In this thesis, the performance of a waveguide was characterized by the propagation loss of the waveguide. The magnitude of the propagation loss of a waveguide depends on the confinement of the propagated light in the waveguide and the absorption of the propagated light in the guiding layer. The former depends on the refractive index contrast between the cladding and guiding layers, while the latter can be influenced by the material defects in the guiding layer which is detrimental to the waveguide performance.

ATTENTION: The Singapore Copyright Act applies to the use of this document. Nanyang Technological University Library

Chapter 3 Growth and characterization of GaNAsSb

3.1 Growth of GaNAsSb material using molecular beam epitaxy system

The growth of GaNAsSb and other III-V compound semiconductor material described in this thesis was performed using a solid source MBE system. Solid source MBE is an ultra-high vacuum (UHV) crystal epitaxy technique based on reaction of molecular or atomic beams on a heated substrate. It is capable of producing extremely high purity and highly crystalline thin films with precisely control over composition and doping by using mostly elemental sources. Its atomic layer epitaxy ensures abrupt interfaces in the fraction of nanometer range in the growth direction with precise lateral uniformity.

Due to the ultra-high vacuum environment inside a MBE system, the mean free path of the molecules from various sources is typically of the order of tens of meters and longer than the distance between the source and substrate. Thus, molecules arriving at the substrate travel in a beam-like and directional manner. To maintain the ultra-high vacuum environment, MBE systems are equipped with complex vacuum pumping systems which comprise ion pumps, turbo pump and Ti-sublimation pump. In addition, liquid N_2 cryo-panels are placed around the chamber to preserve the UHV condition during growth, where the typical pressure is ~10^{-7}–10^{-8} torr. Furthermore, a sample loading chamber and transfer chamber are connected to the MBE chamber to ensure the cleanliness of the substrate loading process by isolating the MBE chamber from the atmosphere.

ATTENTION: The Singapore Copyright Act applies to the use of this document. Nanyang Technological University Library

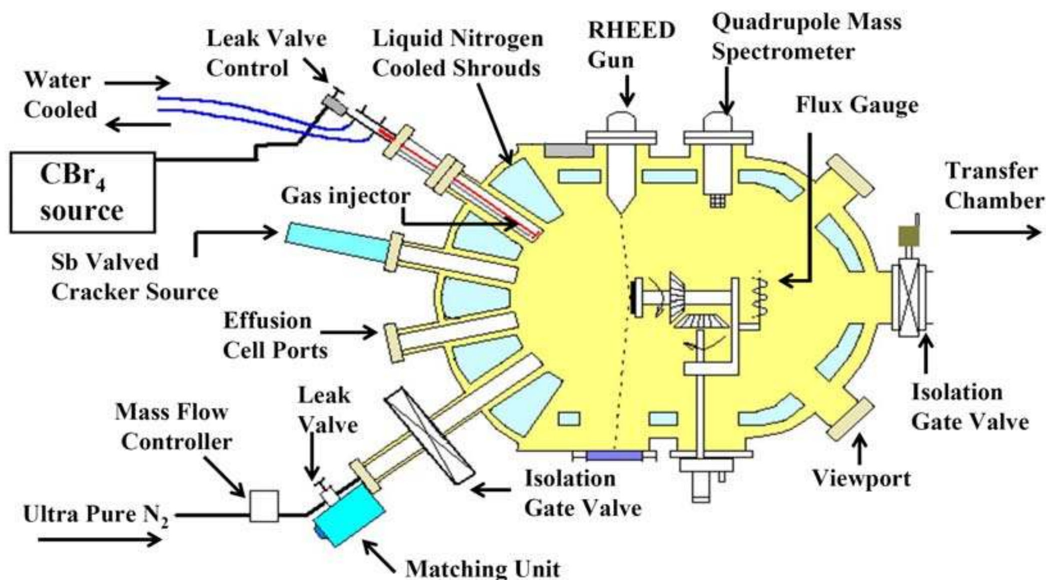

Figure 3.1 Schematic diagram of a typical Solid source molecular beam epitaxy system equipped with RF plasma N source, As and Sb valved-cracker cells.

Figure 3.1 shows the schematic of the solid source MBE growth chamber used in the growth of samples reported in this thesis, with some of the major components such as:

- Standard Knudsen effusion cells for the group III elements (Ga, Al, In) and n-type dopant (Si). The materials are in high purity pyrolytic boron nitride (PBN) crucibles, which can withstand high temperature due to its high dissociation temperature (>1400 °C). Individual mechanical shutters are placed in front of the cells to achieve precise control of the beam fluxes. These cells are kept at standby temperatures (600°C for Ga cell, 450°C for In cell, 750°C for Al cell and 600°C for Si cell) when they are not in

ATTENTION: The Singapore Copyright Act applies to the use of this document. Nanyang Technological University Library

operation. During the growth, their temperatures are increased to between 750°C to 1200°C to achieve the desired beam flux for the growth.

- Valved cracker cells were used for group V elements (As and Sb) due to their higher vapor pressure than the group III elements. The use of valved cell allows precise control and delivery of the group V flux while preventing quick depletion of the source materials. With the valved cracker cell, abrupt transition between two different group V materials during the growth can be achieved.
- RF N_2 plasma source. High purity N_2 gas is cracked using the RF Plasma. The resulting N atoms are used to form the dilute nitride (III-V-N) compound semiconductor epilayer.
- Carbon tetrabromide (CBr_4) source was used as the p-type dopant. The use of carbon dopant avoids the out-diffusion problem faced by other popular choices of p-type dopants in GaAs, such as beryllium and zinc.
- In addition to the III-V and doping sources, the UHV environment allows *in-situ* characterization with reflection high energy electron diffraction (RHEED). The RHEED technique helps to monitor the surface reconstruction during the growth. The quadruple mass spectrometer (QMS) helps to monitor the atomic and molecular species inside the chamber. The MBE chamber is equipped with two ion gauges to monitor the background pressure of the chamber and to measure the beam flux of the III-V sources. Furthermore, the chamber is also equipped with a substrate holder/manipulator that allows substrate heating and substrate rotation.

ATTENTION: The Singapore Copyright Act applies to the use of this document. Nanyang Technological University Library

The growth of the GaNAsSb material in the experiments reported in this thesis used a high purified nitrogen gas. The gas flow rate of the nitrogen gas was between 0.26 to 0.33sccm. The background vacuum pressure in the chamber during the growth of GaNAsSb was ~1×10^{-5} torr. During the growth of the GaNAsSb layer, the variation of the nitrogen plasma RF power changed the amount of N content in the epilayer. In the experiments reported in this thesis, the RF plasma power of the nitrogen plasma was between 200 to 500W during the growth of GaNAsSb layer. This resulted in a GaNAsSb layer with 1 to 4% of nitrogen content. The impedance of the plasma source was tuned to achieve zero reflected power in the plasma.

The Sb source uses a needle valve and mechanical shutter to control the Sb content in the GaNAsSb layer. During the growth of GaNAsSb layer, the temperature of the Sb source reservoir was between 520 to 540°C. This resulted in Sb beam equivalent pressures of between 5×10^{-8} to 2×10^{-7} torr, leading to a GaNAsSb layer with 5 to 18% of Sb content. Moreover, the cracker temperature of the Sb source was set to 900°C. Brewer *et al.* [61] have reported that a cracker temperature of 900°C leads to a complete conversion of Sb_4 molecules to atomic Sb, as shown in Figure 3.2. The use of atomic Sb in the growth increases the incorporation efficiency of Sb species and improves the quality of the epitaxy material.

ATTENTION: The Singapore Copyright Act applies to the use of this document. Nanyang Technological University Library

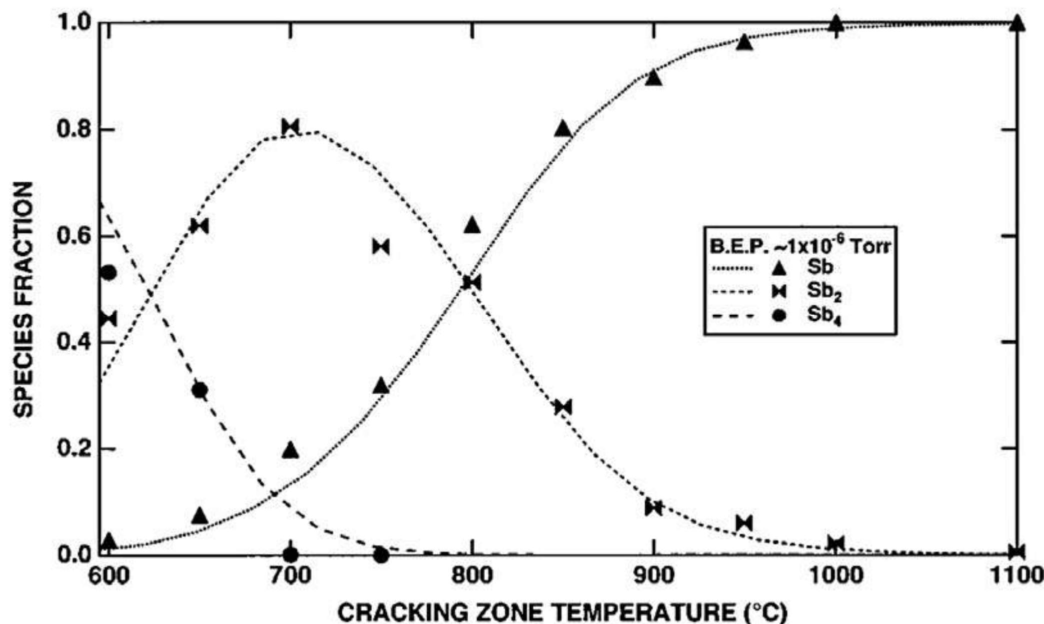

Figure 3.2 The product distribution of an antimony cracker cell is shown as function of cracker zone temperature. Experimentally measured values are indicated by solid symbols: Sb (triangles), Sb_2 (bow ties) and Sb_4 (circles) [61].

3.2 Determination of N and Sb content in GaNAsSb using x-ray diffraction

The determination of N and Sb concentration is very critical in the growth of GaNAsSb material. Incorrect composition of N and Sb in the GaNAsSb can result in an incorrect bandgap energy and lattice constant of the GaNAsSb material. X-ray diffraction (XRD) is a fast turnaround, cost effective and non-destructive way to determine the content of Sb and N in the GaNAsSb material.

ATTENTION: The Singapore Copyright Act applies to the use of this document. Nanyang Technological University Library

The x-ray diffraction from crystal planes is governed by the Bragg Law, which can be expressed as:

$$\lambda = d_{hkl} \sin 2\theta \tag{3.1}$$

where λ is the x-ray wavelength, θ is the diffraction angle and d is the spacing between (hkl) planes. The d for cubic crystal can be expressed as:

$$d_{hkl} = \frac{a}{\sqrt{h^2 + k^2 + l^2}} \tag{3.2}$$

where a is the lattice constant of the cubic crystal and the h, k and l are the Miller indices number corresponding to the (hkl) plane.

Atomic concentration of ternary materials can be obtained by fitting the (004) rocking curves of the XRD spectra with the simulated curves generated by the X'Pert Epitaxy simulator based on the dynamical diffraction theory of Halliwell *et al.* [62]. However, the determination of N and Sb concentration using the (004) rocking curve in quaternary materials, such as GaNAsSb are more complicated because it involves two unknown variables: the concentration of N atoms and the concentration of Sb atoms. Thus, a calibration sample is needed to determine the concentration of N and Sb prior to growth of device samples containing the GaNAsSb material.

The structure of the calibration sample is shown in Figure 3.3. It consists of a 50nm-thick GaAsSb layer and followed by a 200nm-thick GaNAsSb layer. The Sb flux was kept unchanged during the growth of both layers. The (004) rocking curve of the calibration sample is shown in Figure 3.4. The concentration of Sb atoms in both layers was firstly determined by fitting the rocking curve of the

ATTENTION: The Singapore Copyright Act applies to the use of this document. Nanyang Technological University Library

GaAsSb layer. Since the Sb flux was kept unchanged during the growth of the GaAsSb and GaNAsSb layers, it is expected that both layers contain equal amount of Sb. SIMS measurement results in the previous study [63] confirmed that the difference of Sb concentration in these two layers is <0.4±0.2%, leading to only <0.01eV difference in bandgap energy. This difference is negligible. Using the value of Sb concentration in the GaAsSb layer, the concentration of N atoms in the GaNAsSb layer can be determined by fitting the rocking curve of the GaNAsSb layer.

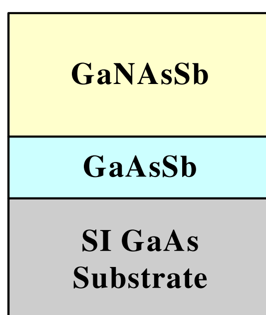

Figure 3.3 Schematic diagram of calibration sample used to determine concentration of N and Sb atoms in GaNAsSb material.

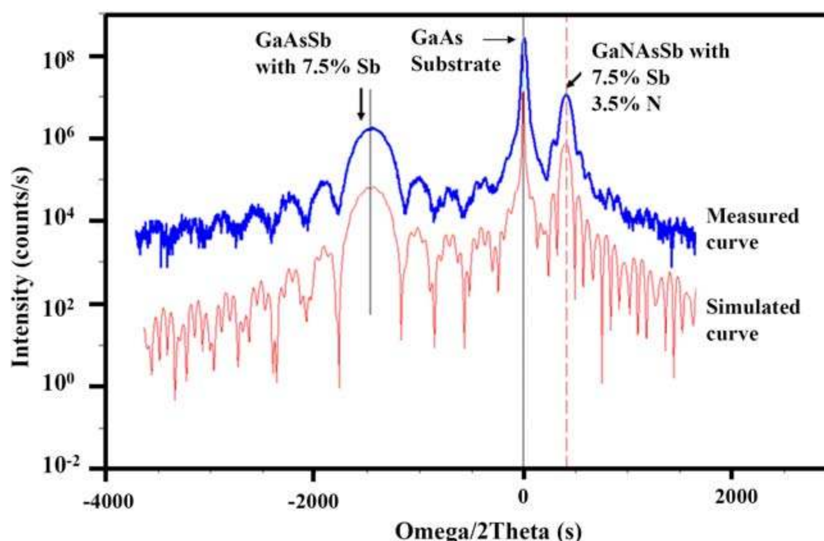

Figure 3.4 XRD (004) rocking curve of calibration sample. The red simulation curve is used to determine the concentration of Sb and N in the material.

ATTENTION: The Singapore Copyright Act applies to the use of this document. Nanyang Technological University Library

3.3 Modification of the nitrogen RF plasma source

N_2 is supplied to the nitrogen source during the growth of the GaNAsSb material. N_2 is a stable and non-reactive species. Thus, additional energy is needed to break the triple bonds in N_2 molecules to produce atomic nitrogen which is responsible for the growth of the dilute nitride material. During the process of exciting the nitrogen gas using plasma or ion-beam source, atomic nitrogen is generated along with other nitrogen species which have large kinetic energies. The impingement of these energetic nitrogen species on the substrate surface generates unwanted defects in the epitaxy layer.

To improve the material quality, an ideal nitrogen plasma source should have low ion energy and small ion flux. The reactive ion (RI) plasma [64] generates ions with energies of between 35 to 90eV and ion fluxes of between 3×10^{14} and 3×10^{15} $cm^{-2}s^{-1}$ at the substrate. The ion flux arriving at the substrate is 1.1×10^{12} $cm^{-2}s^{-1}$ in the RF plasma source [65], much lower compared to the ion flux in the RI plasma. Moreover, the energy of the ions in the RF plasma is approximately 10eV, much lower compared to the energy of the ions in the electron cyclotron resonance (ECR) plasma which is >15eV [65, 66]. This makes the nitrogen RF plasma source, the most suitable atomic nitrogen source for the growth of the GaNAsSb material.

Although the RF plasma source has the smallest ion flux among all types of

ATTENTION: The Singapore Copyright Act applies to the use of this document. Nanyang Technological University Library

plasma sources, it is still far from perfect. Its ion flux still contributes to the obvious deterioration in the quality of the dilute nitride material. Studies have shown that the ion flux induces surface damage, leading to low intensity and red shift in the photoluminescence (PL) spectrum [66]. To improve the material quality by reducing the ion flux of the RF plasma source arriving onto the film surface, the nitrogen RF plasma source was modified to include an ion deflection plates system.

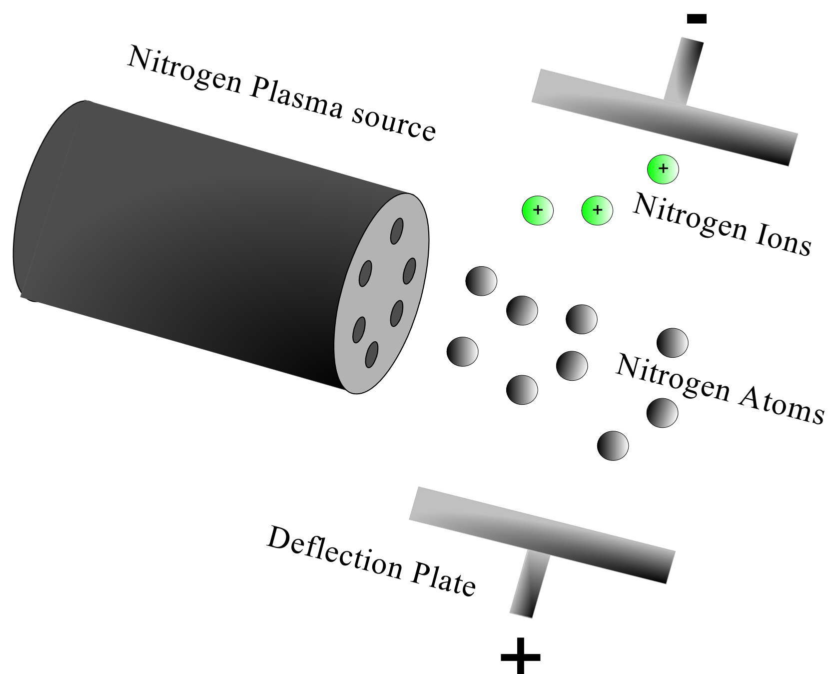

Figure 3.5 Schematic diagram of the ion deflection plates. Nitrogen ions are deflected towards the negatively biased plate.

Figure 3.5 shows the schematic diagram of the ion deflection plates. The ion deflection plates system consists of a pair of parallel steel plates positioned at the

ATTENTION: The Singapore Copyright Act applies to the use of this document. Nanyang Technological University Library

output of the plasma source. The direction of these two plates is perpendicular to the direction of plasma flux. A bias voltage is applied to provide an electric field across the ion deflection plates, diverting the charged ions from arriving at the substrate along with nitrogen atoms.

To optimize the bias voltage, six GaNAs samples were grown at different bias voltages (-60V, -40V, -20V, 20V, 40V and 60V) of the ion deflection plates. Furthermore, one GaNAs sample was grown at bias voltage of 0V as the control sample. These samples were grown on a semi-insulating GaAs substrate. The thickness of the GaNAs layers was 50nm. The PL spectra of these samples and its intensity were measured and shown in Figures 3.6 and 3.7.

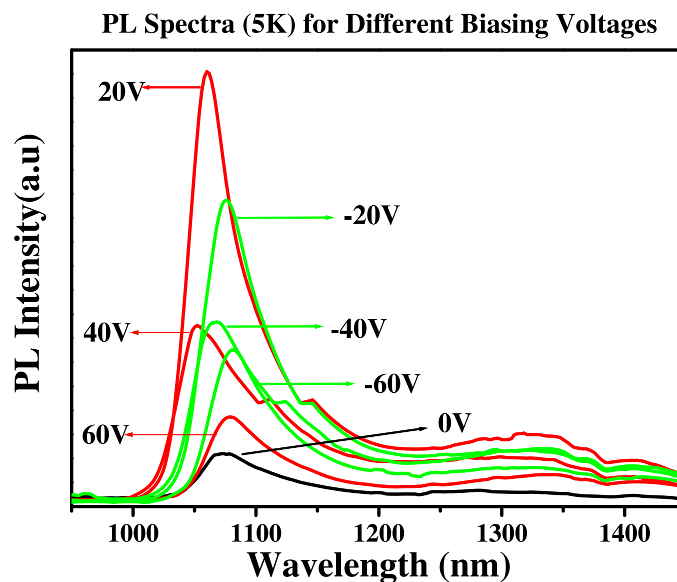

Figure 3.6 PL spectra (5K) of GaNAs samples under different bias voltages.

As shown in Figures 3.6 and 3.7, the PL intensity for samples grown with bias voltage was higher compared to that of the sample grown without bias voltage.

ATTENTION: The Singapore Copyright Act applies to the use of this document. Nanyang Technological University Library

Compared to the sample grown without bias voltage, the sample grown with bias voltage of 20V across the ion deflection plates shows its PL intensity increases by a factor of 7. The increase in the PL intensity implies a significant reduction in the defects and improvement in the material quality.

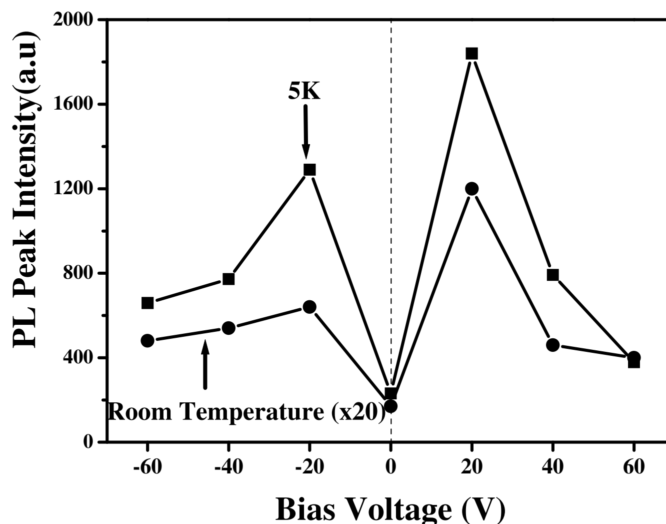

Figure 3.7 Plot of PL intensity at 5K (■) and at room temperature (•) of GaNAs samples *vs.* deflection plate bias voltages.

Further increase in the bias voltage (from 20V to 40V or 60V) does not increase the PL intensity. On the contrary, the PL intensity reduces as the bias voltage increases further. One possible explanation of this phenomenon is that the bias voltage of >20V across the ion deflection plate results in high energy in the ions. These ions acquire energy from the electric field during the ion deflection process. The ion deflection plate diverts these energetic ions to the direction of the chamber wall. The bombardment of these high energy ions onto the chamber wall could

ATTENTION: The Singapore Copyright Act applies to the use of this document. Nanyang Technological University Library

lead to the release of unwanted species into the growth chamber and contaminate the epitaxy layer.

The samples were also characterized using XRD to investigate the nitrogen content in each sample. From Figure 3.8, it can be seen that the XRD rocking curve peak position of the GaNAs layer does not change significantly at different ion deflection plate bias voltages. This indicates that the nitrogen content in the samples is not affected by the bias voltage across the ion deflection plate. As the bias voltage across the ion deflection plates reduces the ions flux arriving onto the substrate, the lack of nitrogen content variation in the samples grown at different bias voltage across the ion deflection plates also indicates that nitrogen-related ions do not contribute to the nitrogen content in the dilute nitride material.

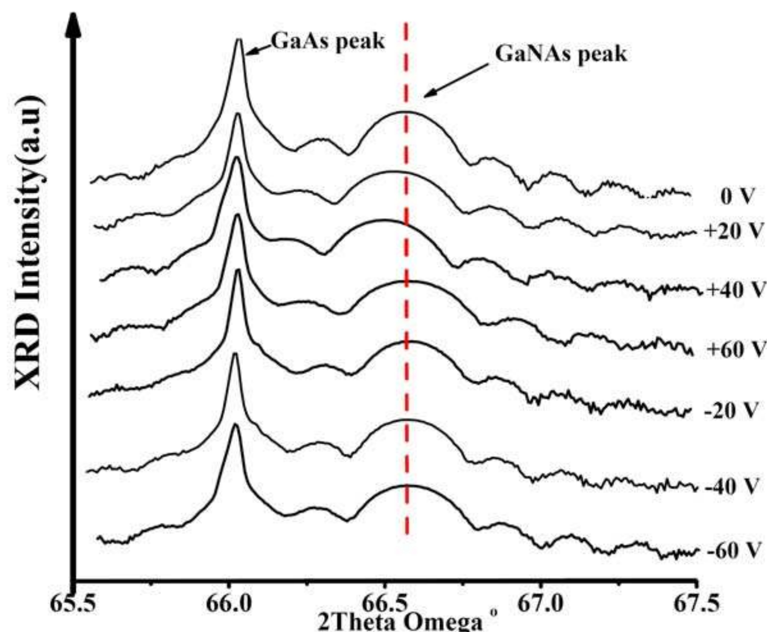

Figure 3.8 XRD rocking curve of GaNAs samples grown under different bias voltages.

ATTENTION: The Singapore Copyright Act applies to the use of this document. Nanyang Technological University Library

Chapter 4 GaNAsSb-based p-i-n photodetector

4.1 Photodetector responsivity

4.1.1 Introduction

Achieving high photoresponsivity is one of the key challenges in GaAs-based dilute nitride photodetector research. So far, reported results of GaAs-based dilute nitride photodetectors can be categorized into two groups: one based on quantum well (QW) absorption layers [14-16] and the other based on bulk absorption layers [28, 42-44, 67, 68]. In the devices based on a quantum well absorption layer, a thin dilute nitride layer (<10nm) is used. While such QW devices enable the utilization of highly strained dilute nitride layers and thus offer photo-response up to 1.6µm, their photoresponsivity is generally low [15, 16] (typically less than 0.03A/W) due to the thin QW photon-absorption layer. To overcome this limitation [14], resonant cavity has been incorporated into the device structure. On the other hand, photodetectors based on bulk dilute nitride absorption layers (>0.4µm-thick) suffer from reduced photo-response at wavelengths longer than 1µm. So far, the highest reported cutoff wavelength is ~1.4µm [43]. This is due to the difficulty in incorporating more than 3.5% of nitrogen into the material. Nevertheless, photodetectors based on bulk dilute nitride absorption layer exhibit higher photoresponsivity compared to QW-based devices. Recently, photoresponsivities of up to about 0.1A/W at 1.3µm have been reported for bulk GaNAsSb-based

ATTENTION: The Singapore Copyright Act applies to the use of this document. Nanyang Technological University Library

devices [67-69]. However, these photoresponsivity values are still much lower compared to those of commercial InGaAs photodetectors, with typical photoresponsivity of up to ~0.9A/W at 1.3μm.

In this section, significant improvement in the photoresponsivity of GaNAsSb-based p-i-n photodetectors with a GaNAsSb bulk photon-absorption layer at 1.3μm wavelength is reported. This improvement is achieved by manipulating the level of defects (nitrogen-related defects and arsenic antisite defects) concentration in the GaNAsSb layer using the growth temperature of the i-GaNAsSb layer. Furthermore, the photodetectors exhibit characteristics which strongly suggest the presence of photogenerated carrier multiplication due to the avalanche effect.

4.1.2 Growth of GaNAsSb-based p-i-n photodetectors

The device structure shown in Figure 4.1 was grown using a MBE system in conjunction with an RF N plasma source and a valved Sb cracker source. The 0.5μm i-GaNAsSb (bulk) photon-absorption layer was grown at 350°C, 400°C, 440°C and 480°C. The RF nitrogen plasma power was 180W and the beam equivalent pressure (BEP) of the Sb flux was ~1×10^{-7} torr. Under these conditions ~3.3% of N and 8% of Sb were incorporated into the i-GaNAsSb layer, which was confirmed by XRD. Using the BAC model [55], the optical bandgap of the

ATTENTION: The Singapore Copyright Act applies to the use of this document. Nanyang Technological University Library

i-GaNAsSb layer was estimated to be ~0.9eV. The doping concentrations of the p-type (C-doped) and n-type (Si-doped) GaAs contact layers were approximately $2\times10^{19}cm^{-3}$ and $5\times10^{18}cm^{-3}$, respectively and the growth temperature of these layers was 600°C.

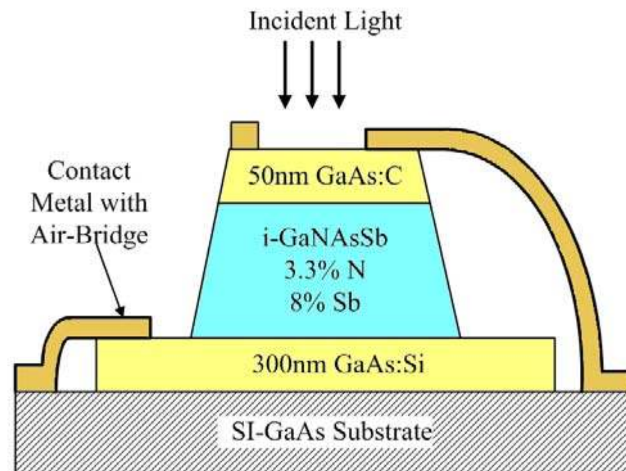

Figure 4.1 Schematic diagram of GaNAsSb-based p-i-n photodetector structure.

4.1.3 Results of Photoresponsivity measurement

The photoresponsivity measurements were carried out using a quartz tungsten halogen lamp as the light source in conjunction with a monochromator. Calibration of the light source was done using a commercial InGaAs photodetector. Figure 4.2(a) shows the spectral response at reverse bias of 3V *vs.* wavelength for the devices whose i-GaNAsSb layers were grown at 350°C to 480°C. The photodetectors show photo-response up to wavelength of at least 1350nm. Figure 4.2(b) shows the photoresponsivity at different reverse biases measured at wavelength of 1300nm.

ATTENTION: The Singapore Copyright Act applies to the use of this document. Nanyang Technological University Library

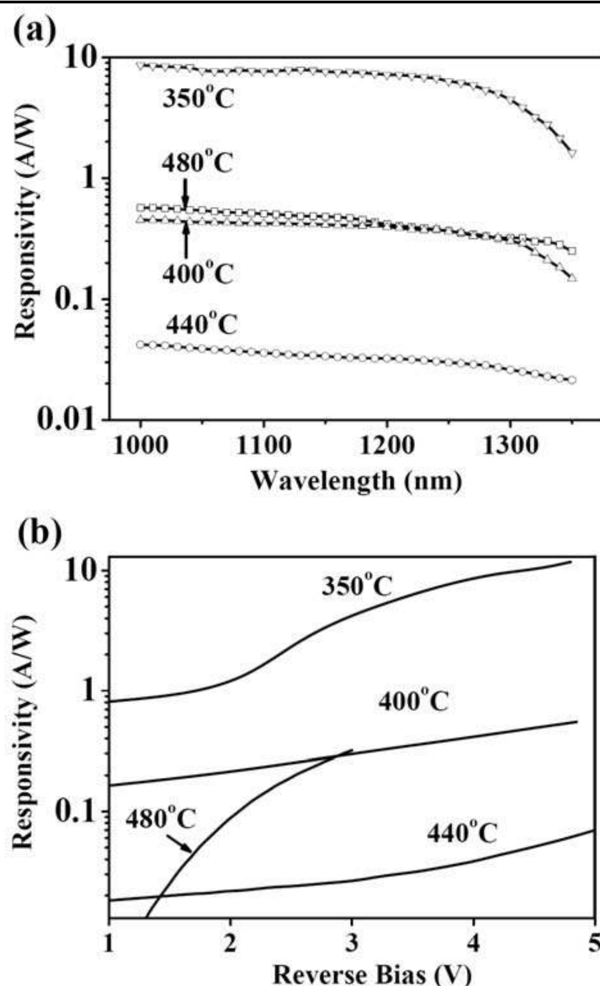

Figure 4.2 (a) Spectral response of devices with i-GaNAsSb layer grown at 350°C, 400°C, 440°C and 480°C, measured at reverse bias voltage of 3V. (b) Plot of photoresponsivity *vs*. reverse bias for devices with i-GaNAsSb layer grown at 350°C, 400°C, 440°C and 480°C measured at 1300nm.

From Figure 4.2(b), it is interesting to note that the photodetector with GaNAsSb layer grown at 350°C shows an extremely high photoresponsivity value of ~12A/W under reverse bias of 4.8V at 1300nm. This is more than 2 orders higher than previously reported results. Assuming unity quantum efficiency, a 1.3μm

ATTENTION: The Singapore Copyright Act applies to the use of this document. Nanyang Technological University Library

photodetector has maximum responsivity of ~0.75A/W after taking into account 29% incident power reflection. This incident power reflection is due to the refractive index difference at the air/GaAs interface. Thus, photoresponsivity value of 12A/W implies a quantum efficiency value significantly larger than 1, possibly due to the presence of an avalanche carrier multiplication effect.

From Figures 4.2(a) and 4.2(b), it can also be seen that the photoresponsivity of the devices increases as the growth temperature of the i-GaNAsSb photon-absorption layer decreases, except for the device with the i-GaNAsSb layer grown at 480°C. It can be seen in Figure 4.2(b), the photoresponsivity of the device grown at 480°C is the lowest at reverse biases below 1V, confirming that the responsivity generally decreases with increasing growth temperature. However, as the reverse bias is increased, the responsivity of the device with i-GaNAsSb layer grown at 480°C rises much stronger as compared to the other devices. This behavior will be further explained below.

4.1.4 Photocurrent multiplication in GaNAsSb-based p-i-n photodetectors

The unintentional doping concentration in the i-GaNAsSb layer can be associated with the nitrogen-related defects which have energy states ~0.1eV above the valence band [28, 44]. At room temperature, ~0.05% of the nitrogen-related defect states is thermally activated and contributes to unintentional doping concentration.

ATTENTION: The Singapore Copyright Act applies to the use of this document. Nanyang Technological University Library

From capacitance-voltage (C-V) measurements, the unintentional doping concentrations in the i-GaNAsSb layer grown at 350°C, 400°C, 440°C and 480°C were determined to be 2×10^{16}cm^{-3}, 6×10^{16}cm^{-3}, 3×10^{17}cm^{-3} and 1.5×10^{18}cm^{-3}, respectively as shown in Figure 4.3. The unintentional doping is p-type. The result indicates that decreasing growth temperature reduces the amount of nitrogen-related defects in the GaNAsSb layer. A similar relation between the growth temperature and nitrogen-related defects was also reported for the GaNAs material [70].

The unintentional doping concentration in GaNAsSb decreases rapidly as the measurement temperature decreases. This is due to high activation energy of the nitrogen-related defects (~0.1eV) compared to that of conventional dopants such as Zn. The activation energy of Zn is 0.025eV. The unintentional doping concentration of all samples falls below 1×10^{15}cm^{-3} at temperature below 150K.

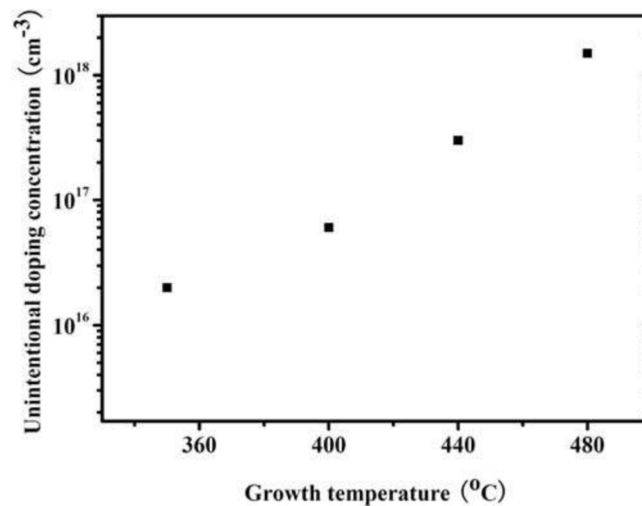

Figure 4.3 Unintentional doping concentration in GaNAsSb at different growth temperatures.

ATTENTION: The Singapore Copyright Act applies to the use of this document. Nanyang Technological University Library

The depletion region width in the i-GaNAsSb layer at different reverse biases can be calculated based on these measured unintentional doping concentrations. Furthermore, from the refractive index measurement (details of this measurement are described in chapter 6) [71], the absorption coefficient α was measured using a spectroscopic ellipsometer and has a value of $1.3\times10^{4}cm^{-1}$ at wavelength of 1300nm. Using the measured photoresponsivity values, calculated depletion region widths and values of α, the photocurrent multiplication factor, M for all devices at different reverse biases is calculated and shown in Figure 4.4.

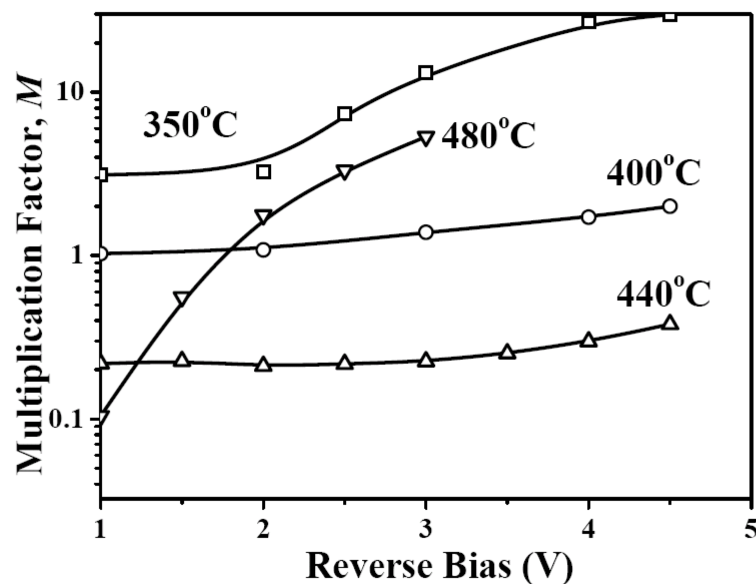

Figure 4.4 Plot of multiplication factor M as function of reverse bias voltage measured at 1300nm for devices with i-GaNAsSb layer grown at 350°C, 400°C, 440°C and 480°C.

From Figure 4.4, it can be seen that the photodetector with the i-GaNAsSb layer grown at 350°C has a M value of ~30 at reverse bias voltage of 4.5V. This high

ATTENTION: The Singapore Copyright Act applies to the use of this document. Nanyang Technological University Library

value of M confirms the earlier suggestion of the presence of photogenerated carrier multiplication due to the avalanche effect. As the carrier avalanche effect is directly dependent on the electric field strength at the depletion region, the values of M in Figure 4.4 are re-plotted against the average electric field strength at the depletion region and shown in Figure 4.5.

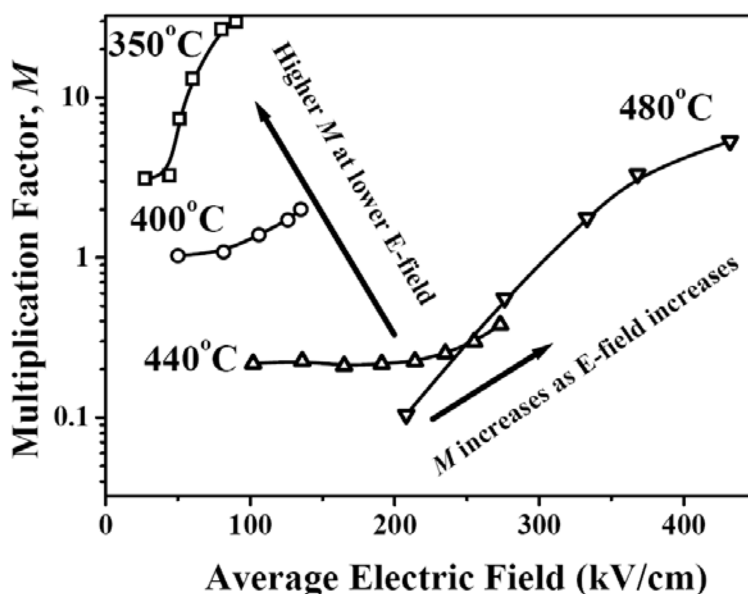

Figure 4.5 Plot of multiplication factor M as function of average electric field measured at 1300nm for devices with i-GaNAsSb layer grown at 350°C, 400°C, 440°C and 480°C.

As mentioned earlier, the photodetector whose i-GaNAsSb layer was grown at 480°C showed a different characteristic where photoresponsivity rises much stronger with increasing reverse bias as compared to the other devices. At high reverse voltages (>1.5V), it exhibits higher responsivity compared to the device with the i-GaNAsSb layer grown at 440°C. This can be explained by the high

ATTENTION: The Singapore Copyright Act applies to the use of this document. Nanyang Technological University Library

electric field in the depletion region of this device which is shown in Figure 4.5.

Due to the high unintentional doping concentration of $1.5\times10^{18}cm^{-3}$ in the i-GaNAsSb layer grown at 480°C, the resulting depletion region is comparably thin (<0.1μm). The thin depletion region results in high electric field strength of about 200-400kV/cm at the depletion region. The electric field strength value of 200-400kV/cm is normally associated with the initialization of a carrier avalanche process in the depletion region. This contrasts with the other devices which exhibit an average electric field strength of <200kV/cm in their depletion regions. Therefore, the rapid increase in the photoresponsivity with increasing reverse bias of the photodetector with the i-GaNAsSb layer was grown at 480°C is due to the high electric field strength at its depletion region. The high electric field strength results in higher carrier multiplication.

4.1.5 Carrier avalanche process at low electric field

It is interesting to note that as the growth temperature of the i-GaNAsSb layer deceases from 440°C to 350°C, the devices show a higher value of M, even at much lower electric fields. Furthermore, the photodetector with the i-GaNAsSb layer grown at 350°C exhibits a high carrier multiplication factor at average electric field strengths of <100kV/cm. Even after considering a non-uniformly distributed electric field in the depletion region, the maximum electric field strength is ~100kV/cm and 180kV/cm at reverse bias of 1V and 5V, respectively.

ATTENTION: The Singapore Copyright Act applies to the use of this document. Nanyang Technological University Library

This electric field strength is unexpectedly low to initialize a carrier avalanche process. The GaAs or InGaAs-based avalanche photodetectors only show carrier multiplication at electric field strength higher than ~200kV/cm [72, 73]. These results suggest that decreasing the growth temperature of the i-GaNAsSb layer leads to a higher impact ionization coefficient in the material. The higher impact ionization coefficient in the material results in the initiation of a carrier avalanche process at low electric field.

The high ionization coefficient and initiation of the carrier avalanche process at low electric field in the photodetector with the low temperature grown i-GaNAsSb layer could be explained by the existence of mid-gap As antisite defects (As_{Ga}) in the material. It is known that dilute nitride materials contain As_{Ga} defects [30, 44] when they are grown at low temperature (<500°C). It is expected that the i–GaNAsSb layer grown at 350°C has the highest concentration of As_{Ga} defects compared to i-GaNAsSb layer grown at higher temperature. The concentration of the As_{Ga} defects increases in response to the decrease in the growth temperature of the dilute nitride material [30].

Generally, carriers in a p-n junction require energy of $\frac{3}{2}E_g$ to start an impact ionization and thus an avalanche process [74-76]. E_g is the bandgap energy of the material. Mid-gap defects such as As_{Ga} are reported [77] to enhance the impact ionization process by lowering the energy required in the impact ionization process. The impact ionization process assisted by the mid-gap defects only requires energy

ATTENTION: The Singapore Copyright Act applies to the use of this document. Nanyang Technological University Library

of $\frac{E_g}{2}$ [77]. By lowering the required energy, the existence of mid-gap defects enables a more efficient impact ionization and carrier multiplication process at a lower electric field. This explains the observation that photodetectors, which have the i-GaNAsSb layer containing more As_{Ga} defects have higher carrier multiplication. The As_{Ga} defects help to initialize the impact ionization process at a lower electric field.

4.1.6 Summary

In summary, section 4.1 reports significant improvement in the photoresponsivity of 1.3µm GaNAsSb-based p-i-n photodetectors with a GaNAsSb bulk photon-absorption layer. This improvement is achieved by manipulating the level of defects (nitrogen-related defects and arsenic antisite defects) concentration in the GaNAsSb layer using the growth temperature of the i-GaNAsSb layer as the control parameter. By lowering the growth temperature of the GaNAsSb layer, the nitrogen-related defects can be reduced, leading to lower unintentional doping and thus, a thicker depletion region. Furthermore, lower growth temperature also increases the concentration of arsenic antisite defects. Higher concentration of arsenic antisite defects is found to enhance the carrier avalanche process. With the thicker depletion region and carrier avalanche process, the photodetector with the i-GaNAsSb layer grown at 350°C exhibits record photoresponsivity of ~12A/W. This is the highest photoresponsivity value ever reported for a dilute nitride-based photodetector.

ATTENTION: The Singapore Copyright Act applies to the use of this document. Nanyang Technological University Library

4.2 High frequency performance of the photodetectors

4.2.1 Introduction

One of the key challenges in GaAs-based dilute nitride photodetectors is to obtain a high frequency response. Recent reports [13, 14] on dilute nitride-based photodetectors have shown 800ps rise time in GaInNAs RCE quantum well devices. Previous measurements of GaNAsSb-based p-i-n photodetectors [28] have shown a RC delay limited 3dB cutoff frequency f_T between 920MHz to 1.4GHz. So far, there has been no report on dilute nitride-based photodetectors with f_T exceeding these values. In this section, the multi-GHz high-frequency performance of GaNAsSb-based p-i-n photodetectors is discussed.

4.2.2 Growth and fabrication of GaNAsSb-based p-i-n photodetectors

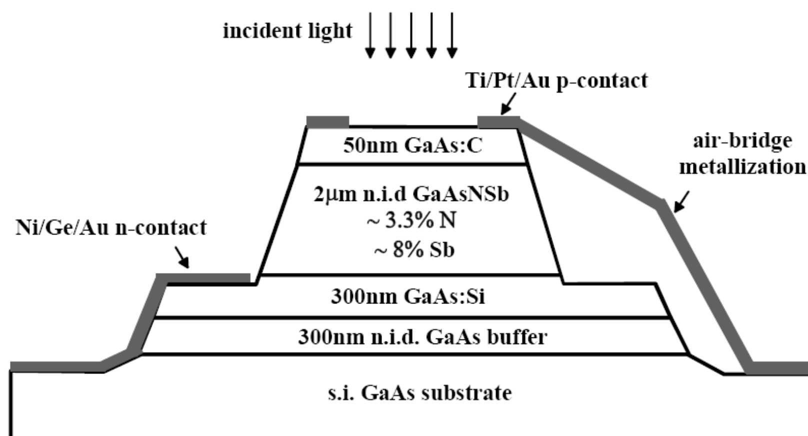

Figure 4.6 Cross section schematic diagram of the GaNAsSb-based p-i-n photodetector mesa structure.

ATTENTION: The Singapore Copyright Act applies to the use of this document. Nanyang Technological University Library

The device structure shown in Figure 4.6 was grown using a MBE system in conjunction with a RF N plasma source and a valved cracker source for Sb. The photodetectors use low-loss 50Ω coplanar feed-lines, air-bridge metallization and a thick non-intentionally doped (n.i.d.) absorption layer to assure a small RC time constant and reasonably large photoresponsivity.

The GaAs buffer and GaAs:C (p-type) and GaAs:Si (n-type) layers were grown at 600°C while the n.i.d. GaNAsSb layer was grown at 440°C at RF plasma power of 300W. The doping concentrations of the p- and n-doped contact layers are approximately 2×10^{19}cm^{-3} and 5×10^{18}cm^{-3}, respectively. The beam equivalent pressure (BEP) of the Sb flux was ~1×10^{-7} torr. Under these conditions, ~3.3% of nitrogen and 8% of Sb were incorporated into the GaNAsSb layer which was confirmed by XRD. Using the BAC model [55], the optical bandgap of the i-GaNAsSb layer was estimated to be ~0.9eV.

GaNAsSb photodetectors with different diameters were fabricated using a high-speed microwave design with coplanar feed-lines. Standard optical lithography was used for defining the different mask layers. Ohmic p and n contacts were formed by 320nm-thick Ti/Pt/Au and 400nm-thick annealed Ni/Ge/Au metallization, respectively. Wet chemical mesa etching of the 2µm-thick GaNAsSb material was performed using diluted NH_4OH:H_2O_2 in a three step

ATTENTION: The Singapore Copyright Act applies to the use of this document. Nanyang Technological University Library

process in order to control the mask under cut. The etch rate of the GaNAsSb material was determined to be 7.2nm/s. The photodetectors were placed in a 50Ω ground-signal ground (GSG) pad. The devices also used air-bridge metallization technology. Photographs of the fabricated GaNAsSb photodetector taken by an optical microscope and a scanning electron microscope are shown in Figure 4.7.

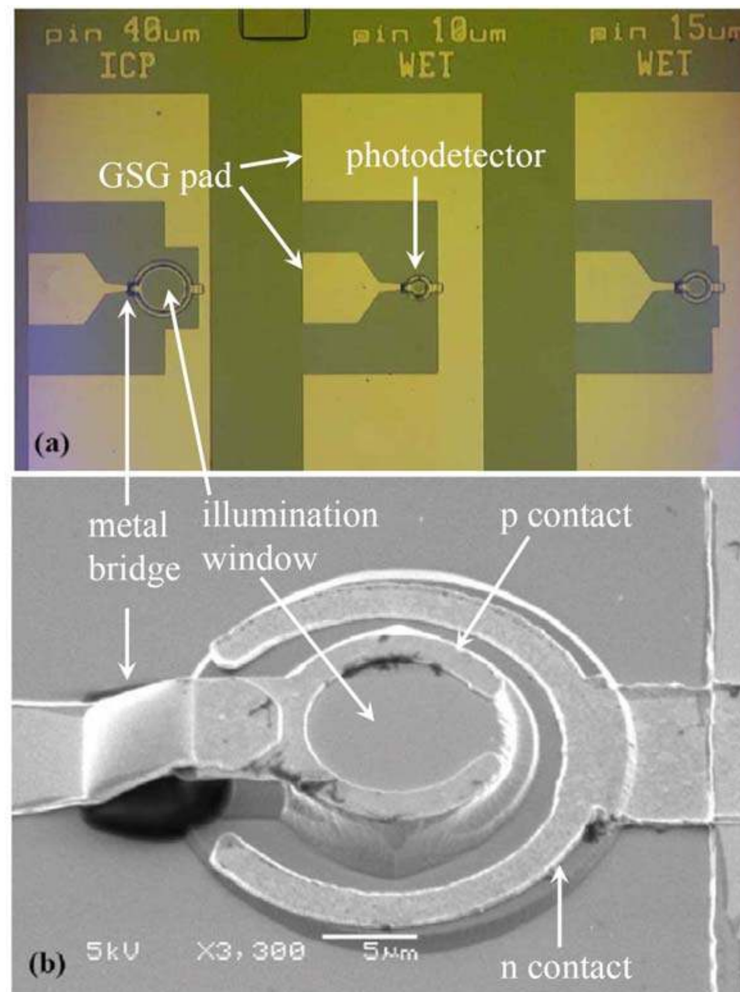

Figure 4.7 (a) Optical micrographs of three fabricated GaNAsSb-based p-i-n photodetector with optical illumination window diameters of 10µm, 15µm and 40µm. (b) Scanning electron micrographs of a GaNAsSb photodetector with air-bridge metallization. `

ATTENTION: The Singapore Copyright Act applies to the use of this document. Nanyang Technological University Library

4.2.3 Spectral response and dark current density

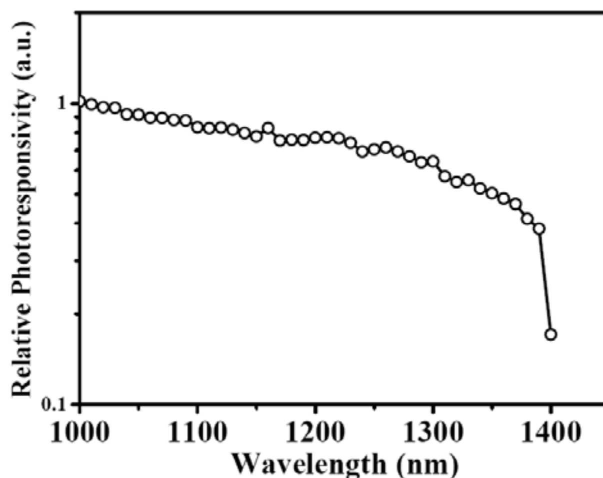

Figure 4.8 Relative spectral response of the GaNAsSb-based p-i-n photodetector.

The photoresponsivity measurement was carried out using a quartz tungsten halogen lamp, in conjunction with a monochromator. Furthermore, the light source was calibrated using a commercial InGaAs photodetector. The relative spectral response is shown in Figure 4.8 for a detector with a diameter of 80µm. It can be seen that the photoresponsivity starts to decrease beyond 1380nm, indicating the optical bandgap is smaller than 0.89eV. This agrees well with the prediction from the BAC model (~0.9eV) as mentioned earlier.

Figure 4.9 shows the dark current characteristic of the photodetector. At 0V and -5V, the dark current density is 1.6×10^{-5} A/cm^2 and 13 A/cm^2, respectively. These values are much higher compared to those from conventional InGaAs-based p-i-n

ATTENTION: The Singapore Copyright Act applies to the use of this document. Nanyang Technological University Library

photodetectors [78]. This could be due to the presence of nitrogen-related defects and arsenic antisite defects in the GaNAsSb layer, which is not uncommon in dilute nitride material [79]. The nitrogen-related defects could contribute to defect states at ~0.1eV above the valence band [26, 27, 79] and are likely to be caused by N-N pairs formed at the group V sites [70, 80]. The arsenic antisite defects contribute to defect states at the middle of the bandgap. Their formation is due to the low growth temperature (<500°C) of the GaNAsSb layer. Both defects increase the dark current density of the photodetector through the trap-assisted tunneling mechanism [27]. They provide the intermediate energy states for the carrier tunneling process. The magnitude of the carrier tunneling is dependent on the concentration of defects and the bandgap of the material. The smaller bandgap of GaNAsSb compared to GaAs leads to a more efficient carrier tunneling process.

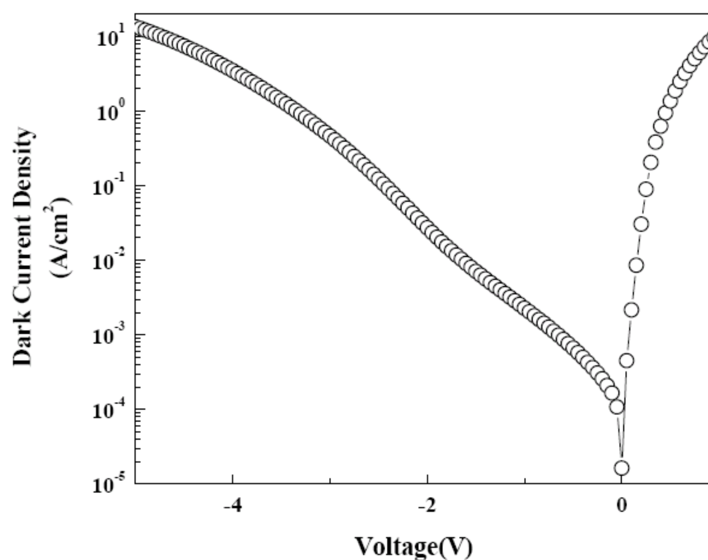

Figure 4.9 Plot of dark current characteristic of the GaNAsSb-based p-i-n photodetector.

ATTENTION: The Singapore Copyright Act applies to the use of this document. Nanyang Technological University Library

4.2.4 Temporal response and 3dB cutoff frequency

The temporal responses of the fabricated GaNAsSb-based p-i-n photodetectors were measured using a femtosecond laser system. A frequency-doubled Nd:YVO_4 laser (type: Coherent Verdi V-5) was used to pump a Ti:sapphire femtosecond Kerr-lens mode-locked laser (type: Coherent Mira 900B) generating 260fs pulses at 890nm wavelength with repetition rate of 76MHz. The wavelength of 890nm ensures negligible photocarrier generation in the adjacent doped GaAs layers, thus preventing significant diffusion current contributions. High-speed (40GHz) on-wafer microwave probes (GSG) and cables were used to extract the photogenerated pulses from the devices. The temporal response of the photodetectors was observed using a 70GHz sampling oscilloscope.

It can be seen in Figure 4.10(a), the 10%-90% rise time accounts for about 17.4ps and the shortest pulse widths (FWHM) achieved with a 10μm diameter device at -8V applied bias is 40.5ps. This corresponds to record bandwidth of about 4.5GHz which can also be seen from the normalized frequency response calculated by fast-Fourier transformation (inset in Figure 4.10(a)). From Figures 4.10(a) and 4.10(b), it can be observed that the rise time is almost independent of the device diameter as well as the applied reverse voltage, indicating a fast photocarrier generation process and electron drift in the photon-absorption layer. On the contrary, the relaxation time is strongly bias dependent. As can be seen from Figure 4.10(b), the relaxation time is significantly reduced by increasing the reverse bias to 8V. The bias-dependent relaxation can be clearly attributed to carrier transit time effects *i.e.* slow carrier transport in the n.i.d. absorption layer.

ATTENTION: The Singapore Copyright Act applies to the use of this document. Nanyang Technological University Library

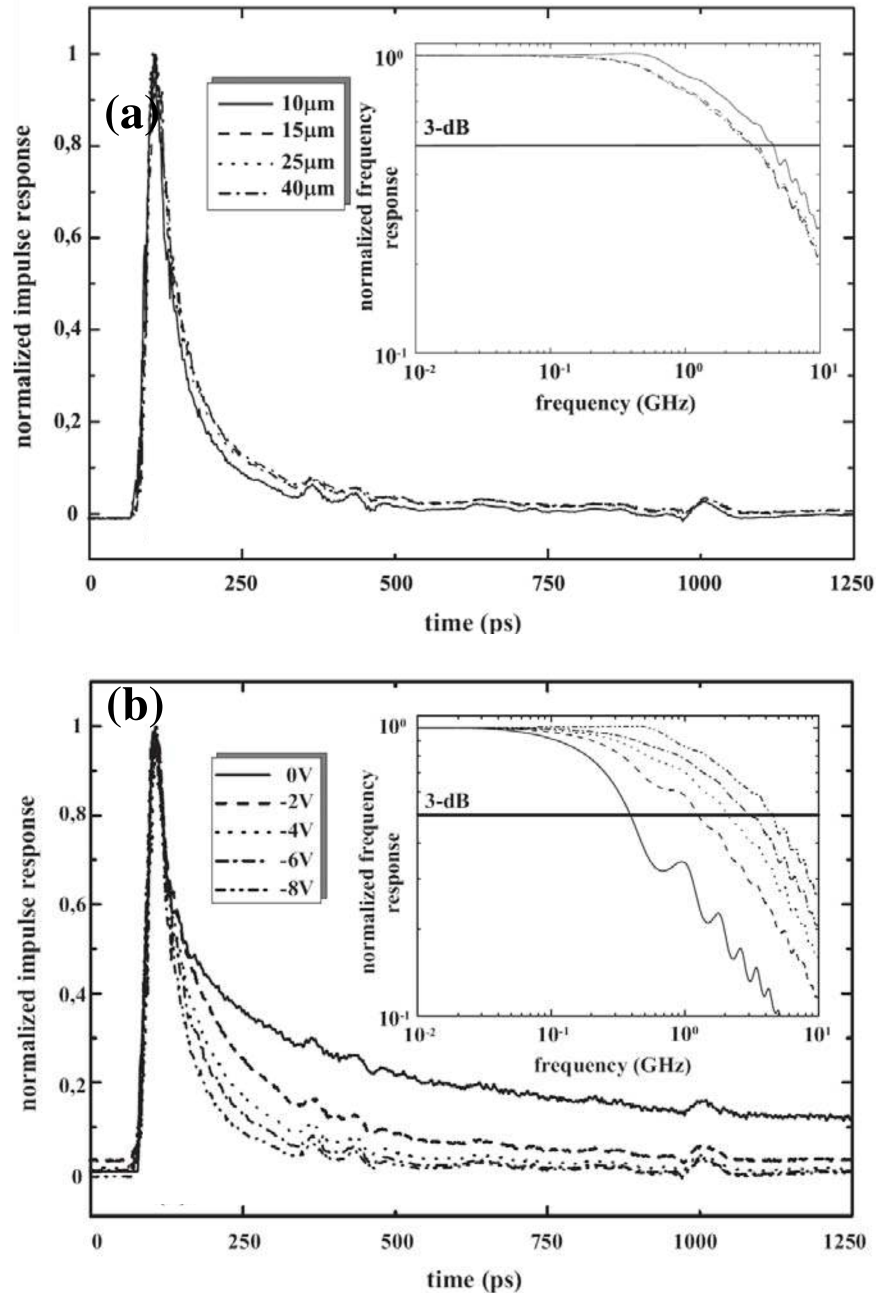

Figure 4.10 (a) Normalized temporal response of GaNAsSb-based p-i-n photodetectors of different diameters at -8V applied bias and (b) normalized temporal response of a 10μm diameter GaNAsSb photodetector at different reverse biases. Insets show the corresponding normalized frequency responses derived by fast-Fourier transform.

ATTENTION: The Singapore Copyright Act applies to the use of this document. Nanyang Technological University Library

According to drift-diffusion model simulation [81], the hole drift is the factor dominating the time constant here. The effective hole drift velocity is determined to be approximately 2×10^6cm/s, which is about 3-4 times slower than in GaAs. The low effective hole drift velocity can be explained by the fact that the GaNAsSb layer is not fully depleted. From capacitance-voltage measurement, the GaNAsSb photon-absorption layer has doping concentration of ~3×10^{17}cm^{-3}. Thus, even at applied reverse bias of 8V, the depletion width is only 0.24µm according to numerical simulations. Hence, even under high electric field, the holes only drifted for a short distance of ~0.24µm. Thereafter, the holes have to diffuse across the remaining 1.8µm of the GaNAsSb layer at a slower velocity. This effectively increases the overall transit time of the holes across the GaNAsSb layer.

On the other hand, the RC time constant does not significantly influence the device high-speed performance. The depletion layer thickness of 0.24µm results in RC delay limited cutoff frequency greater than 5GHz for all the devices. This is confirmed from Figure 4.10(a) which shows that the pulse widths are almost independent of the device diameter. Only slight speed improvement is observed in the smallest devices with 10µm diameter. Thus it can be concluded that the high-speed performance of the fabricated devices is mainly dominated by the carrier transit time.

ATTENTION: The Singapore Copyright Act applies to the use of this document. Nanyang Technological University Library

4.2.5 Summary

In summary, the GaNAsSb photodetectors with bandwidth of 4.5GHz have been successfully demonstrated. The devices exhibit photoresponsivity up to the wavelength of 1380nm. However, the existence of nitrogen-related defects has limited the width of the depletion region. This leads to smaller bandwidth compared to what is predicted using Eq. (2.17). Furthermore, these defects also induce a high leakage current in the photodetectors.

4.3 Fiber optic data transmission

4.3.1 Introduction

In this section, the frequency response of the GaNAsSb-based p-i-n photodetectors at 1.3μm was measured using a 1.3μm laser. The eye diagram and bit-error rate of the data transmission using the GaNAsSb-based p-i-n photodetectors is presented. Furthermore, 5Gb/s fiber-optic data transmission using this photodetector is demonstrated. Such high data rate transmission utilizing dilute nitride-based photodetectors is the first successful demonstration at the time when it was reported. This section also describes the effect of the high dark current in the photodetector on the eye diagram measurement.

ATTENTION: The Singapore Copyright Act applies to the use of this document. Nanyang Technological University Library

4.3.2 Frequency response measurement using 1.3μm laser

GaNAsSb-based p-i-n photodetectors with a bandwidth of 4.5GHz at 890nm wavelength were demonstrated in section 4.2.4. Frequency response measurements at wavelength of 1.3μm were measured using a continuous wave (CW) laser and an external Mach-Zehnder modulator. Figure 4.11 shows the schematic experimental setup for the frequency response measurement.

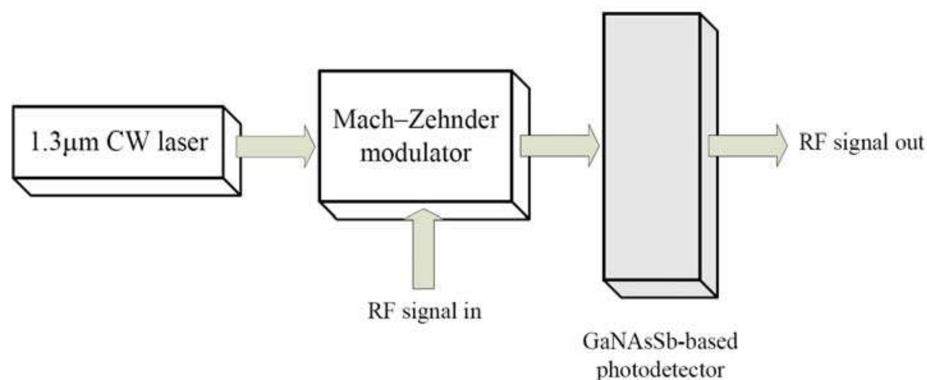

Figure 4.11 Schematic diagram of the experimental setup for the frequency response measurement.

The measurement is aimed to confirm that there is no deterioration in the bandwidth of these photodetectors at wavelength of 1.3μm. Light of different wavelength could lead to different distribution of carrier generation across the device. This might affect the speed of the photodetector. The frequency response of the GaNAsSb-based p-i-n photodetector with an illumination window diameter of 30μm was measured up to 12GHz. It can be seen in Figure 4.12 that the 3dB cutoff frequency is ~4.5GHz. This cutoff frequency is consistent with the results from temporal response measurement in section 4.2.4. This indicates that there is no deterioration in the bandwidth of the photodetectors at wavelength of 1.3μm.

ATTENTION: The Singapore Copyright Act applies to the use of this document. Nanyang Technological University Library

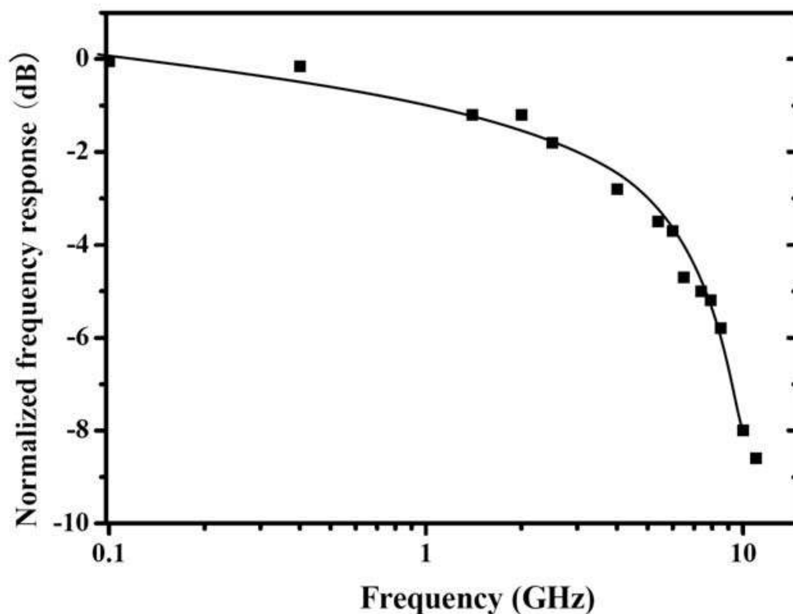

Figure 4.12 Frequency response characteristic of the GaNAsSb-based p-i-n photodetector at 1.3μm wavelength at reverse bias of 12V.

4.3.3 Eye diagram and bit-error rate at 5Gb/s

To carry out high data rate transmission experiments at 1.3μm wavelength, a 12.5 Gb/s pseudo-random bit sequence (PRBS, non-return-to-zero (NRZ), 2^{31}-1) source was used in conjunction with a direct frequency modulated 1.3μm laser. The RF output signal of the 30μm diameter photodetector was measured using a 50GHz sampling oscilloscope.

The eye diagram of the photodetector with the i-GaNAsSb layer grown at 440°C was firstly measured. From the measurement, it was found that the eye diagram is closed even at frequency as low as 300MHz. Figure 4.13 shows the closed eye

ATTENTION: The Singapore Copyright Act applies to the use of this document. Nanyang Technological University Library

diagram of the device at data rate of 300MHz. Since the device exhibits a 3dB cutoff frequency of 4.5GHz, the closed eye diagram cannot be due to the insufficient bandwidth in the device. Therefore, one possible reason for the measured closed eye diagram is the poor signal to noise ratio of the device. The high noise level in the device could be due to the high dark current shot noise. The power of the dark current shot noise is proportional to the square root of the dark current. The device shows a high dark current level of ~1.5mA at reverse bias of 8V. This could lead to the high noise level in the device. To overcome this problem, a GaNAsSb-based photodetector with a higher photoresponsivity and lower dark current is needed.

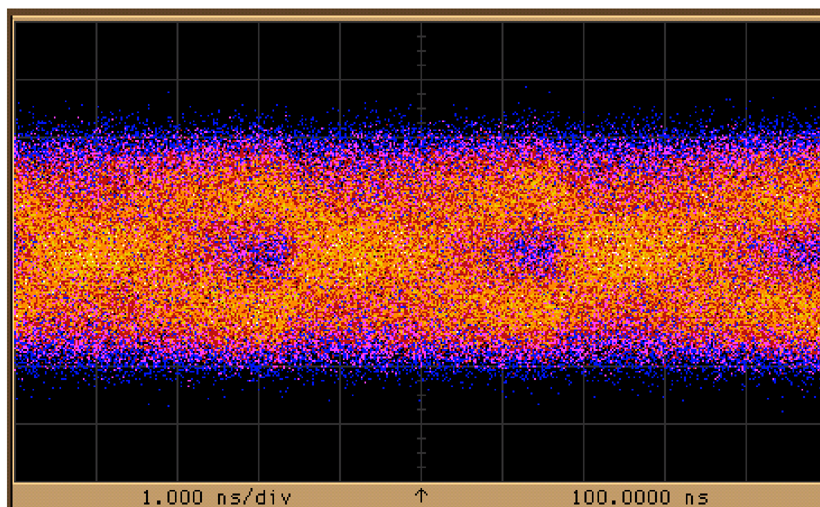

Figure 4.13 Closed eye diagram of GaNAsSb-based photodetector with i-GaNAsSb layer grown at 440°C at the data rate of 300MHz

The photoresponsivity of a GaNAsSb-based photodetector with the i-GaNAsSb layer grown at different temperatures was shown in Figure 4.2. Moreover, Figure 4.14 shows the dark current density of the GaNAsSb-based photodetector with the

ATTENTION: The Singapore Copyright Act applies to the use of this document. Nanyang Technological University Library

i-GaNAsSb layer grown at different temperatures. It can be noted that the device with the i-GaNAsSb layer grown at 400°C shows a higher photoresponsivity and lower dark current density, compared to the device with the i-GaNAsSb layer grown at 440°C. As a result, a new eye diagram measurement is carried out on the device with the i-GaNAsSb layer grown at 400°C.

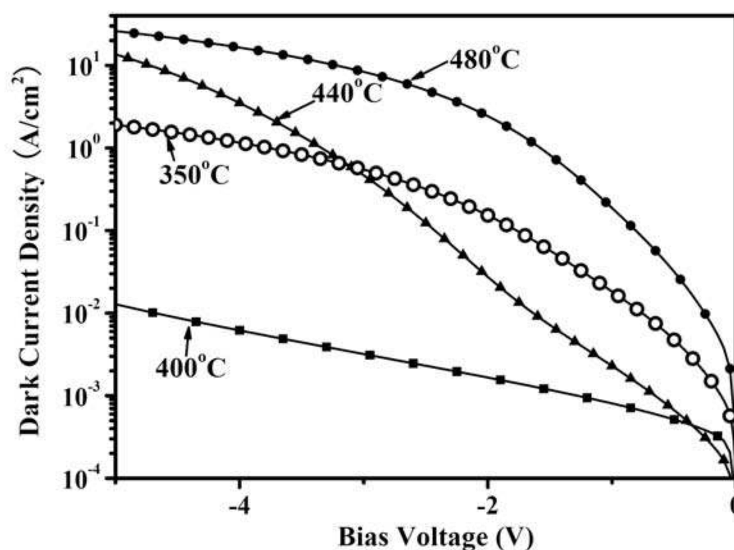

Figure 4.14 Plot of dark current density of the GaNAsSb-based photodetector with i-GaNAsSb layer grown at different temperatures *vs*. bias voltage.

The new eye diagram measurement shows an opened eye diagram up to a data rate of 5Gb/s. Figure 4.15 shows the measured eye diagram of the GaNAsSb-based p-i-n photodetector at a data rate of 5Gb/s. Higher photoresponsivity and lower dark current density in the GaNAsSb-based photodetector improve the device performance in the eye diagram measurement. This confirms the suitability of the GaNAsSb-based p-i-n photodetector for fiber-optic data transmission up to a data rate of 5Gb/s.

ATTENTION: The Singapore Copyright Act applies to the use of this document. Nanyang Technological University Library

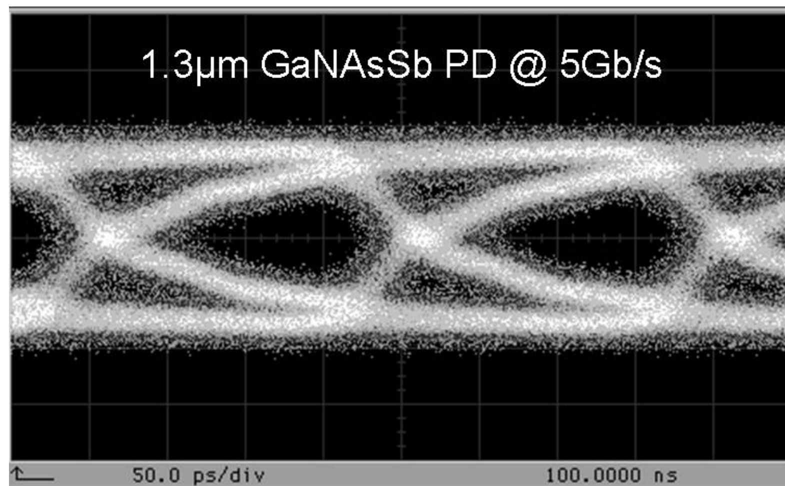

Figure 4.15 Eye diagram of the output signal from a 1.3µm GaNAsSb-based p-i-n photodetector with 30µm illumination window diameter at data rate of 5Gb/s.

Bit-error-rate (BER) measurements were performed using a 12.5Gb/s bit-error-rate tester (BERT). For comparison, there were two different photodetectors used in this measurement; a commercial 12GHz InGaAs-based photodetector with responsivity of 0.85A/W and the newly fabricated 30µm diameter GaNAsSb-based p-i-n photodetector with the i-GaNAsSb layer grown at 400°C. Figure 4.16 shows the measured BERs for the 30µm diameter GaNAsSb-based p-i-n photodetector at data rates of 2.5Gb/s and 5Gb/s, respectively. At 2.5Gb/s, the measured receiver sensitivity at BER of 10^{-9} for the GaNAsSb-based photodetector is 1.4dBm. The measured receiver sensitivity of the InGaAs-based photodetector at BER of 10^{-9} and data rate of 2.5Gb/s is 12.5dBm. The relatively higher responsivity of the InGaAs-based photodetector compared to GaNAsSb-based photodetectors contributes to the difference in receiver sensitivity between these two photodetectors.

ATTENTION: The Singapore Copyright Act applies to the use of this document. Nanyang Technological University Library

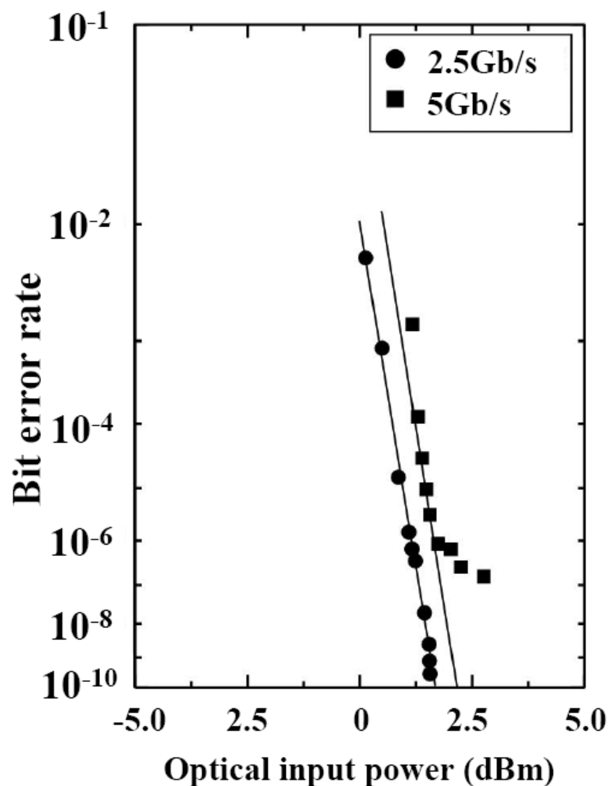

Figure 4.16 Dependence of the bit-error rate on the optical input power of the GaNAsSb-based p-i-n photodetector (30μm window diameter) at data rates of 2.5Gb/s and 5Gb/s, respectively. BER measurements were carried out at 1.3μm wavelength.

As shown in Figure 4.16, saturation of the BER at 10^{-7} at data rate of 5Gb/s for the GaNAsSb-based p-i-n photodetector was observed. This saturation is mainly due to the performance limitation of the broadband amplifier used in the BER measurements. The bandwidth and noise figure of this amplifier at the input of the BERT are 4.2GHz and 8dB, respectively. All measurements were performed at room temperature.

ATTENTION: The Singapore Copyright Act applies to the use of this document. Nanyang Technological University Library

GaNAsSb-based p-i-n photodetector is capable of performing fiber optic data transmission at a data rate up to 5Gb/s. Due to the bandwidth limitation, the GaNAsSb-based p-i-n photodetectors are unable to fulfil the requirement of 10GBASE-LR fiber optic system. The 10GBASE-LR fiber optic system requires a data transmission rate of 10Gb/s. Thus, the high frequency performance of the GaNAsSb-based photodetectors needs further improvement. Chapter five presents the application of GaNAsSb-based uni-traveling carrier photodetectors to improve the high frequency performance of the GaNAsSb-based photodetector.

4.3.4 Summary

In summary, the application of high-speed 1.3μm GaNAsSb-based p-i-n photodetectors in fiber-optic transmission links was successfully demonstrated at data rate of up to 5Gb/s. The GaNAsSb-based photodetector with the i-GaNAsSb layer grown at 400°C shows characteristics of higher responsivity and lower dark current density. These characteristics improve the performance of the photodetector in data transmission. This is the first successful demonstration of high data rate transmission at wavelength of 1.3μm using dilute nitride-based photodetectors.

ATTENTION: The Singapore Copyright Act applies to the use of this document. Nanyang Technological University Library

4.4 Extension of photo-response to 1.55µm

4.4.1 Introduction

In sections 4.1 to 4.3, the performance of the 1.3µm GaNAsSb-based photodetectors has been demonstrated. It is possible to design GaNAsSb-based devices for 1.55µm wavelength detection by further shrinking the bandgap of the GaNAsSb photon-absorption layer. To detect light at wavelength of 1.55µm, the bandgap of the GaNAsSb layer should be lower than 0.8eV. This bandgap value can be achieved by incorporating 4.3% of N and 11% Sb into the GaNAsSb material. However, in reality, it was found that the material quality and device performance is severely degraded when more than 4% of N is incorporated into the material. This is due to the formation of significant amount of nitrogen-related defects [27, 82]. An alternative approach is to use the strained GaNAsSb material system. In this approach, the nitrogen content in the GaNAsSb is kept at 3.5% while the Sb content is increased to 18%, leading to bandgap of 0.77eV in the GaNAsSb layer. However, the drawback of this approach is that the GaNAsSb layer is strained and thus, the quantum efficiency of the photodetector will be constrained by the critical layer thickness of the GaNAsSb layer.

This constraint can be overcome by using the waveguide photodetector (WGPD) structure. In contrast to the top illuminated photodetectors as shown in sections 4.1 to 4.3, where the quantum efficiency is dependent on the thickness of the

ATTENTION: The Singapore Copyright Act applies to the use of this document. Nanyang Technological University Library

GaNAsSb layer, the quantum efficiency of the WGPD is dependent on the cavity length of the waveguide. In this section, the spectral response and photoresponsivity of the GaNAsSb-based WGPD for 1.55μm detection is presented.

4.4.2 Growth and fabrication of GaNAsSb-based waveguide photodetector

The GaNAsSb-based WGPD structure grown by molecular beam epitaxy in conjunction with a RF N plasma source and a valved cracker source for antimony is shown in Figure 4.17. The 0.5μm-thick GaAs:Si (*n*-type) and 1.0μm-thick GaAs:C (*p*-type) layers, each with doping concentration of $5\times10^{18}cm^{-3}$ and $2\times10^{19}cm^{-3}$, respectively, were grown at 580°C. The n.i.d. GaNAsSb layer was grown at 400°C at RF plasma power of 320W and Sb beam equivalent pressure of 2.3×10^{-7} torr. The p-i-n WGPD device was fabricated with ridge widths of 6.5μm and 10μm and ridge length of 500μm.

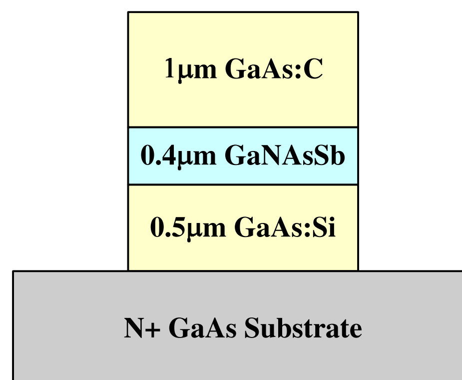

Figure 4.17 Schematic diagram of a GaNAsSb-based waveguide photodetector.

ATTENTION: The Singapore Copyright Act applies to the use of this document. Nanyang Technological University Library

4.4.3 X-ray diffraction characterization

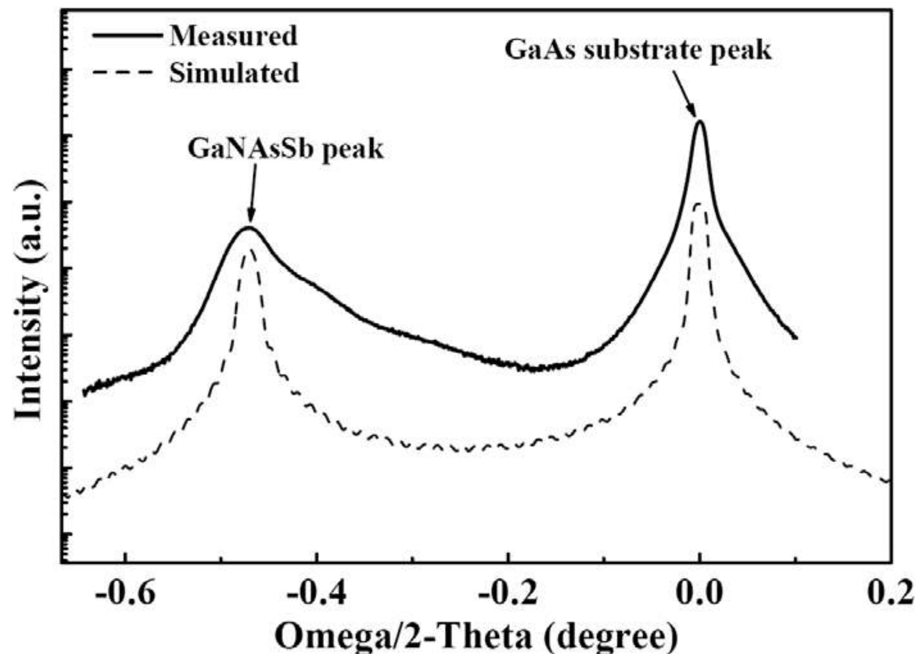

Figure 4.18 X-ray diffraction (004) rocking curve of GaNAsSb layer with 3.5% of N and 18% of Sb.

The composition of the GaNAsSb layer was characterized using XRD and is shown in Figure 4.18. From XRD measurement, the GaNAsSb layer contains 3.5 % of N and 18% of Sb. The thickness of the GaNAsSb layer was kept at 0.4µm to avoid strain relaxation. As indicated by the RHEED pattern during the growth, the growth of the GaNAsSb layer became three dimensional mode at thickness of 0.5µm. This three dimensional growth mode is due to the lattice mismatch between the GaAs substrate and GaNAsSb layer. Calculation using the BAC model [55] shows that the $GaN_{0.035}As_{0.785}Sb_{0.18}$ layer has energy bandgap of 0.77eV (or λ=1.61µm).

ATTENTION: The Singapore Copyright Act applies to the use of this document. Nanyang Technological University Library

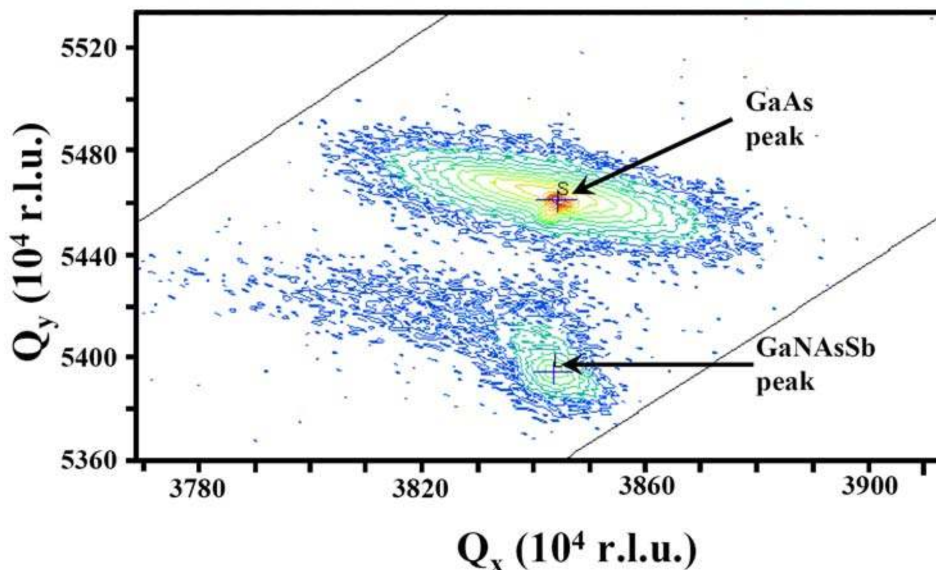

Figure 4.19 X-ray reciprocal (224) space map of GaNAsSb-based p-i-n waveguide photodetector. S and L denote the GaAs substrate peak and GaNAsSb layer peak, respectively.

To verify the degree of strain relaxation in the GaNAsSb layer, the (224) x-ray reciprocal space map of the sample was measured and is shown in Figure 4.19. The measurement comprises a series of ω-2θ scans. The result shows that the parallel (along the Q_x axis) d-spacing difference between the substrate and layer peaks in reciprocal lattice unit (rlu) (Q_x direction) is 0.062×10^{-3} and the perpendicular (along the Q_y axis) d-spacing difference (Q_y direction) is 6.651×10^{-3}, indicating strain relaxation of 1% in the GaNAsSb layer.

4.4.4 Dark current density

Figure 4.20 shows the current-voltage characteristics of the WGPD with 6.5µm ridge width and 500µm ridge length. At reverse bias voltage of -1.5V, the dark

ATTENTION: The Singapore Copyright Act applies to the use of this document. Nanyang Technological University Library

current density of the WGPD is 22.2 A/cm^2. This is higher compared to the dark current density of the top-illuminated GaNAsSb p-i-n device as shown in Figure 4.9. This high dark current density could be due to the strain relaxation of 1% as previously discussed in section 4.4.3. Strain relaxation gives rise to threading dislocation, leading to higher device leakage current.

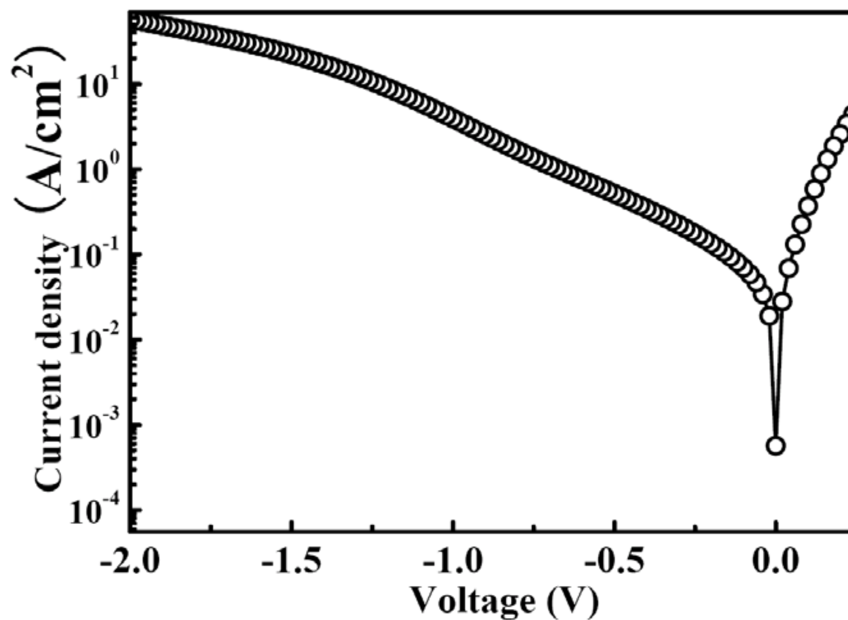

Figure 4.20 Current-voltage characteristics of a GaNAsSb-based p-i-n waveguide photodetector with 6.5μm ridge width and 500μm ridge length.

4.4.5 Spectral response and photoresponsivity at 1.55μm

Figure 4.21 shows the spectral response of the WGPD with 6.5μm ridge width and 500μm ridge length. The measurement was carried out using a 100W quartz tungsten halogen lamp and monochromator in conjunction with a lock-in amplifier to obtain the photo-response spectrum from 1000-1600nm.

ATTENTION: The Singapore Copyright Act applies to the use of this document. Nanyang Technological University Library

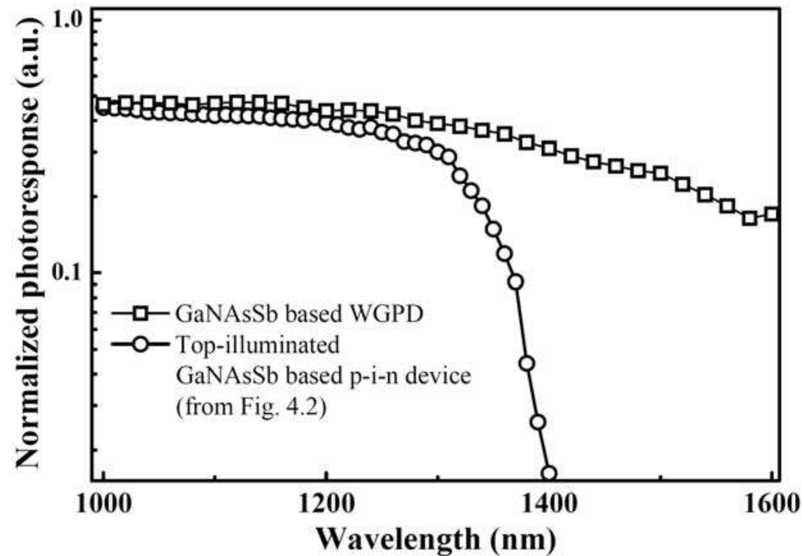

Figure 4.21 Normalized spectral response of GaNAsSb-based p-i-n waveguide photodetector with 6.5μm ridge width and 500μm ridge length. The data of top-illuminated photodetector is taken from Figure 4.2.

The result shows that the GaNAsSb-based WGPD exhibits photo-response up to at least 1600nm. It has longer cutoff wavelength compared to that of the top-illuminated GaNAsSb-based p-i-n devices as shown in Figure 4.2. The cutoff wavelength of the device is consistent with the shrinkage of bandgap of the GaNAsSb layer to 0.77eV as mentioned earlier.

To measure the photoresponsivity, a 1.55μm laser source is coupled into the waveguide facet of the WGPD using a cleaved single mode fiber (10μm core diameter) without additional optical components. The photoresponsivity measurements of all the WGPDs are conducted at reverse bias voltage of 1.5V under incident laser power of 100μW at 1.55μm.

ATTENTION: The Singapore Copyright Act applies to the use of this document. Nanyang Technological University Library

The photoresponsivity of the WGPD with ridge width of 6.5μm is 0.25A/W, while the photoresponsivity of the WGPD with ridge width of 10μm is 0.29A/W. This is because the larger ridge width reduces the coupling loss between the single mode fiber and waveguide facet. The mismatch between the size of the single mode fiber (10μm in diameter) and thickness of the GaNAsSb photon-absorption layer (0.4μm) leads to significant coupling loss in the photoresponsivity measurement. Taking the effect of coupling loss into account, the real photoresponsivity of the GaNAsSb-based WGPD should be higher than 0.29A/W.

These photoresponsivity values are much higher than the reported values of photoresponsivity from top-illuminated photodetectors which use GaNAsSb/GaAs double quantum well structure as the photon-absorption layer. Those photodetectors have a responsivity value of 0.01-0.016A/W at 1.55μm [15]. Furthermore, the photoresponsivity values from the GaNAsSb-based WGPD devices are also comparable to the photoresponsivity values of reported [14] GaInNAs-based RCE photodetectors (0.4A/W). The RCE photodetector uses a mirror system to trap the incident light and thus enhances the photoresponsivity. However, unlike the WGPD, the RCE photodetector structure is not suitable for high-speed applications due to the trapping of light inside the cavity.

ATTENTION: The Singapore Copyright Act applies to the use of this document. Nanyang Technological University Library

4.4.6 Summary

In summary, GaNAsSb-based p-i-n WGPD devices with measured photoresponsivity of up to 0.29A/W at wavelength of 1.55μm have been successfully demonstrated. The devices have shown photo-response of at least 1.6μm. These WGPD devices use 0.4μm-thick strained GaNAsSb layer as the photon-absorption layer. Photoresponsivity of 0.29A/W has been achieved without any mirror system, unlike in RCE-based devices.

ATTENTION: The Singapore Copyright Act applies to the use of this document. Nanyang Technological University Library

Chapter 5 GaNAsSb-based uni-traveling carrier photodetector

5.1 Introduction

In chapter 4, the GaNAsSb-based p-i-n photodetectors [43, 46, 83] have shown a transit time limited 3dB cutoff frequency (f_T) value of 4.5GHz. The cutoff frequency of the GaNAsSb-based p-i-n photodetector is mainly limited by the slow velocity of hole carriers in the undepleted region [43], leading to a long tail signature in the temporal response signal for a narrow pulse input. Data transmission over fiber optic at data rate of 5Gb/s has been demonstrated using the GaNAsSb-based p-i-n photodetectors.

3dB cutoff frequency of 4.5GHz and data transmission rate of 5Gb/s are incapable of meeting the requirements of the 10GBASE-LR fiber optic system. Thus, further improvement in the bandwidth of the GaNAsSb-based photodetectors is needed. In this chapter, the GaNAsSb-based uni-traveling carrier photodetector is proposed and demonstrated to improve the bandwidth of the GaNAsSb-based photodetectors. UTC photodetectors utilize only electron carriers which have much shorter transit time compared to hole carriers. The UTC photodetectors overcome the problem of slow hole carriers faced by the GaNAsSb-based p-i-n photodetectors. In this chapter, temporal response, frequency response and data transmission of the GaNAsSb-based UTC photodetector are presented.

ATTENTION: The Singapore Copyright Act applies to the use of this document. Nanyang Technological University Library

5.2 Growth and fabrication of GaNAsSb-based UTC photodetectors

The structure, shown in Figure 5.1(a), was grown using MBE in conjunction with a RF N plasma source and a valved cracker Sb source. The n.i.d. photon-absorption layer comprises a 0.1μm-thick GaNAsSb (bulk) layer with p-type doping concentration of ~1×10^{17}cm^{-3}. This layer contains ~3.5% of N and 9% of Sb and has bandgap of ~0.88eV, making the UTC photodetectors suitable for near infrared detection up to wavelengths of about 1380nm [43].

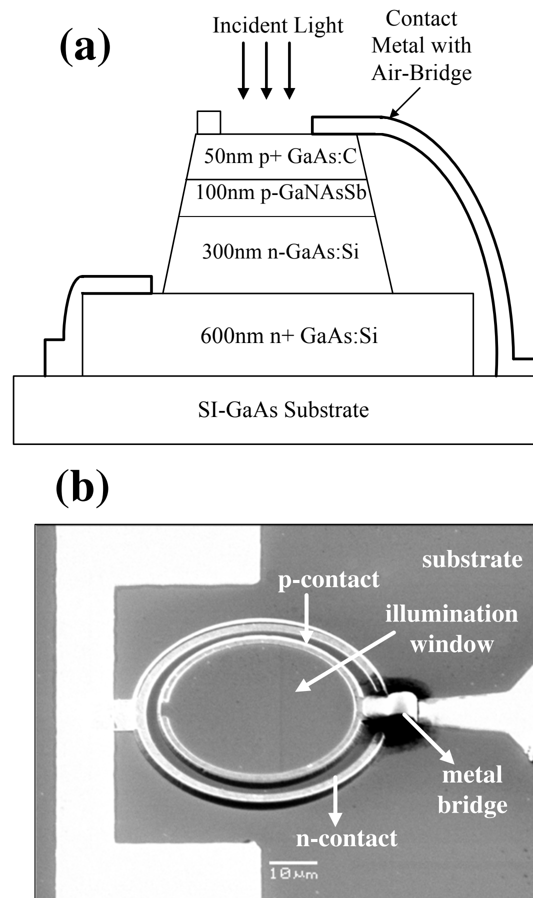

Figure 5.1 (a) Cross section schematic of a GaNAsSb-based UTC photodetector structure. (b) SEM photograph of a GaNAsSb-based UTC photodetector with an illumination window diameter of 25μm.

ATTENTION: The Singapore Copyright Act applies to the use of this document. Nanyang Technological University Library

The p^+ and n^+ layers of the device comprise C-doped and Si-doped GaAs, respectively. The 50nm-thick GaAs:C layer also acts as a diffusion blocker to reflect back the electrons into the n^- GaAs collector layer. The doping concentrations of the p^+ GaAs contact layer, the n^+ GaAs contact layer and the n^- GaAs collector layer are approximately $2x10^{19}cm^{-3}$, $5x10^{18}cm^{-3}$ and $5x10^{16}cm^{-3}$, respectively.

GaNAsSb-based UTC photodetectors with different illumination window diameters were fabricated using a high-speed microwave design with coplanar feed-lines. Ohmic p and n contacts were formed by 320nm-thick Ti/Pt/Au and 400nm-thick annealed Ni/Ge/Au metallization, respectively. The photodetectors were mounted in a 50Ω ground-signal-ground RF carrier using air bridge metallization technology. Figure 5.1(b) shows a scanning electron microscope (SEM) photograph of the fabricated GaNAsSb-based UTC photodetector.

Figure 5.2 shows the schematic diagram of the bandgap structure of a GaNAsSb-based UTC device. The p^+ GaAs layer reflects back the electrons to the collector layer through the conduction band offset. Electrons diffusing towards the n^- GaAs collector layer are swept into the n^+ GaAs contact layer by the electric field.

ATTENTION: The Singapore Copyright Act applies to the use of this document. Nanyang Technological University Library

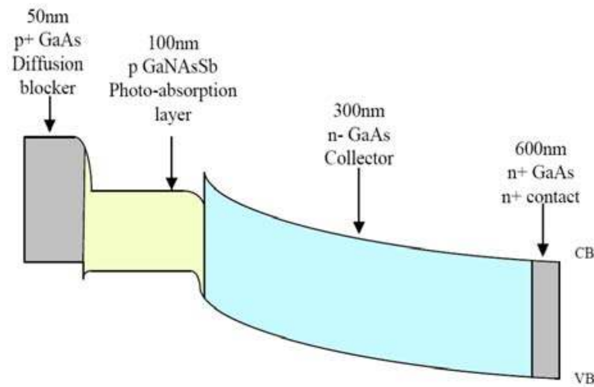

Figure 5.2 Schematic band diagram of a GaNAsSb-based UTC photodetector.

5.3 Dark current density

Figure 5.3 shows the dark current characteristic of the GaNAsSb-based UTC photodetector. At 0V and -9V bias voltage, the dark current density is 6mA/cm^2 and 34mA/cm^2, respectively. These values are at least 2 orders lower compared to those of previously reported GaNAsSb-based p-i-n photodetectors in Figure 4.9 [43], which is mainly attributed to the thinner GaNAsSb layer (100nm *vs.* 2µm) used in the GaNAsSb-based UTC photodetectors.

However, these dark current density values are relatively high compared to those of conventional InGaAs-based p-i-n photodetectors [78]. This may be due to the presence of nitrogen-related defects in the GaNAsSb layer, which is not uncommon in dilute nitride materials [27] and arsenic antisite defects [30]. The growth temperature of the GaNAsSb layer is normally <500°C. This growth temperature is below the normal growth temperature of GaAs material (~600°C).

ATTENTION: The Singapore Copyright Act applies to the use of this document. Nanyang Technological University Library

Thus, the low growth temperature of GaNAsSb layer results in the formation of As antisite defects in the material. From reported results [27], other dilute nitride-based photodetectors also show similar characteristic of high dark current density. The high dark current density in the dilute nitride-based photodetectors is due to trap-assisted tunneling mechanism associated with nitrogen-related defects and As antisite defects.

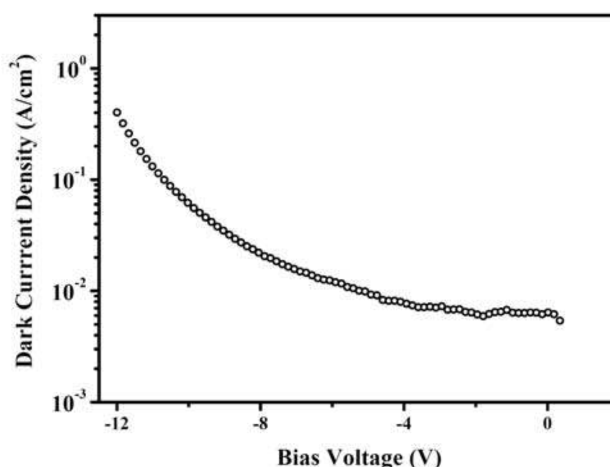

Figure 5.3 Dark current characteristic of the GaNAsSb-based UTC photodetector.

From the trap-assisted tunneling model [27], the magnitude of the dark current is proportional to the depletion region width of the dilute nitride material. The thickness and depletion region width of the GaNAsSb layer in the UTC device is thinner compared to those of previous p-i-n devices discussed in chapter four. This leads to smaller dark current density in the GaNAsSb-based UTC photodetector compared to the dark current density in the GaNAsSb-based p-i-n photodetectors which are shown in Figure 4.9.

ATTENTION: The Singapore Copyright Act applies to the use of this document. Nanyang Technological University Library

5.4 Temporal response and 3dB cutoff frequency

The temporal response of the fabricated GaNAsSb-based UTC photodetectors was measured using a femtosecond laser system. A frequency-doubled Nd:YVO_4 laser was used to pump a Ti:sapphire femtosecond Kerr-lens mode-locked laser, generating 260fs pulses at 890nm wavelength with a repetition rate of 76MHz. An excitation wavelength value of 890nm was chosen to ensure negligible photocarrier generation in the adjacent doped GaAs layers, thus preventing significant diffusion current contributions.

The photoresponsivity of the GaNAsSb-based UTC photodetector was measured using a 1.3μm laser. The incident laser was coupled into the illumination window of the photodetector using a cleaved single mode fiber. At reverse bias of 12V, the photoresponsivity value was measured to be 0.35A/W. The temporal response of the photodetectors was observed using a 50GHz sampling oscilloscope. Using a 1.3μm directly modulated laser diode, the frequency response of the photodetector was measured at frequencies up to 15GHz using an electrical spectrum analyzer.

Figure 5.4 shows the temporal response results of the UTC photodetectors with different illumination window diameters measured at -9V. The shortest pulse is achieved from the 10μm diameter device. The FWHM of the pulse is 46ps. The 10% to 90% rise time of the device is ~23ps.

ATTENTION: The Singapore Copyright Act applies to the use of this document. Nanyang Technological University Library

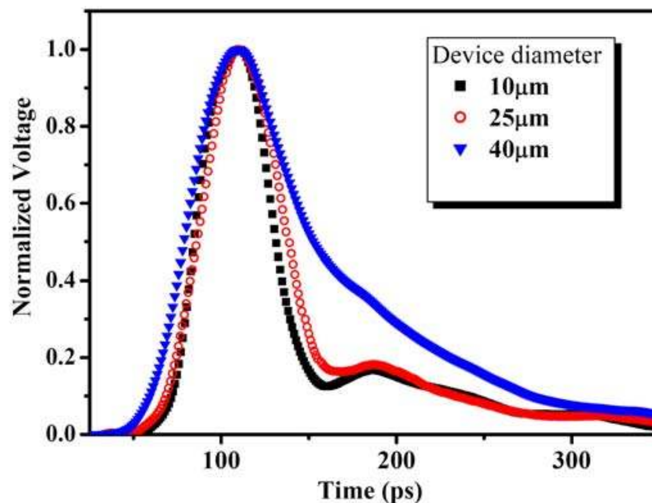

Figure 5.4 Normalized temporal response of GaNAsSb-based UTC photodetectors of different diameters at 9V reverse bias.

Figure 5.5 shows the temporal response of the 10μm diameter GaNAsSb-based p-i-n photodetector and the 10μm GaNAsSb-based UTC photodetector. It can be seen that the response of the UTC photodetector does not exhibit characteristic of significant long tail decay in the output signal compared to the temporal response of a 10μm diameter GaNAsSb p-i-n photodetector [43]. The rise time and fall time in the temporal response of the UTC photodetector is almost identical. This result confirms that the implementation of the UTC photodetector structure successfully minimizes the effect of slow hole carrier velocity in the device.

Figure 5.6 shows the frequency response of the devices at 1.3μm illumination. The highest 3dB cutoff frequency of ~14GHz is achieved from the 10μm diameter device at a reverse bias voltage of 9V. This value of f_T is the highest ever reported from GaAs-based dilute nitride photodetector at 1.3μm illumination.

ATTENTION: The Singapore Copyright Act applies to the use of this document. Nanyang Technological University Library

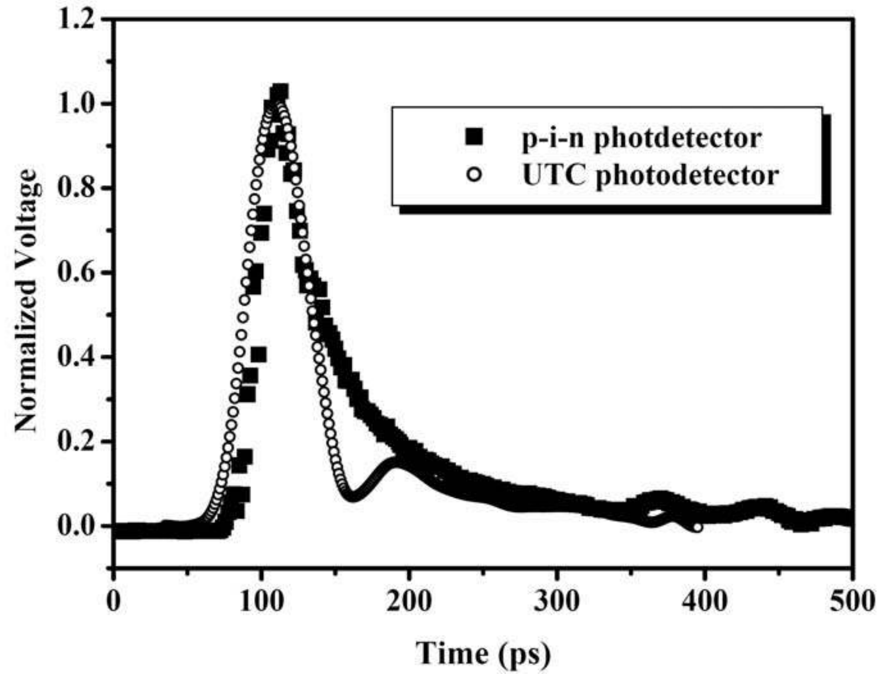

Figure 5.5 Temporal response of the 10μm diameter GaNAsSb-based p-i-n photodetector and the 10μm GaNAsSb-based UTC photodetector.

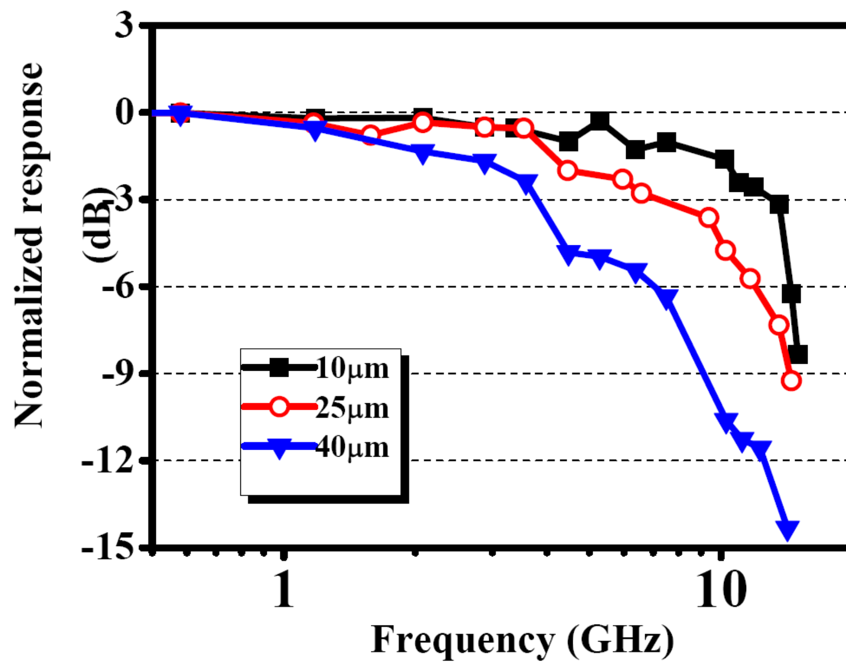

Figure 5.6 Frequency response characterization of the GaNAsSb-based UTC photodetector measured using a 1.3μm laser.

ATTENTION: The Singapore Copyright Act applies to the use of this document. Nanyang Technological University Library

By decreasing the illumination window diameter from 40μm to 25μm, the FWHM of the pulsed signal decreases from 75ps to 50ps. Further decrease in the device diameter from 25μm to 10μm only results in a marginal decrease (from 50ps to 46ps) in the FWHM of the pulsed signal. The decrease in the FWHM of the pulsed signal in the smaller devices is primarily due to the smaller junction capacitance in the smaller devices. The junction capacitance of the device with diameters of 10μm, 25μm and 40μm are 0.05pF, 0.3pF and 0.8pF, respectively. These junction capacitance values are calculated from the doping profile of the devices.

The RC delay limited 3dB cutoff frequency of the devices can be calculated using Eq. (2.15). The RC delay limited 3dB cutoff frequency of the devices with diameter of 10μm, 25μm and 40μm are 75GHz, 10GHz and 4GHz, respectively. Compared to the measured 3dB cutoff frequency shown in Figure 5.6, it can be concluded that the 3dB cutoff frequency of the device with diameter of 40μm is limited by the RC delay. However, the 3dB cutoff frequency of the photodetectors becomes transit time limited for the devices with diameter of 10μm. The measured 3dB cutoff frequency of the photodetectors with diameter of 10μm is 14GHz. This measured 3dB cutoff frequency is much lower than the RC delay limited 3dB cutoff frequency of 75GHz.

More evidence of the RC delay limitation of the 40μm diameter device can be

ATTENTION: The Singapore Copyright Act applies to the use of this document. Nanyang Technological University Library

deduced from the results in Figure 5.7 which show the temporal response of the UTC photodetectors with a diameter of (a) 10µm, (b) 25µm and (c) 40µm at different reverse bias voltages. Figures 5.7(a) and 5.7(b) show the pulsed FWHM of the temporal response of the 10µm and 25µm diameter devices does not change significantly at different reverse bias voltages. However, Figure 5.7(c) shows the pulsed FWHM of the temporal response of the 40µm diameter device decreases from 104ps to 75ps following increase in the reverse bias voltage from 3V to 9V.

Increase in the reverse bias voltage widens the depletion region. This reduces the junction capacitance and shortens the RC delay in the device. The reduction in RC delay is important for devices with RC delay limited cutoff frequency such as the 40µm diameter UTC photodetector in this experiment. At higher reverse bias voltage, the pulsed FWHM of the temporal response of the 40µm diameter device decreases because of the reduction in the RC delay.

On the other hand, a reduction in the junction capacitance following the increase in the reverse bias voltage in the 10µm and 25µm diameter devices does not significantly change the pulsed FWHM of the temporal response as shown in Figures 5.7(a) and 5.7(b). This indicates that the 3dB cutoff frequency of these devices is transit time limited. A reduction in RC delay following the increase in reverse bias voltage does not change the 3dB cutoff frequency of these devices which have transit time limited cutoff frequency.

ATTENTION: The Singapore Copyright Act applies to the use of this document. Nanyang Technological University Library

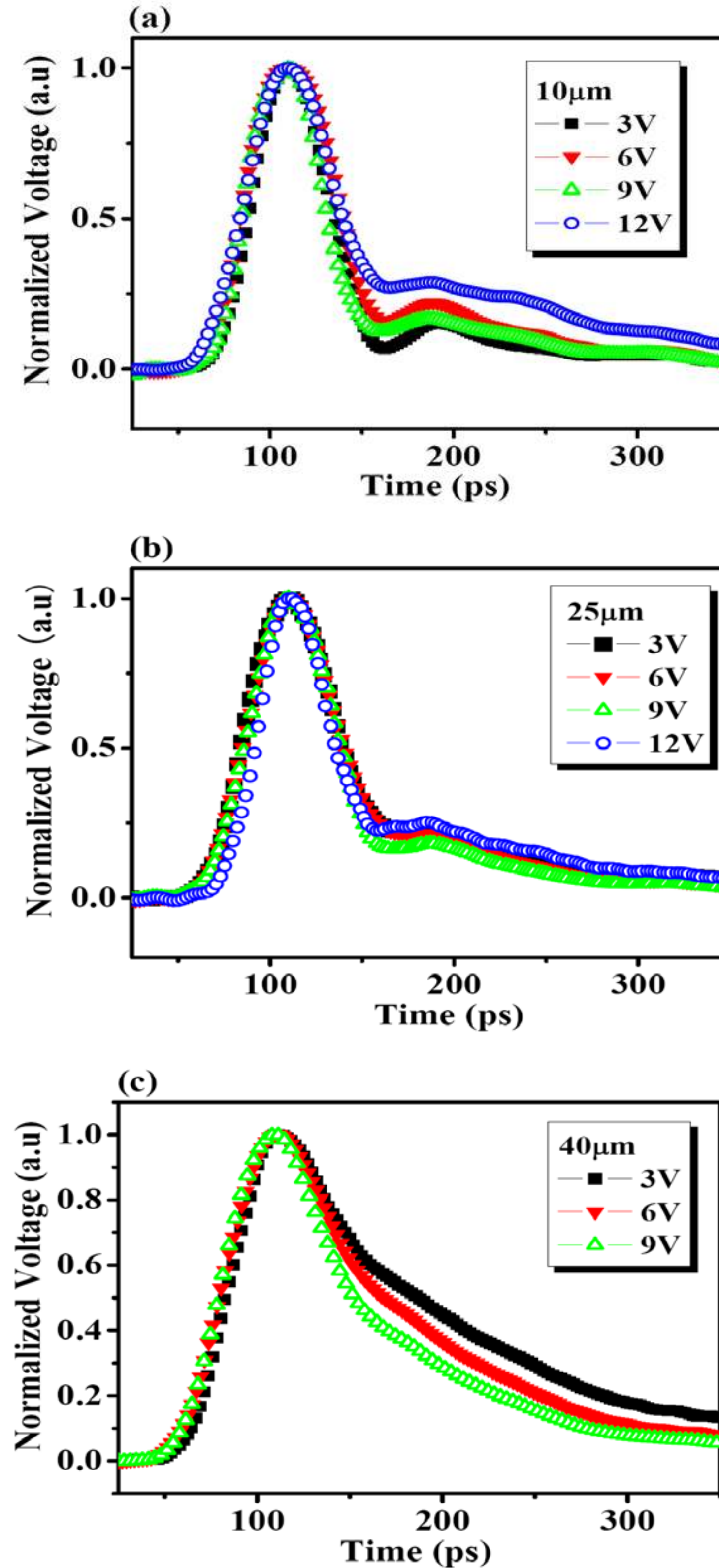

Figure 5.7 Normalized temporal response at different reverse biases for GaNAsSb-based UTC photodetectors with (a) 10µm, (b) 25µm and (c) 40µm illumination window diameters.

ATTENTION: The Singapore Copyright Act applies to the use of this document. Nanyang Technological University Library

5.5 Bandwidth limiting factor of GaNAsSb-based UTC photodetectors

In the GaNAsSb-based UTC photodetectors, electrons follow two transport mechanisms, namely diffusion and drift. The photogenerated electrons will first diffuse across the GaNAsSb layer and then drift across the n GaAs collector layer in response to the electric field. The electron saturated drift velocity of GaAs is 1×10^{7}cm/s. Thus, the drift of electrons across the 300nm n GaAs layer will take ~ 3ps. It is not responsible for the ~46ps pulsed FWHM observed in the 10μm diameter devices as shown in Figure 5.4. The 46ps pulse width observed in this device can only be attributed to the diffusion of electrons across the GaNAsSb layer. The pulsed FWHM of the temporal response of GaAs-based UTC photodetectors with similar absorption layer thickness is typically <2ps [84]. Hence, the pulse width of 46ps could indicate slow electron diffusion and low electron mobility in the GaNAsSb material, compared to GaAs.

The low electron mobility in dilute nitride material system has been reported before [85]. There are two reasons for the low electron mobility in dilute nitride materials: (1) incorporation of nitrogen into GaAs and (2) presence of defects in the dilute nitride material. The incorporation of nitrogen into GaAs increases the scattering cross section of the free electrons. From the calculation in reference [85], incorporating more than 0.5% of nitrogen into GaAs reduces the electron mobility

ATTENTION: The Singapore Copyright Act applies to the use of this document. Nanyang Technological University Library

in the material by at least one order. Secondly, the presence of defects such as nitrogen-related defects and As antisite defects in the dilute nitride material also reduces the electron mobility.

There is no report on the electron diffusion coefficient in the GaNAsSb material. Thus, it is very difficult to estimate the electron diffusion time in the device. However, the mobility of GaInNAs with 3% of N has been reported to be 90cm^{2}V^{-1}s^{-1} [86]. GaNAsSb layer in this UTC structure contains 3.5% of nitrogen. Electron mobility of dilute nitride material decreases with increase in nitrogen content. Thus, the electron mobility of GaNAsSb layer in the UTC device is safely expected to be <90 cm^{2}V^{-1}s^{-1}. Using Einstein relation, the diffusion coefficient of GaNAsSb material is <2.3cm^2/s. This gives an electron diffusion time of >22ps in the device. This estimated value of electron diffusion time is consistent with the 46ps pulse width observed in the GaNAsSb-based UTC device.

GaNAsSb-based p-i-n photodetectors suffer from the characteristic of long tail decay in the signal of the temporal response measurement. This is due to the problem of slow hole carriers in the undepleted region of the i-GaNAsSb layer as discussed in section 4.2. The i-GaNAsSb layer in the GaNAsSb-based p-i-n photodetectors is unable to be fully depleted due to the high unintentional doping concentration in the GaNAsSb material.

ATTENTION: The Singapore Copyright Act applies to the use of this document. Nanyang Technological University Library

In the UTC photodetector, the response time of hole carriers is very short, *i.e* <1ps. Thus, the transit time of hole carriers does not limit the bandwidth of the GaNAsSb-based UTC photodetectors. The bandwidth of the GaNAsSb-based UTC photodetector has improved compared to that of the GaNAsSb-based p-i-n photodetector because of the thinner GaNAsSb layer and the higher mobility of electrons (compared to holes). However, due to the low electron mobility in the dilute nitride material (compared to that of GaAs), the bandwidth of GaNAsSb-based UTC photodetectors is lower compared to that of GaAs-based UTC photodetector. The GaAs-based UTC photodetectors has 3dB cutoff frequency of >100GHz.

5.6 Eye diagram and bit-error rate

To carry out the high data rate transmission experiments at 1.3µm wavelength, a 12.5Gb/s pseudo-random bit sequence (PRBS, non-return-to-zero (NRZ), 2^{31}-1) source was used in conjunction with a direct frequency modulated 1.3µm laser and a 10km long standard optical single mode fiber (SMF). The RF output signal of the GaNAsSb-based UTC photodetector was measured using a 50GHz sampling oscilloscope. To evaluate the performance of the GaNAsSb-based UTC photodetector in fiber optic communication systems, the photodetector performance was characterized according to the IEEE802.3ae specifications for the 10GBASE-LR system.

ATTENTION: The Singapore Copyright Act applies to the use of this document. Nanyang Technological University Library

To fulfil the IEEE802.3ae specifications for the 10GBASE-LR system, data rates of 10.3125Gb/s is needed. In this work, the measurements were performed at data rate of up to 12.5Gb/s, which is the highest data rate generated by the signal generator used in the measurements. The 25µm diameter device was used in the high data rate transmission experiment. Although the 10µm diameter device has higher 3dB cutoff frequency compared to the 25µm diameter device, its smaller device size leads to higher coupling loss between the output of the fiber and the device. Higher coupling loss of the laser power in the 10µm diameter device degrades the device performance in the high data rate transmission measurement.

The measured eye diagrams of the data transmission over the 10km SMF at data rates of 7.5Gb/s, 10.3125Gb/s and 12.5Gb/s using the GaNAsSb-based UTC photodetector are shown in Figure 5.8. It can be seen that all the measured eye diagrams are clearly opened. This verifies that the GaNAsSb photodetectors are well suited for the 10Gb/s Ethernet fiber optic transmission.

To quantitatively evaluate the capability of the GaNAsSb-based UTC photodetector in data transmission over a 10km SMF, bit-error-rate measurements at data rates of 10.3125Gb/s and 12.5Gb/s were carried out. A broadband amplifier with noise figure of ~6dB, was employed to amplify the output signal of the photodetectors. The measurements were performed at room temperature.

ATTENTION: The Singapore Copyright Act applies to the use of this document. Nanyang Technological University Library

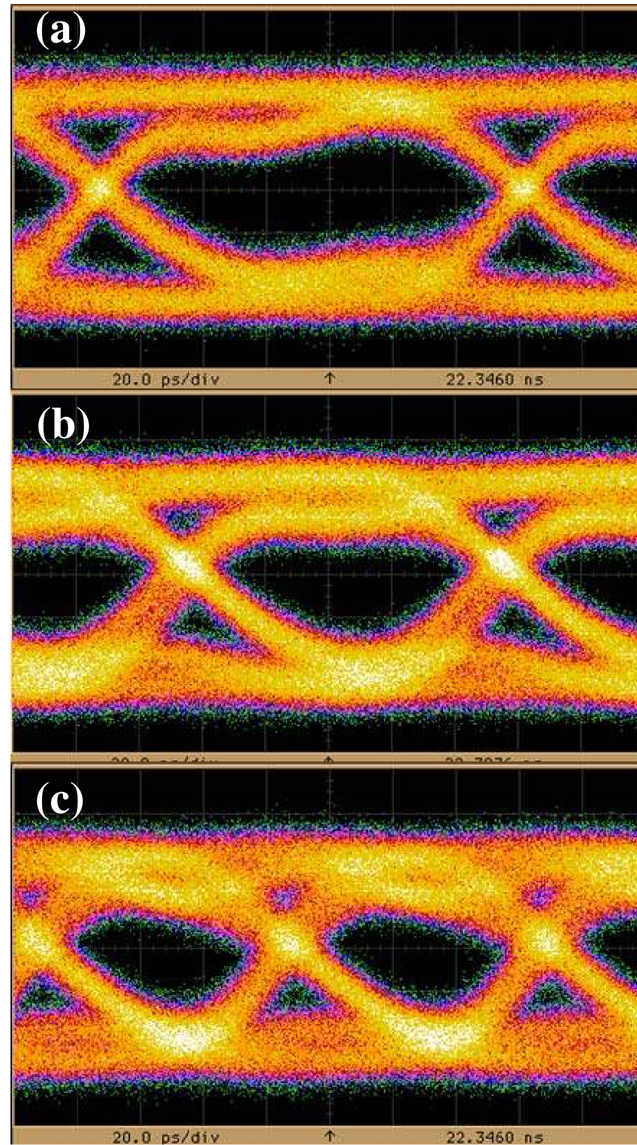

Figure 5.8 Eye diagrams of the output signal from a 1.3µm GaNAsSb-based UTC photodetector with 25µm illumination window diameter at data rate of (a) 7.5Gb/s (b) 10.3125Gb/s and (c) 12.5Gb/s for data transmission over a 10km single mode fiber.

The measured bit-error-rate of the 25µm GaNAsSb-based UTC photodetector at data rates of 10.3125Gb/s and 12.5Gb/s are shown in Figure 5.9. At 10.3125Gb/s, the receiver sensitivity at a BER value of 4×10^{-12} is -0.38dBm. The measured receiver sensitivity at a BER value of 9.3×10^{-12} at data rate of 12.5Gb/s is

ATTENTION: The Singapore Copyright Act applies to the use of this document. Nanyang Technological University Library

0.28dBm. These BER results confirm the capability of the GaNAsSb-based photodetectors in the 10Gb/s Ethernet fiber optic transmission.

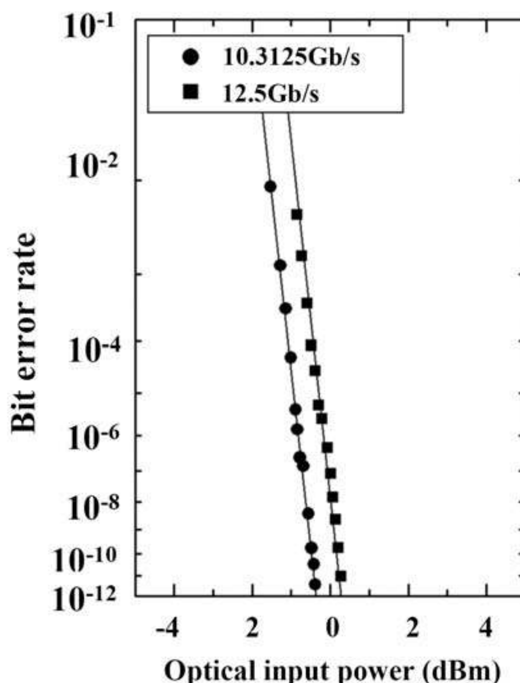

Figure 5.9 Bit-error rate *vs.* the optical input power at 1.3μm wavelength of the GaNAsSb-based UTC photodetector (25μm diameter) at data rates of 10.3125Gb/s and 12.5Gb/s for data transmission over a 10km single mode fiber.

The eye diagram and the BER results of the GaNAsSb-based UTC photodetectors at data rate up to 12.5Gb/s are the first reported fiber data transmission results of dilute nitride-based photodetector at such high data rate. Moreover, this is the first demonstration of the 1.3μm photodetectors on GaAs substrate in a 10Gb Ethernet fiber optic system. Previous data transmission reports on the application of 1.3μm photodetectors in the 10Gb Ethernet fiber optic system are entirely demonstrated using devices which are fabricated on the InP substrate.

ATTENTION: The Singapore Copyright Act applies to the use of this document. Nanyang Technological University Library

5.7 Summary

GaNAsSb-based UTC photodetectors with a temporal response pulsed FWHM of 46ps was demonstrated. Frequency response measurement at 1.3μm wavelength using a 10μm diameter device shows record 3dB cutoff frequency value of 14GHz, which is the highest reported cutoff frequency for a dilute nitride-based 1.3μm photodetector. Furthermore, the application of GaNAsSb-based UTC photodetector in a 10Gb Ethernet fiber-optic transmission links (10GBASE-LR) at 1.3μm wavelength was successfully demonstrated. The results of eye diagram and bit-error rate measurements confirm the capability of the GaNAsSb-based photodetector in the 10GBASE-LR system. This is the first demonstration of 10Gb Ethernet fiber-optic transmission at wavelength of 1.3μm using a dilute nitride-based photodetector.

ATTENTION: The Singapore Copyright Act applies to the use of this document. Nanyang Technological University Library

Chapter 6 GaNAsSb-based photoconductive switch

6.1 Introduction

Apart from the photodetectors discussed in chapters 4 and 5, the photoconductive switch is another alternative as a photon-detecting device. One of the major advantages of a photoconductive switch compared to a p-i-n photodetector is its simple device structure. Photoconductive switch usually consists of a single active layer, which is deposited on a semi insulating substrate. The simple device structure of the photoconductive switch makes it easier to monolithically integrate with other devices, such as a laser on the same chip. Smith *et al.* [18] demonstrated picosecond response in photoconductive switches based on low temperature grown gallium arsenide (LT-GaAs) as the active material in 1988. However, the optical bandgap of 1.43eV of GaAs prohibits the GaAs-based photoconductive switches to operate at common optical communication wavelengths of 1.3μm and 1.55μm.

Efforts such as utilization of the trap assisted two-step absorption in the LT-GaAs photoconductive switch have been demonstrated [21]. The use of trap-assisted absorption in the LT-GaAs photoconductive switch resulted in a weak photo-response at 1.55μm as the absorption process is not a band-to-band process. The utilization of small bandgap material such as LT-InGaAs [22-24] and ion-irradiated InGaAs [25] have also been reported. However, the carrier lifetime in the LT-InGaAs material [87] is relatively long (100ps). While the ion-irradiated

ATTENTION: The Singapore Copyright Act applies to the use of this document. Nanyang Technological University Library

InGaAs [25] has shown a reduced carrier lifetime down to the sub-picosecond regime (0.9ps), its low dark electrical resistivity value of <1Ω-cm is detrimental to the performance of the photoconductive switch. Presently, there is no viable material system for photoconductive switching at wavelength of 1.55μm, which has the characteristics of high photoresponsivity at 1.55μm, short carrier lifetime and high dark electrical resistivity.

In this chapter, the pulsed response of the GaNAsSb-based photoconductive switch was measured at wavelength of up to 1.6μm. The performance of the GaNAsSb-based photoconductive switch for microwave switching application is demonstrated by measuring its ON/OFF ratio at frequency up to 25GHz. This chapter also presents the improvement in the ON/OFF ratio of the GaNAsSb-based photoconductive switch at wavelength of 1.55μm by utilizing a smaller bandgap (0.8eV) lattice strained GaNAsSb layer.

6.2 Growth of GaNAsSb-based photoconductive switch

To fabricate the photoconductive switch, a sample with layer structure as shown in Figure 6.1(a) was grown using molecular beam epitaxy in conjunction with a RF N plasma source and a valved antimony cracker source. The 0.5μm-thick GaNAsSb layer was grown at 400°C at RF plasma power of 180W. The beam equivalent pressure (BEP) of the Sb flux was ~1.2×10^{-7} torr. Under these conditions, ~3.5% of

ATTENTION: The Singapore Copyright Act applies to the use of this document. Nanyang Technological University Library

nitrogen and 9% of Sb were incorporated into the GaNAsSb layer, which was confirmed by XRD. Dang *et al.* [55] have reported the bandgap of GaNAsSb material calculated using the BAC model. Using the BAC model, the optical bandgap of the GaNAsSb layer with 3.5% of nitrogen and 9% of Sb was estimated to be ~0.88eV.

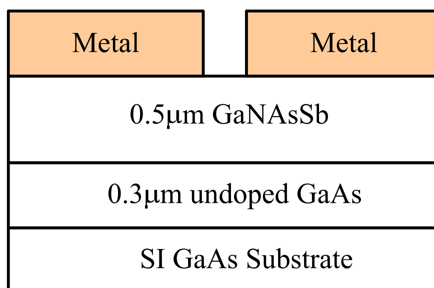

Figure 6.1 Schematic diagram of a GaNAsSb-based photoconductive switch structure.

6.3 Photoluminescence and refractive index measurement

Before depositing the Pt/Ti/Pt/Au contact metal, the sample was characterized using ellipsometry to measure the GaNAsSb refractive index and photoluminescence (PL) to verify the bandgap of the GaNAsSb layer. The refractive index measurement was performed using a spectroscopic ellipsometer at 70° of the incident angle. The wavelength was scanned from 800nm to 1700nm. The accuracy of refractive index in this measurement is ±0.001.

ATTENTION: The Singapore Copyright Act applies to the use of this document. Nanyang Technological University Library

The ellipsometry result is shown in Figure 6.2. The absorption coefficient of the GaNAsSb material was derived from the ellipsometry result and is shown in Figure 6.3. The GaNAsSb material shows absorption coefficient of 13000±90cm^{-1} and 700±80cm^{-1} at wavelength of 1.3μm and 1.55μm, respectively.

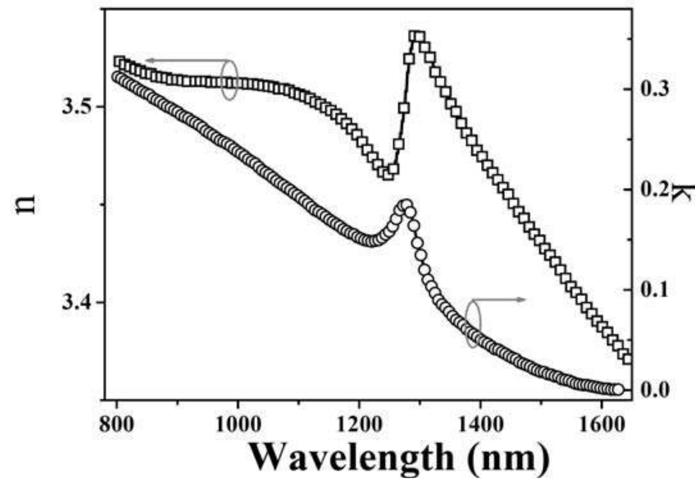

Figure 6.2 n-k plot *vs.* wavelength of the GaNAsSb material from refractive index measurement.

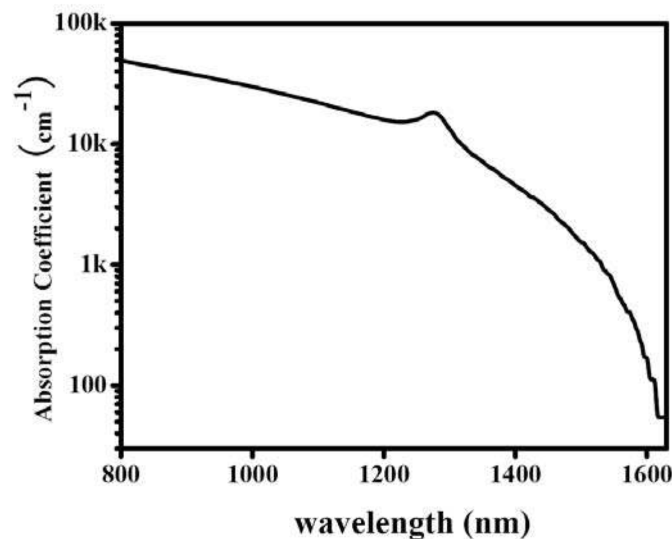

Figure 6.3 Absorption coefficient derived from the extinction coefficient (k) data set.

ATTENTION: The Singapore Copyright Act applies to the use of this document. Nanyang Technological University Library

The PL spectrum of the GaNAsSb sample is shown in Figure 6.4. It can be seen that the GaNAsSb layer exhibits a dominant peak at 0.875eV and a broad shoulder peak at 0.825eV. The dominant PL peak is attributed to band-to-band transition. The position of the dominant peak agrees well with the estimated bandgap value of 0.88eV. The broad shoulder peak could be due to nitrogen-related defects. The nitrogen-related defects have energy states ~0.1eV above the valence band. The transition of carriers from defect states to the conduction band could lead to the PL peak at 0.825eV. The transition of carriers from defect states to the conduction band also explains the weak absorption at 1.55μm observed in the refractive index measurement as shown in Figure 6.3.

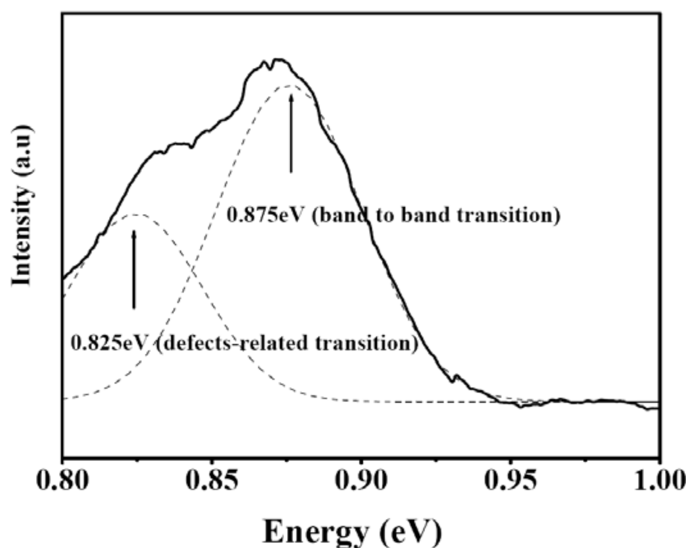

Figure 6.4 PL spectrum at 4K of the GaNAsSb material. The dashed lines are two Gaussian peaks used to fit the spectrum. Band-to-band transition gives rise to the main PL peak at 0.875eV. The shoulder peak at 0.825eV is attributed to transitions related to defects.

ATTENTION: The Singapore Copyright Act applies to the use of this document. Nanyang Technological University Library

6.4 Switch fabrication and resistivity

Photoconductive switches with different electrode gaps (1µm, 2µm, 5µm and 10µm) were fabricated using a standard photolithography process. The electrodes consist of two 150µm×150µm Pt(100Å)/Ti(300Å)/Pt(100Å)/Au(3000Å) contact pads and were deposited on the GaNAsSb active layer followed by 45s of rapid thermal annealing at 450°C.

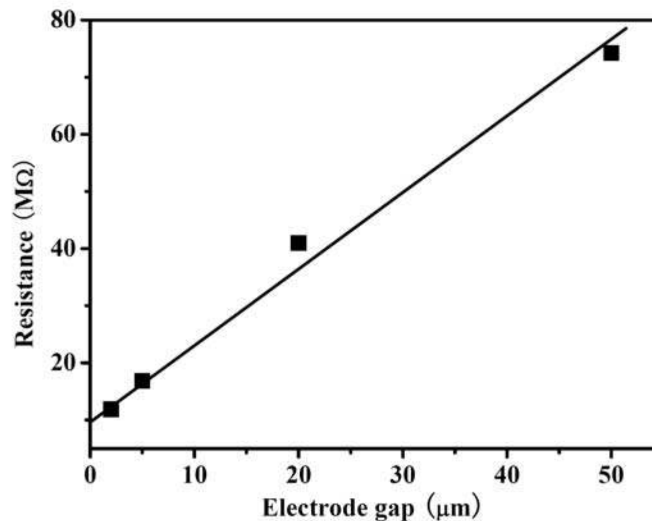

Figure 6.5 Plot of electrical resistance of GaNAsSb *vs*. electrode gap.

Current-voltage (I-V) characteristics measured at various electrode gaps show a linear behavior, which confirms the ohmic nature of the devices, including the metal-semiconductor contacts. The resistance values of various electrode gaps are shown in Figure 6.5. The resistivity of the GaNAsSb layer is calculated from the data in Figure 6.5 and has a value of ~9700Ωcm. The resistivity value of GaNAsSb is four orders higher compared to that of ion-irradiated InGaAs. This resistivity

ATTENTION: The Singapore Copyright Act applies to the use of this document. Nanyang Technological University Library

value validates the suitability of the GaNAsSb material for photoconductive microwave devices where a highly resistive semiconductor is essential.

Figure 6.6 shows the resistivity of the GaNAsSb under laser illumination at different optical powers. The wavelength of the laser is 810nm. The resistivity of the GaNAsSb decreases rapidly from 9700Ωcm to 170Ωcm as the laser power increases from 0mW to 21mW. The decrease in resistivity becomes less significant at laser power higher than 21mW. The resistivity of the GaNAsSb is ~60Ωcm at laser power of 90mW. The trend of resistivity change in the GaNAsSb in response to the optical power is typical and proportional to 1/(optical power). The relationship between resistivity of a semiconductor and optical power can be seen in Eqs. (2.18), (2.19) and (2.20).

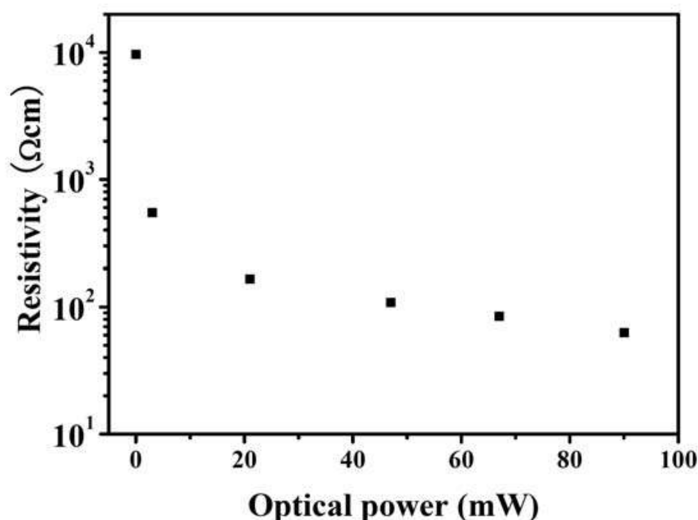

Figure 6.6 Resistivity of the GaNAsSb at different laser powers.

Figure 6.7 shows the resistivity of the GaNAsSb under 23mW laser excitation at different wavelengths. The resistivity is lowest at 810nm laser excitation and has a

ATTENTION: The Singapore Copyright Act applies to the use of this document. Nanyang Technological University Library

value of 170Ωcm. On the other hand, the 1550nm laser excitation is only capable of lowering the resistivity of the GaNAsSb from 9700Ωcm to 5300Ωcm. The different resistivity value of the GaNAsSb under different laser excitation wavelengths is due to the wavelength dependent absorption coefficient of the GaNAsSb as shown in Figure 6.3. The absorption of light of shorter wavelength is more efficient and generates more carriers compared to that of light of longer wavelength. This leads to lower resistivity of the GaNAsSb under 810nm laser excitation. In contrast, GaNAsSb has a lower absorption coefficient at 1.55um. This leads to fewer photo-generated carriers and thus higher resistivity.

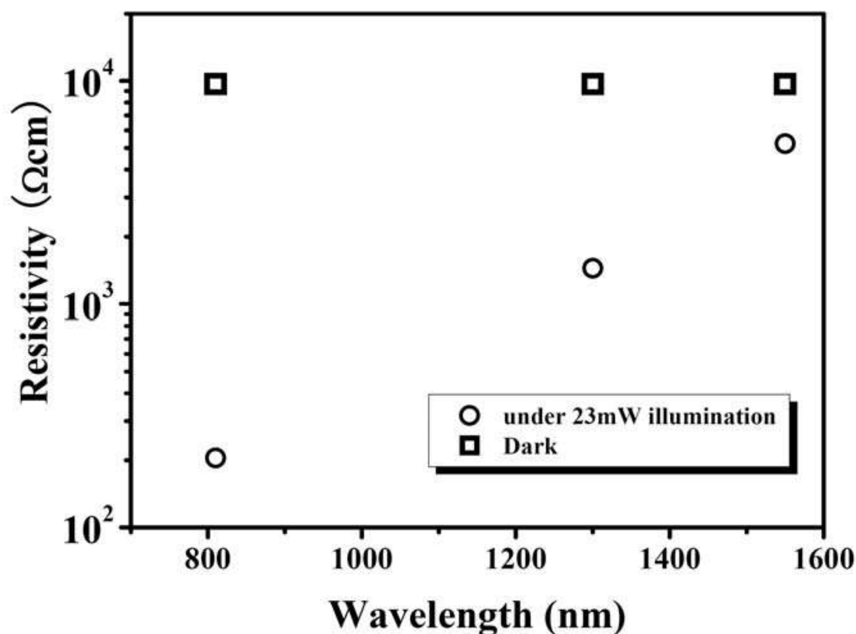

Figure 6.7 Resistivity of the GaNAsSb at different laser excitation wavelengths. The laser power is 23mW. The squares represent the dark resistivity of the GaNAsSb.

ATTENTION: The Singapore Copyright Act applies to the use of this document. Nanyang Technological University Library

6.5 Pulsed response measurement and carrier lifetime

The dynamic properties of the GaNAsSb layer were investigated by characterizing the pulsed response and carrier lifetime of the material upon absorption of femto second laser pulses [88]. The measurements of photoconductive pulsed response and carrier lifetimes of the GaNAsSb switch were carried out on a sample with 2μm electrode gap mounted on a DC-20 GHz alumina carrier as shown in Figure 6.8. An optical parametric oscillator (OPO) ultrafast pulsed solid state laser with Gaussian pulsed FWHM of 100fs and average power of 50mW was introduced into the device *via* free space top illumination. The laser has a circular beam spot size of 2μm in diameter and can be operated at optical wavelengths from 1.1μm to 1.6μm.

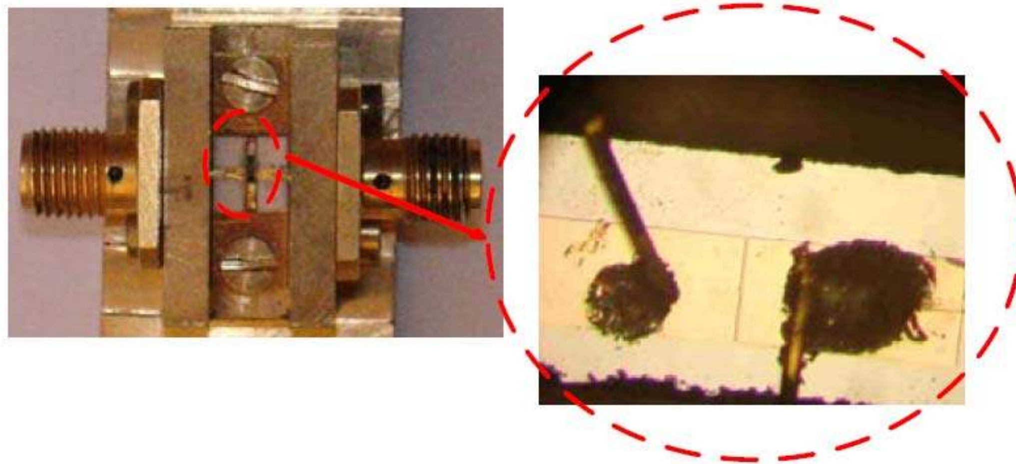

Figure 6.8 Top view of sub-miniature version A (SMA) alumina carrier of the GaNAsSb-based photoconductive switch with gap of 2μm.

The pulsed response of the GaNAsSb-based photoconductive switch under a negative DC bias of 0.8V was measured using a 50 GHz sampling oscilloscope. As

ATTENTION: The Singapore Copyright Act applies to the use of this document. Nanyang Technological University Library

shown in Figure 6.9, the device exhibits photo-response up to 1.6µm. The photoresponsivity of the device is the highest at 1.3µm and gradually decreases at longer wavelength. So far, there has been no other report on the photo-response characteristic at wavelength >1.55µm for any lattice-matched dilute nitride material system on GaAs substrate. Due to the GaNAsSb bandgap of 0.88eV, the pulsed response at wavelength >1.55µm cannot be attributed to band-to-band transition and is likely due to the absorption from transition between nitrogen-related defects and the conduction band. This is consistent with the observation in the refractive index and photoluminescence measurements discussed in section 6.3.

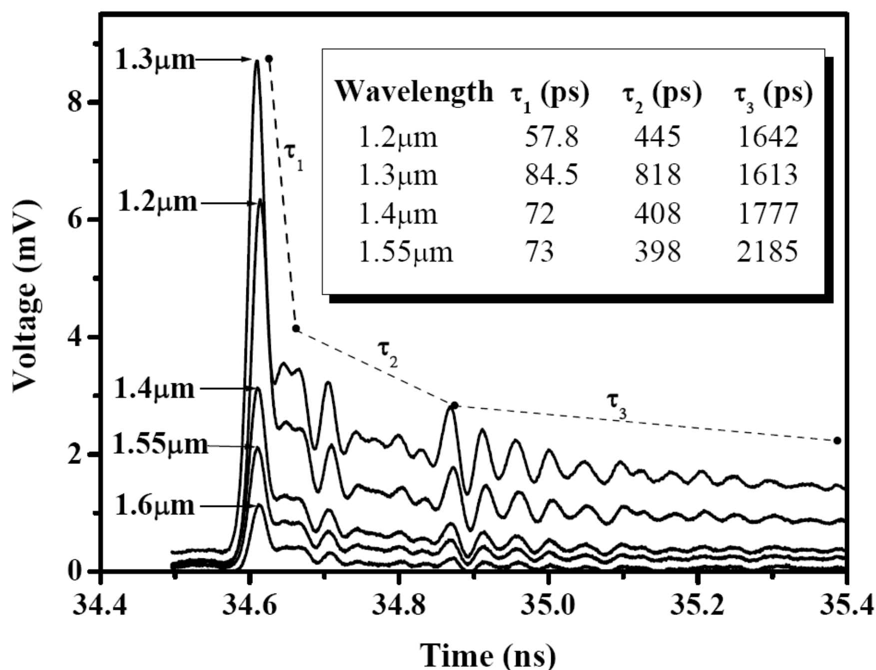

Figure 6.9 Pulsed response of GaNAsSb-based photoconductive switch at different laser excitation wavelengths. Inset shows carrier lifetimes of the GaNAsSb layer derived from pulsed measurement at different wavelengths.

ATTENTION: The Singapore Copyright Act applies to the use of this document. Nanyang Technological University Library

The measured FWHM of the pulses at wavelengths from 1.2μm to 1.6μm is ~30ps. This value is close to the time response limit of the SMA alumina carrier. Thus, the actual response time of the device may be shorter than the measured response time. Furthermore, as shown in the inset of Figure 6.9, there are three carrier recombination processes in the GaNAsSb layer at 1.2, 1.3, 1.4 and 1.55μm, giving rise to three values of carrier lifetimes represented by τ_1, τ_2 and τ_3, respectively. To explain the origin of these carrier lifetimes, the recombination processes in the GaNAsSb material and how they are affected by the defect levels have to be discussed.

From the three carrier lifetime values, it can be expected that three kinds of recombination processes occur in the GaNAsSb material. The first is band-to-band recombination, which is radiative for a direct bandgap material like GaNAsSb, and usually gives a relatively long carrier lifetime. The longest carrier lifetime in this measurement, τ_3, has a value of 2ns and can be attributed to this band-to-band recombination. The two shorter carrier lifetimes, τ_1 and τ_2, can be attributed to Shockley-Read-Hall (SRH) recombination related to two types of predominant defects in GaNAsSb: namely the mid-gap As antisite defects and the nitrogen-related defects.

In SRH recombination, the rate of recombination, U can be expressed as:

$$U \propto \frac{1}{\cosh(E_t - E_i)} \tag{6.1}$$

where E_t and E_i are the trap energy level and intrinsic Fermi level, respectively.

ATTENTION: The Singapore Copyright Act applies to the use of this document. Nanyang Technological University Library

Based on that Eq. (6.1), the highest rate of recombination is attained when E_i=E_t. In other words, trap with energy state at the middle of the bandgap is the most efficient recombination center. Thus, the mid-gap As antisite defect level should be a more effective recombination center compared to the nitrogen-related defect level which is located at 0.1eV above the conduction band. The As antisite defect was known to contribute to sub-picosecond carrier lifetime in LT-GaAs, as formation of As antisite defects occurs readily at low growth temperature. Consequently, the low growth temperature of the GaNAsSb (400°C) is more favorable for the formation of the As antisite defects compared to normal growth temperature (600°C). Similarly, Gupta *et al.* [89] have reported that GaAs grown at same temperature (400°C) using MBE has a carrier lifetime of ~70ps, which is closed to the value of τ_1. Thus, τ_1 can be safely attributed to the SRH recombination related to the midgap As antisite defect level. On the other hand, the second longest carrier lifetime, τ_2, can be attributed to the SRH recombination related to nitrogen-related defects as the energy level of the nitrogen-related defects is located away from the middle of the bandgap.

6.6 Microwave switching performance

The performance of the GaNAsSb-based photoconductive switch for microwave switching is characterized by its ON/OFF ratio measurement, where the S-parameters were extracted using a vector network analyzer with and without laser excitation. The laser has wavelength of 790nm and average power of 80mW.

ATTENTION: The Singapore Copyright Act applies to the use of this document. Nanyang Technological University Library

The ON/OFF ratio is derived from the difference in the S_{21} value with and without laser excitation. From Figure 6.10, it can be seen that the ON/OFF ratio is ~11dB at 1GHz and maintained above 0dB up to 15GHz. This value of ON/OFF ratio is significantly higher than that of the microwave photoconductive switch based on LT-GaAs [90].

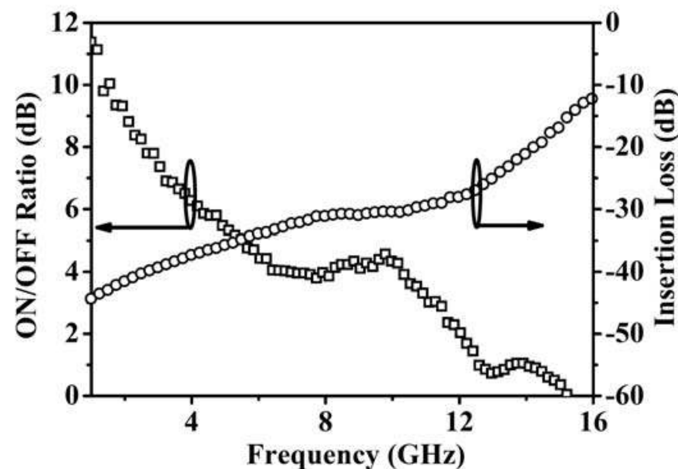

Figure 6.10 Plot of ON/OFF ratio and RF insertion losses of the GaNAsSb-based photoconductive switch at different frequencies.

At frequency of 10GHz, the ON/OFF ratio in LT-GaAs-based photoconductive switch is 1.45dB. On the other hand, the GaNAsSb-based photoconductive switch has an ON/OFF ratio of 5dB at frequency of 10GHz. The higher ON/OFF ratio in the GaNAsSb-based photoconductive switch compared to that in LT-GaAs-based photoconductive switch could be attributed to the longer carrier lifetime in the GaNAsSb layer. The carrier lifetime in LT-GaAs is <1ps. It is much shorter compared to the carrier lifetime in the GaNAsSb which is 60ps. Longer carrier lifetime allows collection of more photo-generated carriers in the GaNAsSb-based

ATTENTION: The Singapore Copyright Act applies to the use of this document. Nanyang Technological University Library

photoconductive switch. This leads to higher photoresponsivity in the GaNAsSb-based photoconductive switch compared to the LT-GaAs-based photoconductive switch. Higher photoresponsivity leads to higher ON/OFF ratio as the switch becomes more sensitive to the change in the light intensity.

Figure 6.10 also shows the insertion loss of the GaNAsSb-based photoconductive switch is at least 30dB at frequency <10GHz. This insertion loss value is high. A sophisticated photoconductive switch is expected to have insertion loss <5dB. The reason for the high insertion loss is discussed in the later part of this chapter.

The ON/OFF ratio measurement of the GaNAsSb-based photoconductive switch was repeated using lasers emitting at wavelengths of 1.3µm and 1.55µm. Figures 6.11 and 6.12 show the results of the measurements. The GaNAsSb-based photoconductive switch shows negligible ON/OFF ratio under laser excitation at wavelengths of 1.3µm and 1.55µm. The negligible ON/OFF ratio can be attributed to the low photoresponsivity of the GaNAsSb-based photoconductive switch at wavelengths of 1.3µm and 1.55µm. As shown previously in Figure 6.7, the change in resistivity of the GaNAsSb material with and without the laser excitation at wavelengths of 1.3µm and 1.55µm is smaller compared to that at wavelength of 810nm. Thus, higher photoresponsivity at wavelengths of 1.3µm and 1.55µm is needed to improve the ON/OFF ratio of the GaNAsSb-based photoconductive switch at these wavelengths.

ATTENTION: The Singapore Copyright Act applies to the use of this document. Nanyang Technological University Library

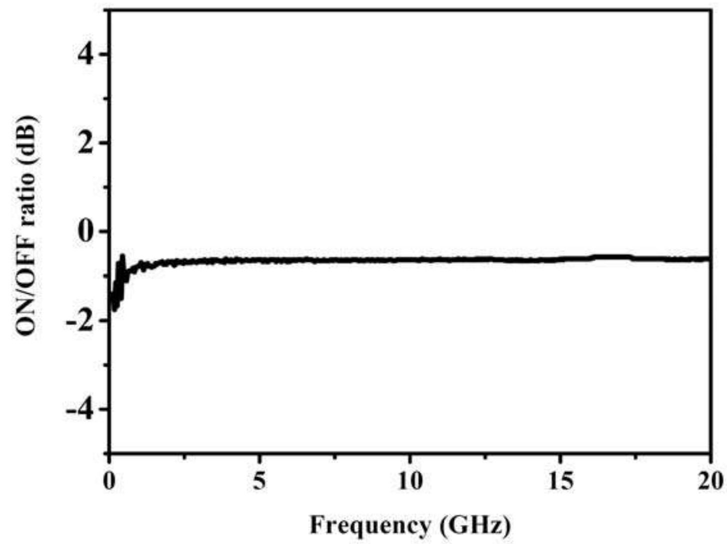

Figure 6.11 Plot of ON/OFF ratio of the GaNAsSb-based photoconductive switch at different frequencies under a 80mW laser excitation at 1.3μm.

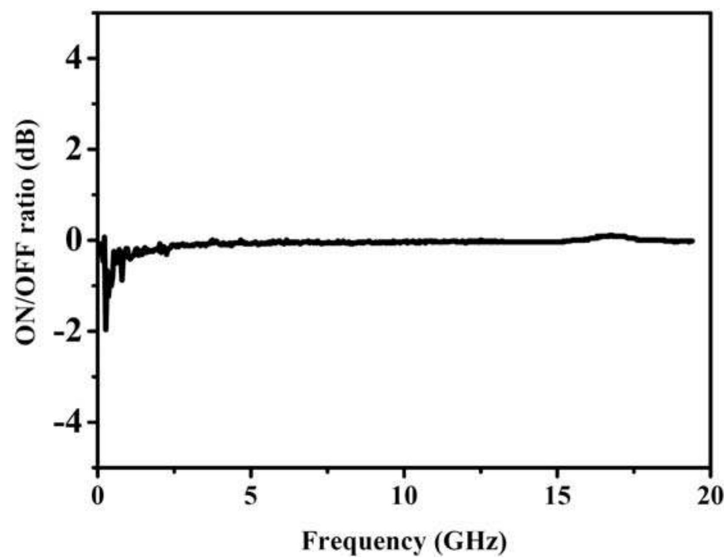

Figure 6.12 Plot of ON/OFF ratio of the GaNAsSb-based photoconductive switch at different frequencies under a 80mW laser excitation at 1.55μm.

ATTENTION: The Singapore Copyright Act applies to the use of this document. Nanyang Technological University Library

6.7 Improvement of ON/OFF ratio at 1.55μm

In section 6.6, the application of GaNAsSb-based photoconductive switch for microwave switching under laser excitation at 790nm is presented. The photoconductive switches have shown high dark electrical resistivity value (9700Ωcm) and short carrier lifetime (60ps). Pulsed response to incident light at wavelength of up to 1.6μm is also demonstrated. However, due to the GaNAsSb material having bandgap of 0.9eV, the photo-response of the device at 1.55μm is weak compared to that at short wavelength (i.e. 790nm). As a result, the GaNAsSb-based photoconductive switch was only capable of showing a positive ON/OFF ratio at wavelength up to 790nm for microwave switching application.

In this section, the characteristic of a GaNAsSb-based photoconductive switch with high photo-response under 1.55μm wavelength laser excitation for microwave switching is presented. The optical bandgap of the GaNAsSb material in the photoconductive switch is reduced to 0.8eV by increasing the concentration of nitrogen and antimony. New photoconductive switches with the GaNAsSb layer having bandgap energy of 0.8eV were grown and fabricated. Measurements were carried out on devices fabricated with different gap dimensions. Analysis of ON/OFF ratio of the GaNAsSb-based photoconductive switch is presented.

Figure 6.13(a) shows the structure of the GaNAsSb-based photoconductive switch. The sample was grown using molecular beam epitaxy in conjunction with a RF N

ATTENTION: The Singapore Copyright Act applies to the use of this document. Nanyang Technological University Library

plasma source and a valved antimony cracker cell. The 0.4μm-thick GaNAsSb layer was grown at 400°C. X-ray diffraction measurement shows the GaNAsSb layer is fully strained and contains 3.5% of nitrogen and 15% of antimony. From band anti-crossing (BAC) model [55], the bandgap of the GaNAsSb layer is estimated to be 0.8eV.

Photoconductive switches with different tapered electrode shapes (linear tapered, cosine tapered and exponential tapered) as shown in Figure 6.13(b) were fabricated. Figure 6.14 shows the schematic diagram of the switch with different tapered electrode shapes. The electrode gap and the width of the electrode are both 1μm. Moreover, the photoconductive switches with linear tapered electrodes were fabricated with electrode gaps measuring 1μm, 2μm and 5μm. These electrodes, made of Pt(100Å)/Ti(300Å)/Pt(100Å)/Au(3000Å) metallization, were deposited on the GaNAsSb active layer followed by 30s of rapid thermal annealing at 450°C.

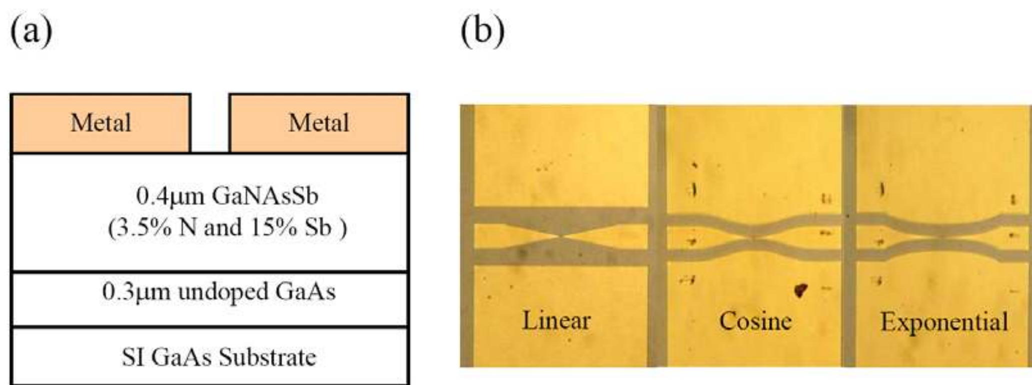

Figure 6.13 a) Schematic diagram of the GaNAsSb-based photoconductive switch structure. b) Optical microscope picture of the GaNAsSb-based photoconductive switch with different electrode shapes.

ATTENTION: The Singapore Copyright Act applies to the use of this document. Nanyang Technological University Library

The microwave switching performance of the GaNAsSb-based photoconductive switch is characterized by measuring its ON/OFF ratio, where the S-parameters (S_{21}) were extracted using a vector network analyzer with and without laser excitation at the electrode gap. The laser emits at wavelength of 1550nm and has an average power of 80mW. The ON/OFF ratio is derived from the difference in the S_{21} value with and without the laser excitation.

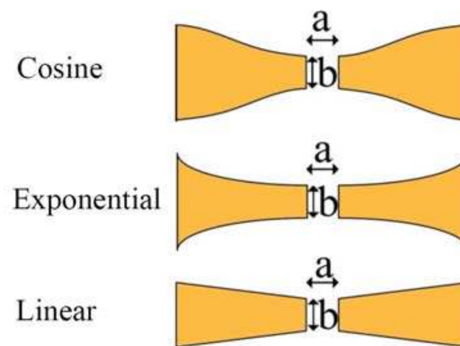

Figure 6.14 Schematic diagram of the switches with different electrode shapes. The electrode gap, a and the width of electrode, b are 1μm.

The ON/OFF ratio values of the photoconductive switches with different electrode shapes are shown in Figure 6.15. Tapered electrode is well known and widely used for broadband impedance matching in microwave devices [91-93]. The design of the different tapered electrodes in the GaNAsSb-based photoconductive switches is aimed to closely match the switch impedance to 50Ω and to improve the output microwave power under the laser illumination. However, the ON/OFF ratio does not change significantly with different electrode shapes as shown in Figure 6.15. This indicates the performance of the switches is not limited by the impedance mismatch of the electrodes. The results in Figure 6.15 could be explained by the

ATTENTION: The Singapore Copyright Act applies to the use of this document. Nanyang Technological University Library

high impedance in the switch under the laser illumination regardless of the electrode shape.

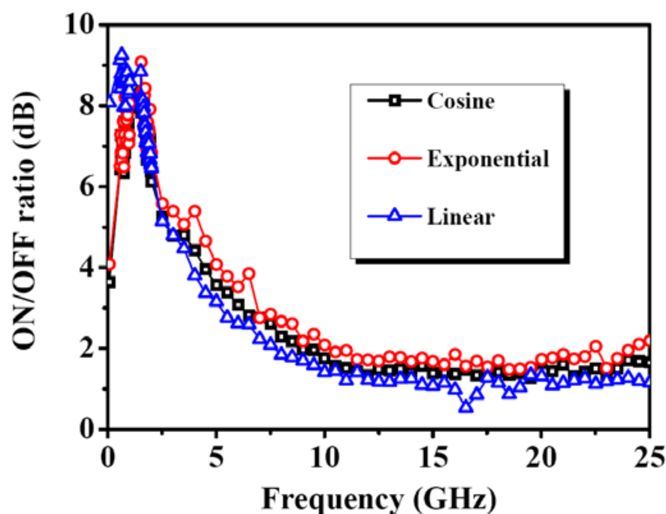

Figure 6.15 Plot of ON/OFF ratio of the GaNAsSb-based photoconductive switch with different electrode shapes as function of frequency.

Figure 6.16 shows the ON/OFF ratio of the photoconductive switches with linear tapered electrodes and electrode gaps of 1µm, 2µm and 5µm. At frequency <2GHz, the switches show an ON/OFF ratio value of 9dB, indicating that the devices are highly sensitive to 1.55µm laser excitation. This is the first demonstration of a photoconductive switch showing a positive ON/OFF ratio value under 1.55µm laser excitation.

At frequencies between 2GHz to 10GHz, the ON/OFF ratio drops rapidly to a level of 1dB. The magnitude and trend of the change in the ON/OFF ratio are independent of the electrode gap dimension. This suggests that the electrode gap resistance is not the main factor which degrades the ON/OFF ratio at high frequency.

ATTENTION: The Singapore Copyright Act applies to the use of this document. Nanyang Technological University Library

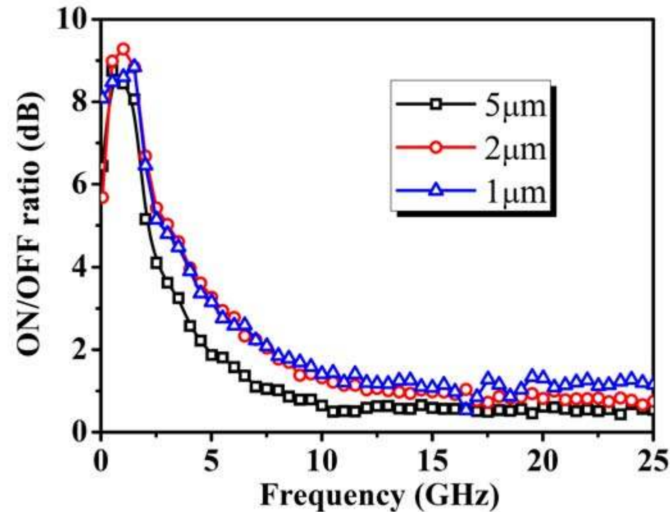

Figure 6.16 Plot of ON/OFF ratio of the GaNAsSb-based photoconductive switch with linear tapered electrode and electrode gaps of 1μm, 2μm and 5μm as function of frequency.

Figure 6.17 shows the insertion loss of the GaNAsSb-based photoconductive switch with linear tapered electrode and electrode gaps of 1μm, 2μm and 5μm. The photoconductive switch basically behaves as a light sensitive variable resistor in parallel with a gap capacitor. The insertion loss exhibits a flat response following increase in the frequency if the resistance of the switch is smaller compared to its capacitive reactance. Otherwise, the insertion loss decreases in response to increase in the frequency if the capacitive reactance is smaller compared to the resistance of the switch.

Figure 6.17 shows that the insertion loss decreases as the frequency increases, even at the low frequency region (<500MHz), where the capacitive reactance is extremely high (see Figure 6.18). This indicates that the switch has high ON state resistance of >10kΩ. This ON state resistance value is estimated from the insertion

ATTENTION: The Singapore Copyright Act applies to the use of this document. Nanyang Technological University Library

loss value of 46dB. The resistance of the switch consists of the electrode gap resistance and contact resistance. The change in the electrode gap distance affects the gap resistance of the switch. As shown in Figures 6.17 and 6.18, the high resistance nature of the switch bears no correlation to the electrode gap distance. Thus, the only likely cause of the high switch resistance is the contact resistance.

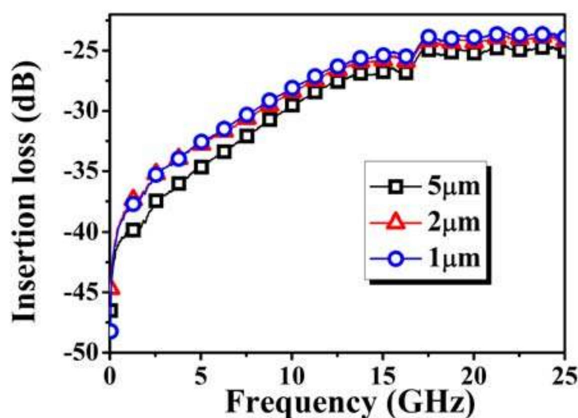

Figure 6.17 Plot of insertion loss of the GaNAsSb-based photoconductive switch with tapered electrode and electrode gaps of 1μm, 2μm and 5μm as function of frequency.

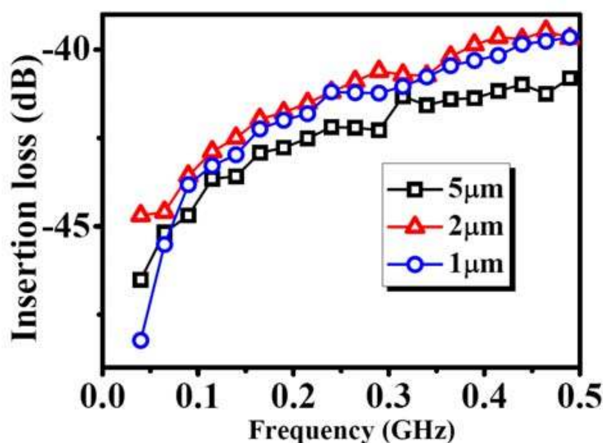

Figure 6.18 Plot of insertion loss of the GaNAsSb-based photoconductive switch with tapered electrode and electrode gaps of 1μm, 2μm and 5μm as function of frequency at the low frequency range (<500MHz).

ATTENTION: The Singapore Copyright Act applies to the use of this document. Nanyang Technological University Library

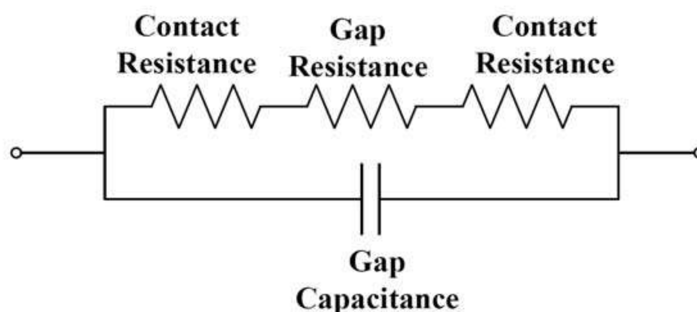

Figure 6.19 Equivalent circuit of a photoconductive switch.

The equivalent circuit of a photoconductive switch can be represented by the switch resistance in parallel with the gap capacitance as shown in Figure 6.19. The switch resistance consists of two contact resistances and the gap resistance. The gap capacitance of the GaNAsSb-based photoconductive switch is estimated to be 40fF by using the numerical calculation results from Meada *et al*. [94]. Using the value of gap capacitance, the insertion loss of the switch can be calculated. Figure 6.20 shows the calculated insertion loss at different switch resistance (R), assuming an output load of 50Ω.

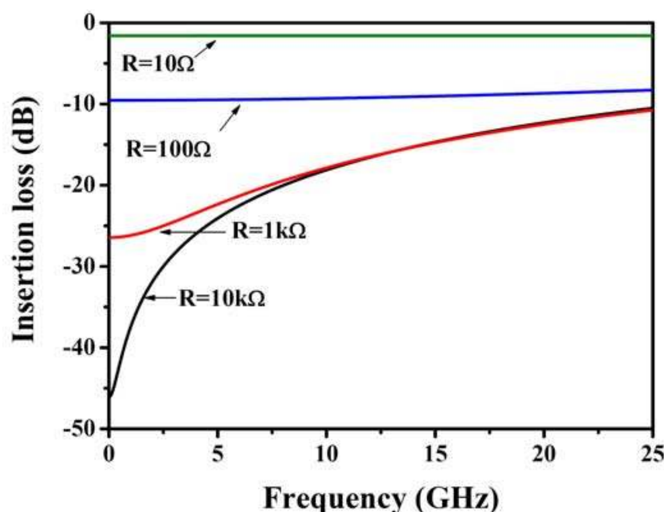

Figure 6.20 Plot of the calculated insertion loss of a photoconductive switch at different switch resistances, R as a function of frequency.

ATTENTION: The Singapore Copyright Act applies to the use of this document. Nanyang Technological University Library

It can be seen in Figure 6.20 that the high switch resistance, which is caused by the high contact resistance in the GaNAsSb-based photoconductive switch, leads to large insertion loss at the low frequency regime. This limits the ON/OFF ratio of the switch to 9dB as shown in Figure 6.16. Lower contact resistance will improve the maximum ON/OFF ratio of the switch by reducing the insertion loss.

Moreover, the high contact resistance also leads to the rapid decrease in the ON/OFF ratio at frequencies from 2 to 10GHz. At such frequencies, the switch impedance is mainly affected by the gap capacitance due to the high switch resistance. Since the gap capacitance hardly changes with or without the 1.55µm laser excitation at the electrode gap, the switch has negligible ON/OFF ratio at high frequency. It can be seen in Figure 6.20 that a reduction in the switch resistance leads to a smaller insertion loss. This could improve the magnitude of the ON/OFF ratio and extend the maximum frequency range of the switch to >10GHz.

Figure 6.20 shows the insertion loss of the switch is ~9dB and exhibits a flat response following increase in the frequency if the switch resistance is 100Ω. A photoconductive switch can exhibit an ON/OFF ratio >30dB and has maximum frequency >25GHz with such insertion loss. Thus, reduction in contact resistance is very important to improve the performance of the GaNAsSb-based photoconductive switch. Further investigation to improve the contact metallization

ATTENTION: The Singapore Copyright Act applies to the use of this document. Nanyang Technological University Library

technology of the GaNAsSb material is warranted to reduce the contact resistance from 10kΩ to <10Ω, which is normally found in GaAs-based ohmic contact.

6.8 Summary

In summary, GaNAsSb has been demonstrated as a viable material for 1.55µm photoconductive switch application. The GaNAsSb photoconductive switch shows characteristics of high dark electrical resistivity, short carrier lifetime and high photoresponsivity at 1.55µm. The GaNAsSb material shows dark electrical resistivity of 9700Ωcm. The resistivity of the GaNAsSb can be reduced to 60Ωcm under 90mW 810nm laser excitation. The photoconductive switch, with the GaNAsSb layer having bandgap energy of 0.9eV, shows low photoresponsivity and negligible ON/OFF ratio at 1.55µm. This is due to the non band-to-band photon-absorption at wavelength of 1.55µm. Thus, the bandgap of the GaNAsSb material is reduced to 0.8eV to ensure sufficient photon absorption of the light at wavelength of 1.55µm. The new photoconductive switch with the GaNAsSb layer having bandgap energy of 0.8eV shows ON/OFF ratio of 9dB at 1.55µm. Further analysis shows that high contact resistance limits the performance of the GaNAsSb-based photoconductive switch.

ATTENTION: The Singapore Copyright Act applies to the use of this document. Nanyang Technological University Library

Chapter 7 GaAs/GaNAsSb/GaAs 1.55μm optical waveguide system

7.1 Introduction

Apart from photon-detecting devices described in the previous chapters, GaNAsSb can also be applied to other applications, such as optical confinement and guiding due to the bandgap difference compared to GaAs. In this chapter, a GaAs/GaNAsSb/GaAs 1.55μm optical waveguide structure fabricated on a GaAs substrate as an alternative to the AlGaAs/GaAs system is demonstrated. The GaAs/GaNAsSb/GaAs system has two distinguishing features compared to the AlGaAs/GaAs/AlGaAs optical waveguide system. Firstly, the GaAs/GaNAsSb/GaAs system only transmits light at wavelength >1.4μm. Secondly, the GaAs/GaNAsSb/GaAs system is capable of using the GaAs substrate as the bottom cladding layer.

In this chapter, the near-field optical intensity distribution pattern in the waveguide is measured and the propagation loss of the waveguide with different ridge widths is reported. Furthermore, the effect of nitrogen-related defect absorption on the propagation loss is discussed.

ATTENTION: The Singapore Copyright Act applies to the use of this document. Nanyang Technological University Library

7.2 Growth and fabrication of waveguide

The rib optical waveguides with GaAs/GaNAsSb/GaAs double heterostructures as shown in Figure 7.1 were grown using MBE on N^+ GaAs (100) substrates. The n-type 0.3μm-thick GaAs buffer layer and 1.5μm-thick top GaAs layer were doped at ~5 x $10^{18}cm^{-3}$ to reduce the effective refractive index [95]. Silicon was used as the n-type dopant. The 0.4μm-thick undoped GaNAsSb layer was grown under identical conditions as the sample for refractive index measurement as shown in section 6.3. Under these conditions, the bandgap of the GaNAsSb layer is ~0.88eV. The optical waveguides were fabricated using optical lithography and wet etch process.

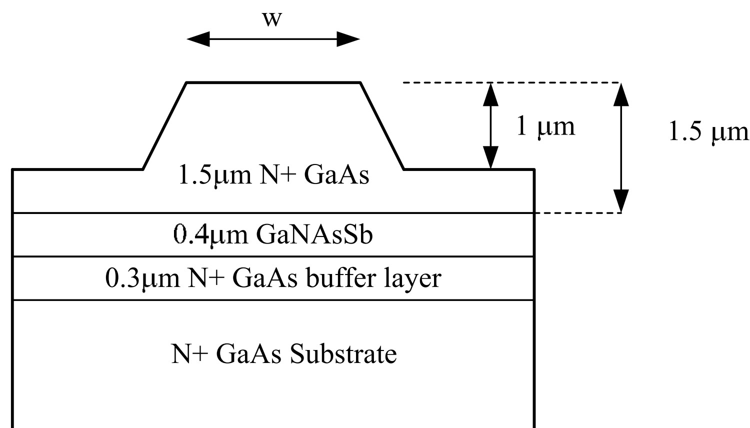

Figure 7.1 Cross section schematic of the GaAs/GaNAsSb/GaAs waveguide structure. The ridge widths of the waveguide are 4μm, 6.5μm and 8μm, respectively. The length of the waveguide is 2.1mm.

At 1.55μm, the real part of the refractive index (n) of GaNAsSb is 3.42 as shown in Figure 6.2. As expected, this value is higher than that of GaAs (3.37) [96]. Thus,

ATTENTION: The Singapore Copyright Act applies to the use of this document. Nanyang Technological University Library

the difference in refractive index between GaAs and GaNAsSb is ~1.5%, providing enough refractive index contrast for optical confinement at 1.55μm.

7.3 Near-field optical intensity distribution pattern measurement

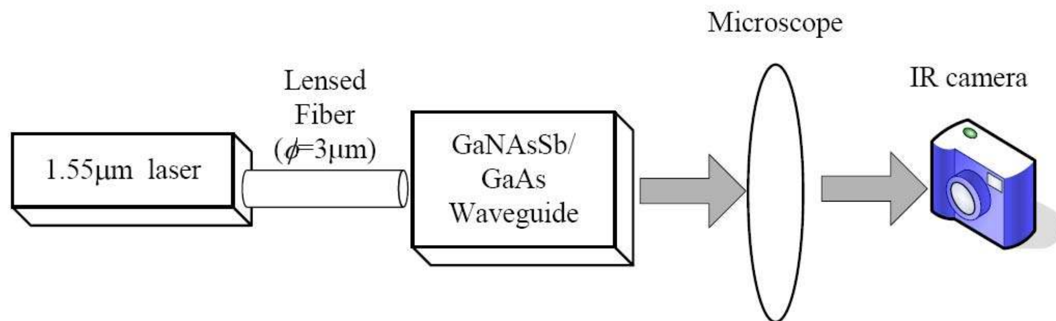

Figure 7.2 Schematic diagram of the experimental setup for the near-field optical intensity distribution pattern measurement.

For near-field optical intensity distribution pattern measurement, a 40X optical microscope and an infrared camera were used to capture the output of the waveguide. The schematic diagram of the experiment setup is shown in Figure 7.2. Figure 7.3 shows the near-field optical intensity distribution pattern of the waveguides with 4μm, 6.5μm and 8μm ridge widths, respectively.

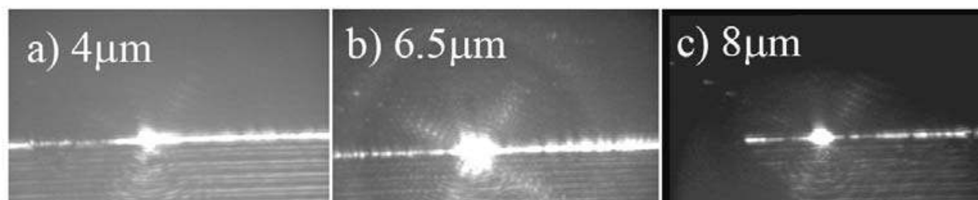

Figure 7.3 Near-field optical intensity distribution pattern of the waveguides with (a) 4μm, (b) 6.5μm and (c) 8μm ridge widths, respectively.

ATTENTION: The Singapore Copyright Act applies to the use of this document. Nanyang Technological University Library

The "lateral leakage of light" observed in Figure 7.3 is not due to the poor lateral confinement of the waveguide. There are two reasons which lead to this observation. Firstly, the lensed fiber has a divergence angle higher than 40°. Thus, part of the incident light was injected into the area beside the waveguide. The length of the waveguide used in this experiment, which is 2.1mm, is too short to eliminate the residual light at the area beside the waveguide. Secondly, the IR camera was saturated by the high intensity of the propagating light from the waveguide. Due to the saturation of the camera sensitivity, the "lateral leakage of light", which has a low optical power, appears to be as bright as the high power propagating light from the waveguide.

To eliminate the "lateral leakage of light", a new near-field optical intensity distribution pattern measurement was performed by using an input laser with lower light intensity. The results of the measurement are shown in Figure 7.4. It can be seen in Figure 7.4 that the "lateral leakage of light" is eliminated. A circular near-field optical intensity distribution pattern is observed at the output of each waveguide.

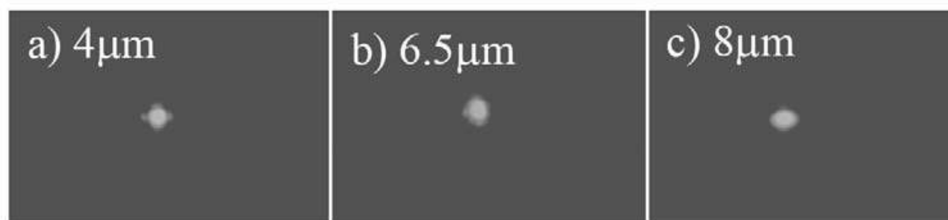

Figure 7.4 Near-field optical intensity distribution pattern of the waveguides with (a) 4μm, (b) 6.5μm and (c) 8μm ridge widths, respectively measured using an input laser with lower light intensity.

ATTENTION: The Singapore Copyright Act applies to the use of this document. Nanyang Technological University Library

Qualitatively, it can be observed in the near-field optical intensity pattern that the transmitted light can be properly confined in both the vertical and lateral directions of the waveguides, due to the refractive index difference between the GaNAsSb and GaAs layers.

7.4 Propagation loss

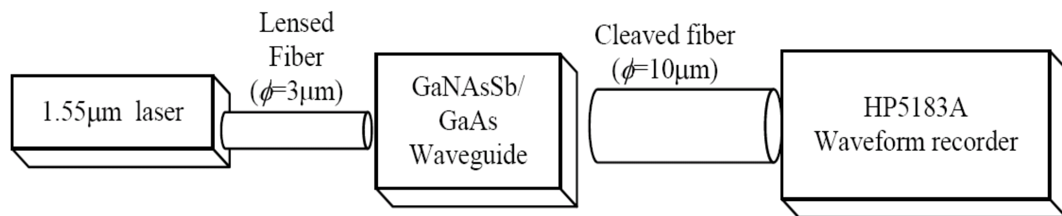

Figure 7.5 Schematic diagram of the experimental setup for the propagation loss measurement using the Fabry-Perot resonance.

Figure 7.5 shows the schematic diagram of the experimental set up for the propagation loss measurement using the Fabry-Perot resonance method. A 1.55μm tunable laser was used as the optical source. The end-fire coupling technique was used to couple the laser light from a 3μm lensed fiber into the GaAs/GaNAsSb/GaAs optical waveguide. The output optical power of the waveguide is collected using a 10μm cleaved fiber. The cleaved fiber is connected to a HP 5183A waveform recorder to measure the output optical power. The results of the Fabry Perot resonance measurement are shown in Figure 7.6

ATTENTION: The Singapore Copyright Act applies to the use of this document. Nanyang Technological University Library

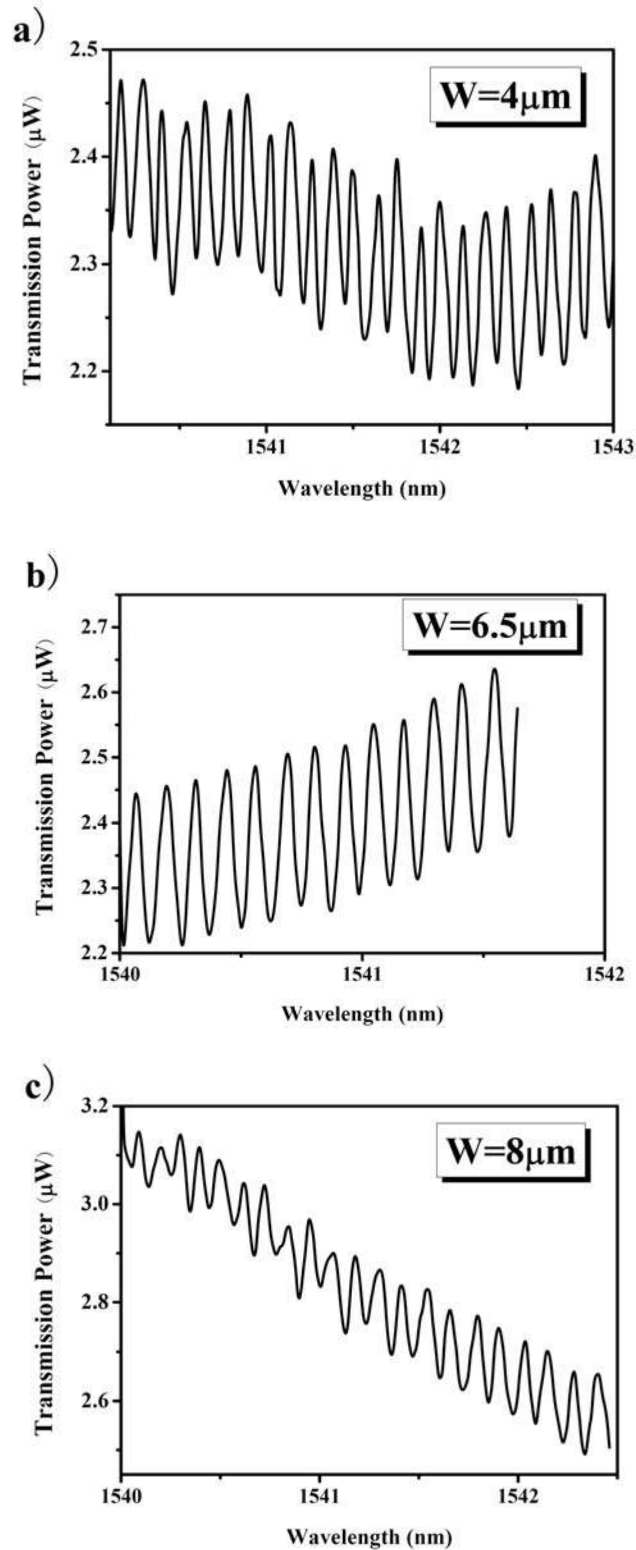

Figure 7.6 Fabry Perot resonance results of GaAs/GaNAsSb/GaAs waveguides with ridge width of (a) 4μm, (b) 6.5μm and (c) 8μm, respectively.

ATTENTION: The Singapore Copyright Act applies to the use of this document. Nanyang Technological University Library

The propagation loss, α_p can be deduced from the Fabry-Perot fringes measurements through the relationship:

$$\alpha_p = \frac{-10}{L}\log_{10}\left[\frac{1}{R}\frac{\sqrt{(I/i)}-1}{\sqrt{(I/i)}+1}\right] \qquad (7.1)$$

where L is the waveguide length and R is the classical Fresnel reflection coefficient at the waveguide facet. I is the output optical intensity at a maximum point of the fringes and i is the output optical intensity at a minimum point of the fringes.

The value of R can be obtained using the relationship:

$$R = \frac{(n_{eff}-1)^2}{(n_{eff}+1)^2} \qquad (7.2)$$

where n_{eff} is the effective index of the waveguide. The value of n_{eff} is obtained using numerical calculation based on the three dimensional beam propagation method [97]. From the simulation, the value of n_{eff} is 3.392.

From the results in Figure 7.6, the propagation loss of these waveguides is calculated using Eqs. (7.1) and (7.2). The propagation loss of these waveguides is found to be ~55 ± 10dB/cm and is independent of the waveguide ridge width. The waveguide ridge width can affect the propagation loss of a waveguide because it can change the propagation mode of the light in the waveguide. The results suggest that the propagation loss of the waveguide is not determined by the ridge width. Other factors, such as material properties of the GaNAsSb layer could be

ATTENTION: The Singapore Copyright Act applies to the use of this document. Nanyang Technological University Library

the overwhelming factor in determining the propagation loss of the GaAs/GaNAsSb/GaAs waveguide.

The propagation loss of the GaAs/GaNAsSb/GaAs waveguide is relatively high compared to the AlGaAs/GaAs system. The nitrogen-related defects absorption is probably the major contributor to this high propagation loss. As shown in Figure 6.3, the defect-related states lead to an absorption coefficient value of $700cm^{-1}$ at 1.55μm in the GaNAsSb material. Apparently, this is inconsistent with the expected bandgap of GaNAsSb (0.88eV) mentioned previously.

The PL measurement (4K) result shown in Figure 6.4 provides an explanation for this inconsistency. The measured PL spectrum has been de-convoluted into two Gaussian peaks: a main peak centered at ~0.875eV and a broad shoulder centered at 0.825eV. The main peak position is close to the expected bandgap of the GaNAsSb layer, which is likely to be due to band-to-band transition, while the shoulder peak at 0.825eV is broad and extended below 0.8eV. The shoulder peak could be due to nitrogen-related defects, which is located at ~0.1eV above the valence band [44]. Carrier transitions between this defect-related state and conduction band could give rise to this shoulder peak. Due to such intra-bandgap transitions, GaNAsSb exhibits absorption below its optical bandgap.

ATTENTION: The Singapore Copyright Act applies to the use of this document. Nanyang Technological University Library

The propagation loss, α_p of the waveguide is given by $\Gamma\alpha$, where Γ is the optical confinement factor and α is the absorption coefficient of the core layer. Γ is calculated using the three dimensional beam propagation method [97]. It has a value of 0.25. Using $\Gamma = 0.25$ and $\alpha = 700\text{cm}^{-1}$, the propagation loss in the waveguide due to the nitrogen-related defects absorption is ~800dB/cm. Therefore, the effect of nitrogen-related defect absorption alone is more than sufficient to explain the high propagation loss.

A reduction in the concentration of the nitrogen-related defects is needed to improve the performance of the GaAs/GaNAsSb/GaAs optical waveguide. Nitrogen-related defects lead to high background carrier concentration in the GaNAsSb material. As shown in Figure 4.3, the background carrier concentration decreases as the growth temperature of the GaNAsSb layer decreases. This indicates a lower concentration of nitrogen-related defects is present in the GaNAsSb layer grown at lower temperature. Thus, the propagation loss in the GaAs/GaNAsSb/GaAs waveguide could be reduced by lowering the growth temperature of the GaNAsSb layer.

It is noted that the measured value of the propagation loss is much lower than the derived value from the absorption coefficient in the refractive index measurement. One possible explanation for this difference is the *in-situ* thermal annealing during the growth of the 1.5μm-thick top GaAs layer (at 600°C for 90 minutes) in the

ATTENTION: The Singapore Copyright Act applies to the use of this document. Nanyang Technological University Library

waveguide sample. There was no *in-situ* thermal annealing of the sample used in the refractive index measurement. *In-situ* annealing of the waveguide sample could suppress the defect state density [98], leading to a lower value of absorption coefficient and thus lower propagation loss. This is an interesting observation. It suggests a further reduction in the propagation loss of the waveguide could be achieved by performing an optimized thermal annealing process on the GaNAsSb layer.

7.5 Summary

GaAs/GaNAsSb/GaAs waveguides have successfully demonstrated optical transmission at wavelength of 1.55µm. The near-field optical intensity distribution pattern measurement shows that the transmitted light can be properly confined in both vertical and lateral directions of the waveguides. However, there exists relatively high propagation loss due possibly to defect-related absorption in the GaNAsSb material. Defect reduction in the GaNAsSb material is a key strategy for improving the absorption loss in this system.

ATTENTION: The Singapore Copyright Act applies to the use of this document. Nanyang Technological University Library

Chapter 8 Conclusions and recommendations

8.1 Conclusions

In this thesis, GaNAsSb-based optoelectronic devices were grown using a solid-source molecular beam epitaxy system in conjunction with a RF N plasma source and a valved Sb cracker source. The RF plasma source generates nitrogen plasma that contains energetic ion species. These ion species could damage the film surface and lead to defect formation in the dilute nitride material. To reduce the nitrogen plasma induced defects, an ion deflection plates system was installed. The PL spectra of the GaNAs material show a significant improvement in the intensity after the installation. This indicates a reduction in the concentration of the defects.

A significant improvement in the photoresponsivity at wavelength of 1.3μm of the GaNAsSb-based p-i-n photodetectors was demonstrated. The photodetectors with the i-GaNAsSb layer grown at 350°C exhibit a record photoresponsivity value of ~12A/W. This is the highest photoresponsivity value ever reported for a dilute nitride-based photodetector. Such high responsivity indicates a carrier avalanche process in the devices, even at reverse bias voltage as low as 1V. The efficient carrier avalanche process in the photodetectors with the i-GaNAsSb layer grown at 350°C could be due to the high concentration of As antisite defects in the GaNAsSb layer. The As antisite defects lower the threshold energy, which is needed to initiate the carrier avalanche process.

ATTENTION: The Singapore Copyright Act applies to the use of this document. Nanyang Technological University Library

In temporal response measurement, the device shows a pulsed FWHM of 40.5ps. This corresponds to a 3dB cutoff frequency value of 4.5GHz. This frequency response is the first multi-GHz frequency response characteristic ever reported for a dilute nitride-based photodetector. However, the existence of the nitrogen-related defects in the GaNAsSb layer has limited the width of the depletion region, leading to a lower measured 3dB cutoff frequency value compared to the theoretically predicted 3dB cutoff frequency. Furthermore, these defects also induce a high leakage current in the photodetector.

The application of high-speed GaNAsSb-based p-i-n photodetectors in 5Gb/s fiber-optic transmission at wavelength of 1.3μm was successfully demonstrated. The eye diagram is clearly opened at data rate of 5Gb/s. Furthermore, the bit-error rate of the photodetector was measured at data rate of 2.5Gb/s and 5Gb/s. This is the first result on high data rate fiber-optic transmission at wavelength of 1.3μm using dilute nitride-based photodetectors. Data rate of 5Gb/s is insufficient to meet the requirements of the 10Gb Ethernet system. Thus, further improvement in the 3dB cutoff frequency of the GaNAsSb-based photodetector is needed.

To further extend the photo-response from 1380nm to 1600nm, the GaNAsSb-based p-i-n strained waveguide photodetectors were grown using molecular beam epitaxy. The device consists of a 0.4μm-thick strained GaNAsSb layer, with N and Sb contents of 3.5% and 18%, respectively. From the XRD

ATTENTION: The Singapore Copyright Act applies to the use of this document. Nanyang Technological University Library

measurement, the GaNAsSb layer has strain relaxation of 1%. The device shows photo-response up to wavelength of 1600nm in the spectral response. Moreover, photoresponsivity of 0.29A/W at 1550nm was demonstrated. This value of photoresponsivity has been achieved without any mirror system, such as in RCE-based devices.

MBE-grown GaNAsSb-based UTC photodetectors were fabricated to improve the high frequency performance of the GaNAsSb-based photodetector. The GaNAsSb-based UTC photodetectors exhibit a pulsed FHWM of 46ps in the temporal response measurement. The frequency response measurement at wavelength of 1.3µm using a 10µm diameter device shows record 3dB cutoff frequency of 14GHz. This is the highest ever reported 3dB cutoff frequency for GaAs-based dilute nitride 1.3µm photodetectors.

The application of the GaNAsSb-based UTC photodetector in 10Gb/s fiber-optic data transmission (10GBASE-LR) over a 10km SMF at 1.3µm was successfully demonstrated. The eye diagrams at data rates of 10.3125Gb/s and 12.5Gb/s are clearly opened. The bit-error-rate (BER) for the 25µm diameter GaNAsSb-based UTC photodetector was measured at data rates of 10.3125Gb/s and 12.5Gb/s. The photodetector sensitivity at BER of 4×10^{-12} is -0.38dBm at data rate of 10.3125Gb/s. The photodetector sensitivity at BER of 9.3×10^{-12} at data rate of 12.5Gb/s is 0.28dBm. The results of these measurements indicate that the

ATTENTION: The Singapore Copyright Act applies to the use of this document. Nanyang Technological University Library

GaNAsSb-based UTC photodetector is capable of meeting the requirements of the IEEE802.3ae specifications for the 10GBASE-LR application. This is the first result of such high data rate transmission at wavelength of 1.3µm using a GaAs-based photodetector.

A semiconductor which has characteristics of high resistivity and short carrier lifetime is an ideal candidate for the active material in a photoconductive switch. GaNAsSb has the two characteristics. A photoconductive switch with 0.5µm-thick GaNAsSb photon-absorption layer with 3.5% of N and 9% of Sb, exhibits a pulsed FWHM of 30ps in the pulsed response experiment. This value is close to the time response limit of the SMA alumina carrier. The switch also shows photo-response up to 1.6µm, assisted by the defects-related absorption. The application of the GaNAsSb-based photoconductive switch in microwave switching was also demonstrated. At wavelength of 790nm, the switch shows an ON/OFF ratio of 11dB at 1GHz and response up to 15GHz. This value of ON/OFF ratio is significantly higher than that of the LT-GaAs-based photoconductive switch. The GaNAsSb-based photoconductive switch shows negligible ON/OFF ratio at wavelengths of 1.3µm and 1.55µm. This is due to the inefficient photon-absorption process in the GaNAsSb layer at these wavelengths.

The bandgap of the GaNAsSb was reduced to ~0.8eV to increase the efficiency of the photon-absorption at wavelength of 1.55µm. The GaNAsSb-based

ATTENTION: The Singapore Copyright Act applies to the use of this document. Nanyang Technological University Library

photoconductive switch with a GaNAsSb layer having bandgap energy of 0.8eV, shows an ON/OFF ratio of 9dB at wavelength of 1.55µm. This suggests that the switch has high photoresponsivity at 1.55µm. There is a rapid drop in the ON/OFF ratio at the frequency region between 2GHz and 10GHz. The ON/OFF ratio is negligible at frequency >10GHz. Further analysis suggests that the high contact resistance limits the performance of the GaNAsSb-based photoconductive switch.

Apart from photon detection, the GaNAsSb material has also been applied to the optical waveguide application. A 1.55µm GaAs/GaNAsSb/GaAs optical waveguide grown by molecular beam epitaxy was demonstrated as an alternative to the AlGaAs/GaAs system. The 0.4µm-thick GaNAsSb guiding layer contains ~3.5% of N and 9% of Sb, resulting in optical bandgap of 0.88eV. The GaNAsSb layer has a refractive index value of 3.42 at wavelength of 1.55µm. The near-field optical intensity distribution pattern measurement shows that the transmitted light can be properly confined in the waveguides. The propagation loss of the waveguide was measured using the Fabry-Perot resonance method. The propagation loss of the waveguide is ~55 ± 10dB/cm. The high propagation loss could be due to nitrogen-related defect absorption. The defect-related absorption leads to an absorption coefficient value of 700cm^{-1} at 1.55µm. This leads to high propagation loss in the GaAs/GaNAsSb/GaAs waveguide.

ATTENTION: The Singapore Copyright Act applies to the use of this document. Nanyang Technological University Library

8.2 Recommendations for future research

The GaNAsSb-based p-i-n photodetectors exhibit high unintentional doping concentration and high dark current density as described in chapter four. The high unintentional doping concentration and high dark current density could be due to the nitrogen-related defects and the arsenic antisite defects. The growth of the GaNAsSb layer at low temperature (<400°C) has been shown to be capable of reducing the nitrogen-related defects, but it also introduces more As antisite defects into the layer. Evidently, it is important to investigate a method to lower the nitrogen-related defects without increasing the arsenic antisite defects. Only by reducing both types of defects, the high unintentional doping and high dark current issues which hinder the high frequency performance of the GaNAsSb-based p-i-n photodetector can be overcome.

In this thesis, a strained GaNAsSb layer has been utilized to extend the photo-response to 1.55µm. The XRD measurement result of the GaNAsSb layer shows strain relaxation of 1% which accounts for the high leakage current in the photodetector. To overcome this problem, methods such as the application of a strain compensating layer can be investigated to increase the critical thickness of the GaNAsSb layer with 3.5% of N and 18% of Sb.

The GaNAsSb-based UTC photodetectors exhibit a 3dB cutoff frequency value of

ATTENTION: The Singapore Copyright Act applies to the use of this document. Nanyang Technological University Library

14GHz in chapter five. It is capable of meeting the requirements of the 10GBASE-LR system. Due to the intrinsically low electron mobility in the GaNAsSb material, the 3dB cutoff frequency of the GaNAsSb-based UTC photodetectors is lower than that of GaAs or InGaAs-based UTC photodetectors. To increase the 3dB cutoff frequency, the structure of the GaNAsSb-based UTC photodetectors such as doping concentration and layer thickness has to be optimized in a way that overcomes the low electron mobility in the GaNAsSb material.

The GaNAsSb-based photoconductive switch shows an ON/OFF ratio value of 9dB at 1GHz and response up to 10GHz in microwave switching application at 1.55μm. The high contact resistance in the photoconductive switch limits the performance of the switch. Further investigation on methods to lower the contact resistance of the switch is certainly needed to improve the performance of the GaNAsSb-based photoconductive switch.

It is also important to increase the dark electrical resistivity of the GaNAsSb to improve the ON/OFF ratio of the GaNAsSb-based photoconductive switch. One possible way is to lower the growth temperature of the GaNAsSb layer. In low temperature-grown GaAs, a dark electrical resistivity value of 10MΩcm can be achieved by lowering the growth temperature to less than 250°C. Currently, the dark electrical resistivity of the GaNAsSb achieved here is 9700Ωcm. This is ~3

ATTENTION: The Singapore Copyright Act applies to the use of this document. Nanyang Technological University Library

orders lower compared to the dark electrical resistivity of the low temperature-grown GaAs. Intuitively, the dark electrical resistivity of the GaNAsSb will also be higher if it is grown at lower temperature. Thus, more investigation on the electrical properties of GaNAsSb grown at lower temperature is required.

The performance of the GaAs/GaNAsSb/GaAs optical waveguide is limited by the high propagation loss of the waveguide. Such high propagation loss could be caused by the nitrogen-related defects. The concentration of nitrogen-related defects can be reduced by lowering the growth temperature of the GaNAsSb layer. Thus, further investigation on the GaAs/GaNAsSb/GaAs optical waveguide incorporating a low temperature-grown GaNAsSb layer is needed. The analysis on the GaAs/GaNAsSb/GaAs optical waveguide in this thesis also suggests that thermal annealing treatment could reduce the propagation loss of the waveguide. Thus, more investigation on the effect of different thermal annealing conditions on the propagation loss of the waveguide is required.

ATTENTION: The Singapore Copyright Act applies to the use of this document. Nanyang Technological University Library

Bibliography

[1] J. Hecht, *Understanding Fiber Optics*. New York: Prentice Hall, 2002.

[2] G. P. Agrawal, *Fiber-Optic Communications Systems*. New York: John Wiley & Sons, 2002.

[3] J. S. Harris, "GaInNAs long-wavelength lasers: progress and challenges," *Semiconductor Science and Technology*, vol. 17, pp. 880-891, 2002.

[4] "ANSI standard Z136.1.," *ANSI standard Z136.1*.

[5] M. Weyers, M. Sato, and H. Ando, "Red shift of photoluminescence and absorption in dilute GaAsN alloy layers," *Japanese Journal of Applied Physics, Part 2 (Letters)*, vol. 31, pp. 853-5, 1992.

[6] M. Kondow, K. Uomi, A. Niwa, T. Kitatani, S. Watahiki, and Y. Yazawa, "GaInNAs: a novel material for long-wavelength-range laser diodes with excellent high-temperature performance," *Japanese Journal of Applied Physics, Part 1 (Regular Papers & Short Notes)*, vol. 35, pp. 1273-5, 1996.

[7] G. Ungaro, G. Le Roux, R. Teissier, and J. C. Harmand, "GaAsSbN: a new low-bandgap material for GaAs substrates," *Electronics Letters*, vol. 35, pp. 1246-8, 1999.

[8] J. C. Harmand, A. Caliman, E. V. K. Rao, L. Largeau, J. Ramos, R. Teissier, L. Travers, G. Ungaro, B. Theys, and I. F. L. Dias, "GaNAsSb: how does it compare with other dilute III-V-nitride alloys?," *Semiconductor Science and Technology*, vol. 17, pp. 778-84, 2002.

ATTENTION: The Singapore Copyright Act applies to the use of this document. Nanyang Technological University Library

[9] J. C. Harmand, G. Ungaro, L. Largeau, and G. Le Roux, "Comparison of nitrogen incorporation in molecular-beam epitaxy of GaAsN, GaInAsN, and GaAsSbN," *Applied Physics Letters*, vol. 77, pp. 2482-4, 2000.

[10] H. Ito, T. Furuta, S. Kodama, and T. Ishibashi, "InP/InGaAs uni-travelling-carrier photodiode with 310 GHz bandwidth," *Electronics Letters*, vol. 36, pp. 1809-10, 2000.

[11] I. Kimukin, N. Biyikli, B. Butun, O. Aytur, S. M. Unlu, and E. Ozbay, "InGaAs-based high-performance p-i-n photodiodes," *IEEE Photonics Technology Letters*, vol. 14, pp. 366-8, 2002.

[12] V. Gambin, "Long wavelength luminescence from GaInNAsSb on GaAs," *Ph.D. thesis*, Stanford University, 2002.

[13] D. Jackrel, H. Yuen, S. Bank, M. Wistey, J. Fu, X. Yu, Z. Rao, and J. S. Harris, "Thick lattice-matched GaInNAs films in photodetector applications," presented at Semiconductor Photodetectors II, San Jose, CA, USA, 2005.

[14] Q. Han, X. H. Yang, Z. C. Niu, H. Q. Ni, Y. Q. Xu, S. Y. Zhang, Y. Du, L. H. Peng, H. Zhao, C. Z. Tong, R. H. Wu, and Q. M. Wang, "1.55µm GaInNAs resonant-cavity-enhanced photodetector grown on GaAs," *Applied Physics Letters*, vol. 87, pp. 111105-1, 2005.

[15] H. Luo, J. A. Gupta, and H. C. Liu, "1.55µm GaNAsSb photodetector on GaAs," *Applied Physics Letters*, vol. 86, pp. 211121-1, 2005.

[16] E. Luna, M. Hopkinson, J. M. Ulloa, A. Guzman, and E. Munoz, "Dilute nitride based double-barrier quantum-well infrared photodetector operating in the near infrared," *Applied Physics Letters*, vol. 83, pp. 3111-13, 2003.

ATTENTION: The Singapore Copyright Act applies to the use of this document. Nanyang Technological University Library

[17] D. H. Auston, "Picosecond optoelectronic switching and gating in silicon," *Applied Physics Letters*, vol. 26, pp. 101-3, 1975.

[18] F. W. Smith, H. Q. Le, V. Diadiuk, M. A. Hollis, A. R. Calawa, S. Gupta, M. Frankel, D. R. Dykaar, G. A. Mourou, and T. Y. Hsiang, "Picosecond GaAs-based photoconductive optoelectronic detectors," *Applied Physics Letters*, vol. 54, pp. 890-2, 1989.

[19] A. Claverie, F. Namavar, and Z. Liliental-Weber, "Formation of As precipitates in GaAs by ion implantation and thermal annealing," *Applied Physics Letters*, vol. 62, pp. 1271-1273, 1993.

[20] A. Krotkus, S. Marcinkevicius, J. Jasinski, M. Kaminska, H. H. Tan, and C. Jagadish, "Picosecond carrier lifetime in GaAs implanted with high doses of As ions: an alternative material to low-temperature GaAs for optoelectronic applications," *Applied Physics Letters*, vol. 66, pp. 3304-3306, 1995.

[21] H. Erlig, S. Wang, T. Azfar, A. Udupa, H. R. Fetterman, and D. C. Streit, "LT-GaAs detector with 451fs response at 1.55μm via two-photon absorption," *Electronics Letters*, vol. 35, pp. 173-4, 1999.

[22] H. Kunzel, J. Bottcher, R. Gibis, and G. Urmann, "Material properties of $Ga_{0.47}In_{0.53}As$ grown on InP by low-temperature molecular beam epitaxy," *Applied Physics Letters*, vol. 61, pp. 1347-9, 1992.

[23] J. P. Ibbetson, J. S. Speck, A. C. Gossard, and U. K. Mishra, "Observation of arsenic precipitates in GaInAs grown at low temperature on InP," *Applied Physics Letters*, vol. 62, pp. 2209-2211, 1993.

ATTENTION: The Singapore Copyright Act applies to the use of this document. Nanyang Technological University Library

[24] S. Gupta, J. F. Whitaker, and G. A. Mourou, "Ultrafast carrier dynamics in III-V semiconductors grown by molecular-beam epitaxy at very low substrate temperatures" *Quantum Electronics, IEEE Journal of*, vol. 28, pp. 2464-2472, 1992.

[25] J. Mangeney, L. Joulaud, P. Crozat, J. M. Lourtioz, and J. Decobert, "Ultrafast response (~2.2ps) of ion-irradiated InGaAs photoconductive switch at 1.55μm," *Applied Physics Letters*, vol. 83, pp. 5551-5553, 2003.

[26] R. J. Kaplar, D. Kwon, S. A. Ringel, A. A. Allerman, S. R. Kurtz, E. D. Jones, and R. M. Sieg, "Deep levels in p- and n-type InGaAsN for high-efficiency multi-junction III-V solar cells," *Solar Energy Materials and Solar Cells*, vol. 69, pp. 85-91, 2001.

[27] W. K. Loke, S. F. Yoon, S. Wicaksono, K. H. Tan, and K. L. Lew, "Defect-induced trap-assisted tunneling current in GaInNAs grown on GaAs substrate," *Journal of Applied Physics*, vol. 102, pp. 054501-6, 2007.

[28] S. Wicaksono, S. F. Yoon, W. K. Loke, K. H. Tan, K. L. Lew, M. Zegaoui, J. P. Vilcot, D. Decoster, and J. Chazelas, "Effect of growth temperature on defect states of GaAsSbN intrinsic layer in GaAs/GaAsSbN/GaAs photodiode for 1.3μm application," *Journal of Applied Physics*, vol. 102, pp. 044505-7, 2007.

[29] W. K. Loke, S. F. Yoon, K. H. Tan, S. Wicaksono, and W. J. Fan, "Improvement of GaInNAs p-i-n photodetector responsivity by antimony incorporation," *Journal of Applied Physics*, vol. 101, pp. 033122-5, 2007.

ATTENTION: The Singapore Copyright Act applies to the use of this document. Nanyang Technological University Library

[30] W. M. Chen, I. A. Buyanova, C. W. Tu, and H. Yonezu, "Point defects in dilute nitride III-N-As and III-N-P," *Physica B: Condensed Matter*, vol. 376-377, pp. 545-551, 2006.

[31] A. J. Ptak, S. W. Johnston, S. Kurtz, D. J. Friedman, and W. K. Metzger, "A comparison of MBE- and MOCVD-grown GaInNAs," *Journal of Crystal Growth*, vol. 251, pp. 392-8, 2003.

[32] R. A. Mair, J. Y. Lin, H. X. Jiang, E. D. Jones, A. A. Allerman, and S. R. Kurtz, "Time-resolved photoluminescence studies of $In_xGa_{1-x}As_{1-y}N_y$," *Applied Physics Letters*, vol. 76, pp. 188-90, 2000.

[33] S. Wicaksono, S. F. Yoon, K. H. Tan, and W. K. Loke, "Characterization of small-mismatch GaAsSbN on GaAs grown by solid source molecular beam epitaxy," *Journal of Vacuum Science and Technology B: Microelectronics and Nanometer Structures*, vol. 23, pp. 1054-1059, 2005.

[34] A. J. N. Houghton, D. A. Andrews, G. J. Davies, and S. Richie, "Low-Loss optical waveguides in MBE-grown GaAs/GaAlAs heterostructures," *Optics Communications*, vol. 46, pp. 164-166, 1983.

[35] H. Inoue, K. Hiruma, K. Ishida, T. Asai, and H. Matsumura, "Low loss GaAs optical waveguides," *Journal of Lightwave Technology*, vol. T-3, pp. 1270-6, 1985.

[36] H. Hiruma, H. Inoue, K. Ishida, and H. Matsumura, "Low loss GaAs optical waveguides grown by the metalorganic chemical vapor deposition method," *Applied Physics Letters*, vol. 47, pp. 186-7, 1985.

ATTENTION: The Singapore Copyright Act applies to the use of this document. Nanyang Technological University Library

[37] E. Kapon and R. Bhat, "Low-loss single-mode GaAs/AlGaAs optical waveguides grown by organometallic vapor phase epitaxy," *Applied Physics Letters*, vol. 50, pp. 1628-30, 1987.

[38] H. Takeuchi and K. Oe, "Low-loss single-mode GaAs/AlGaAs miniature optical waveguides with straight and bending structures," *Journal of Lightwave Technology*, vol. 7, pp. 1044-54, 1989.

[39] M. Seto, A. Shahar, R. J. Deri, W. J. Tomlinson, and A. Yi-Yan, "GaAs/AlGaAs single-mode optical waveguides with low propagation loss and strong optical confinement," *Applied Physics Letters*, vol. 56, pp. 990-2, 1990.

[40] R. J. Deri and E. Kapon, "Low-loss III-V semiconductor optical waveguides," *IEEE Journal of Quantum Electronics*, vol. 27, pp. 626-40, 1991.

[41] B. Young Tae, P. Kyung Hyun, K. Sun Ho, C. Sang Sam, and L. Tong Kun, "Single-mode GaAs/AlGaAs W waveguides with a low propagation loss," *Applied Optics*, vol. 35, pp. 928-33, 1996.

[42] S. Wicaksono, S. F. Yoon, W. K. Loke, K. H. Tan, and B. K. Ng, "Effect of growth temperature on closely lattice-matched GaAsSbN intrinsic layer for GaAs-based 1.3µm p-i-n photodetector," *Journal of Applied Physics*, vol. 99, pp. 104502-1, 2006.

[43] K. H. Tan, S. F. Yoon, W. K. Loke, S. Wicaksono, K. L. Lew, A. Stohr, O. Ecin, A. Poloczek, A. Malcoci, and D. Jager, "High-speed picosecond pulse response GaNAsSb p-i-n photodetectors grown by rf plasma-assisted nitrogen molecular beam epitaxy," *Applied Physics Letters*, vol. 90, pp. 183515-1, 2007.

ATTENTION: The Singapore Copyright Act applies to the use of this document. Nanyang Technological University Library

[44] W. K. Loke, S. F. Yoon, K. H. Tan, S. Wicaksono, and W. J. Fan, "Improvement of GaInNAs p-i-n photodetector responsivity by antimony incorporation," *Journal of Applied Physics*, vol. 101, pp. 33122-1, 2007.

[45] K. H. Tan, S. F. Yoon, W. K. Loke, S. Wicaksono, T. K. Ng, K. L. Lew, A. Stohr, S. Fedderwitz, M. Weiss, D. Jager, N. Saadsaoud, E. Dogheche, D. Decoster, and J. Chazelas, "High responsivity GaNAsSb p-i-n photodetectors at 1.3µm grown by radio-frequency nitrogen plasma-assisted molecular beam epitaxy," *Optics Express*, vol. 16, pp. 7720-7725, 2008.

[46] S. Fedderwitz, A. Stohr, S. F. Yoon, K. H. Tan, M. Weiss, W. K. Loke, A. Poloczek, S. Wicaksono, and D. Jager, "Multigigabit 1.3µm GaNAsSb/GaAs photodetectors," *Applied Physics Letters*, vol. 93, pp. 033509-3, 2008.

[47] K. H. Tan, S. F. Yoon, S. Fedderwitz, A. Stohr, W. K. Loke, S. Wicaksono, T. K. Ng, M. Weiss, A. Poloczek, V. Rymanov, A. S. Patra, E. Tangdiongga, and D. Jager, "14-GHz GaNAsSb Unitraveling-Carrier 1.3µm photodetectors grown by RF plasma-assisted nitrogen molecular beam epitaxy," *Electron Device Letters, IEEE*, vol. 30, pp. 590-592, 2009.

[48] W. K. Loke, S. F. Yoon, Z. Xu, K. H. Tan, T. K. Ng, Y. K. Sim, S. Wicaksono, N. Saadsaoud, D. Decoster, and J. Chazelas, "GaNAsSb/GaAs waveguide photodetector with response up to 1.6µm grown by molecular beam epitaxy," *Applied Physics Letters*, vol. 93, pp. 081102-3, 2008.

ATTENTION: The Singapore Copyright Act applies to the use of this document. Nanyang Technological University Library

[49] K. H. Tan, S. F. Yoon, C. Tripon-Canseliet, W. K. Loke, S. Wicaksono, S. Faci, N. Saadsaoud, J. F. Lampin, D. Decoster, and J. Chazelas, "GaNAsSb material for ultrafast microwave photoconductive switching application," *Applied Physics Letters*, vol. 93, pp. 063509-3, 2008.

[50] K. H. Tan, S. F. Yoon, W. K. Loke, S. Wicaksono, Z. Xu, T. K. Ng, K. L. Lew, N. Saadsaoud, M. Zegaoui, D. Decoster, and J. Chazelas, "1.55μm GaAs/GaNAsSb/GaAs optical waveguides grown by radio frequency nitrogen plasma-assisted molecular beam epitaxy," *Applied Physics Letters*, vol. 92, pp. 113513-1, 2008.

[51] R. Teissier, D. Sicault, J. C. Harmand, G. Ungaro, G. Le Roux, and L. Largeau, "Temperature-dependent valence band offset and band-gap energies of pseudomorphic GaAsSb on GaAs," *Journal of Applied Physics*, vol. 89, pp. 5473-7, 2001.

[52] S. Sakai, Y. Ueta, and Y. Terauchi, "Band gap energy and band lineup of III-V alloy semiconductors incorporating nitrogen and boron," *Japanese Journal of Applied Physics, Part 1 (Regular Papers & Short Notes)*, vol. 32, pp. 4413-17, 1993.

[53] W. Shan, W. Walukiewicz, J. W. Ager, III, E. E. Haller, J. F. Geisz, D. J. Friedman, J. M. Olson, and S. R. Kurtz, "Band anticrossing in GaInNAs alloys," *Physical Review Letters*, vol. 82, pp. 1221-4, 1999.

[54] I. Vurgaftman and J. R. Meyer, "Band parameters for nitrogen-containing semiconductors," *Journal of Applied Physics*, vol. 94, pp. 3675-96, 2003.

ATTENTION: The Singapore Copyright Act applies to the use of this document. Nanyang Technological University Library

[55] Y. X. Dang, W. J. Fan, S. T. Ng, S. Wicaksono, S. F. Yoon, and D. H. Zhang, "Study of interdiffusion in GaAsSbNGaAs quantum well structure by ten-band kp method," *Journal of Applied Physics*, vol. 98, pp. 026102, 2005.

[56] T. P. Lee and T. Li, "Photodetectors," in *Optical Fiber Telecommunications* S. E. Miller and A. G. Chynoweth, Eds. San Diego: Academic Press, 1979, pp. Chapter 18.

[57] T. Ishibashi, S. Kodama, N. Shimizu, and T. Furuta, "High-speed response of uni-traveling-carrier photodiodes," *Japanese Journal of Applied Physics, Part 1 (Regular Papers, Short Notes & Review Papers)*, vol. 36, pp. 6263-8, 1997.

[58] N. Shimizu, N. Watanabe, T. Furuta, and T. Ishibashi, "High-speed InP/InGaAs uni-traveling-carrier photodiodes with 3-dB bandwidth over 150 GHz," presented at Device Research Conference Digest, New York, NY, USA, 1997.

[59] W. C. Nunnally, "High-power microwave generation using optically activated semiconductor switches," *Electron Devices, IEEE Transactions on*, vol. 37, pp. 2439-2448, 1990.

[60] K. S. Kelkar, "Silicon carbide as a photo conductive switch material for high power applications," *Ph.D. thesis,* University of Missouri-Columbia, 2006, pp. 11.

[61] P. D. Brewer, D. H. Chow, and R. H. Miles, "Atomic antimony for molecular beam epitaxy of high quality III-V semiconductor alloys," *Journal of Vacuum Science and Technology B*, vol. 14, pp. 2335-8, 1996.

ATTENTION: The Singapore Copyright Act applies to the use of this document. Nanyang Technological University Library

[62] M. A. G. Halliwell, "X-ray diffraction solutions to heteroepitaxial growth problems," Netherlands, 1997.

[63] S. Wicaksono, S. F. Yoon, K. H. Tan, and W. K. Cheah, "Concomitant incorporation of antimony and nitrogen in GaAsSbN lattice-matched to GaAs," *Journal of Crystal Growth*, vol. 274, pp. 355-61, 2005.

[64] R. C. Powell, N. E. Lee, Y. W. Kim, and J. E. Greene, "Heteroepitaxial wurtzite and zinc-blende structure GaN grown by reactive-ion molecular-beam epitaxy. Growth kinetics, microstructure, and properties," *Journal of Applied Physics*, vol. 73, pp. 189, 1993.

[65] K. H. Shim, "Structural and optical properties of GaN-based heterostructures grown by plasma-assisted molecular beam epitaxy," vol. Ph.D: University of Illinois at Urbana-Champaign, 1997.

[66] M. A. Wistey, "Growth of 1.5μm gallium indium nitrogen arsenic antimonide vertical cavity surface emitting lasers by molecular beam epitaxy," *Ph.D. thesis*, Stanford University, 2005.

[67] W. K. Cheah, W. J. Fan, S. F. Yoon, D. H. Zhang, B. K. Ng, W. K. Loke, R. Liu, and A. T. S. Wee, "GaAs-based heterojunction p-i-n photodetectors using pentanary InGaAsNSb as the intrinsic layer," *IEEE Photonics Technology Letters*, vol. 17, pp. 1932-4, 2005.

[68] W. K. Loke, S. F. Yoon, S. Wicaksono, and B. K. Ng, "Characteristics of non-annealed λ=1.35μm closely lattice-matched GaInNAs/GaAs p-i-n photodetector structures grown by solid-source molecular beam epitaxy," *Materials Science and Engineering: B*, vol. 131, pp. 40-44, 2006.

ATTENTION: The Singapore Copyright Act applies to the use of this document. Nanyang Technological University Library

[69] J. S. Ng, W. M. Soong, M. J. Steer, M. Hopkinson, J. P. R. David, J. Chamings, S. J. Sweeney, and A. R. Adams, "Long wavelength bulk GaInNAs p-i-n photodiodes lattice matched to GaAs," *Journal of Applied Physics*, vol. 101, pp. 64506-1, 2007.

[70] M. Reason, H. A. McKay, W. Ye, S. Hanson, R. S. Goldman, and V. Rotberg, "Mechanisms of nitrogen incorporation in GaAsN alloys," *Applied Physics Letters*, vol. 85, pp. 1692-1694, 2004.

[71] K. H. Tan, S. F. Yoon, W. K. Loke, S. Wicaksono, Z. Xu, T. K. Ng, K. L. Lew, N. Saadsaoud, M. Zegaoui, D. Decoster, and J. Chazelas, "1.55μm GaAs/GaNAsSb/GaAs optical waveguides grown by radio frequency nitrogen plasma-assisted molecular beam epitaxy," *Applied Physics Letters*, 2007.

[72] C. Hu, K. A. Anselm, B. G. Streetman, and J. C. Campbell, "Noise characteristics of thin multiplication region GaAs avalanche photodiodes," *Applied Physics Letters*, vol. 69, pp. 3734-6, 1996.

[73] J. S. Ng, J. P. R. David, G. J. Rees, and J. Allam, "Avalanche breakdown voltage of $In_{0.53}Ga_{0.47}As$," *Journal of Applied Physics*, vol. 91, pp. 5200-2, 2002.

[74] W. Shockley, "Problems related to p-n junctions in silicon," *Solid-State Electronics*, vol. 2, pp. 35-67, 1961.

[75] R. A. Logan, A. G. Chynoweth, and B. G. Cohen, "Avalanche breakdown in gallium arsenide P-N junctions," *Physical Review*, vol. 128, pp. 2518-2523, 1962.

ATTENTION: The Singapore Copyright Act applies to the use of this document. Nanyang Technological University Library

[76] R. A. Logan and H. G. White, "Charge multiplication in GaP p-n junctions," *Journal of Applied Physics*, vol. 36, pp. 3945-3946, 1965.

[77] L. Partain, D. Day, and R. Powell, "Metastable impact ionization of traps model for lock-on in GaAs photoconductive switches," *Journal of Applied Physics*, vol. 74, pp. 335-40, 1993.

[78] M. Gallant, N. Puetz, A. Zemel, and F. R. Shepherd, "Metalorganic chemical vapor deposition InGaAs p-i-n photodiodes with extremely low dark current," *Applied Physics Letters*, vol. 52, pp. 733-5, 1988.

[79] S. Y. Xie, S. F. Yoon, and S. Z. Wang, "Effects of thermal annealing on deep-level defects and minority-carrier electron diffusion length in Be-doped InGaAsN," *Journal of Applied Physics*, vol. 97, pp. 73702-1, 2005.

[80] S. B. Zhang and S.-H. Wei, "Nitrogen solubility and induced defect complexes in epitaxial GaAs:N," *Physical Review Letters*, vol. 86, pp. 1789-1792, 2001.

[81] A. Stohr, A. Malcoci, A. Sauerwald, I. C. Mayorga, R. Gusten, and D. S. Jager, "Ultra-wide-band traveling-wave photodetectors for photonic local oscillators," *Journal of Lightwave Technology*, vol. 21, pp. 3062-3070, 2003.

[82] W. J. Fan, S. F. Yoon, T. K. Ng, S. Z. Wang, W. K. Loke, R. Liu, and A. Wee, "Comparison of nitrogen compositions in the as-grown GaNxAs1-x on GaAs measured by high-resolution X-ray diffraction and secondary-ion mass spectroscopy," *Applied Physics Letters*, vol. 80, pp. 4136-8, 2002.

ATTENTION: The Singapore Copyright Act applies to the use of this document. Nanyang Technological University Library

[83] S. Wicaksono, S. F. Yoon, W. K. Loke, K. H. Tan, K. L. Lew, M. Zegaoui, J. P. Vilcot, D. Decoster, and J. Chazelas, "Effect of growth temperature on defect states of GaAsSbN intrinsic layer in GaAs/GaAsSbN/GaAs photodiode for 1.3µm application," *Journal of Applied Physics*, vol. 102, pp. 044505-1, 2007.

[84] L. Yu-Tai, J. W. Shi, H. Cheng-Yu, C. Nan-Wei, C. Shu-Han, J. I. Chyi, and P. Ci-Ling, "Characterization of sub-THz photonic-transmitters based on GaAs-AlGaAs uni-traveling-carrier photodiodes and substrate-removed broadband antennas for impulse-radio communication," *IEEE Photonics Technology Letters*, vol. 20, pp. 1342-4, 2008.

[85] E. P. O'Reilly, A. Lindsay, and S. Fahy, "Theory of the electronic structure of dilute nitride alloys: beyond the band-anti-crossing model," *Journal of Physics: Condensed Matter*, vol. 16, pp. 3257-76, 2004.

[86] J. F. Geisz, D. J. Friedman, J. M. Olson, S. R. Kurtz, and B. M. Keyes, "Photocurrent of 1eV GaInNAs lattice-matched to GaAs," *Journal of Crystal Growth*, vol. 195, pp. 401-408, 1998.

[87] R. Takahashi, Y. Kawamura, T. Kagawa, and H. Iwamura, "Ultrafast 1.55µm photoresponses in low-temperature-grown InGaAs/InAlAs quantum wells," *Applied Physics Letters*, vol. 65, pp. 1790-2, 1994.

[88] D. Vignaud, D. A. Yarekha, J. F. Lampin, M. Zaknoune, S. Godey, and F. Mollot, "Electron lifetime measurements of heavily C-doped InGaAs and GaAsSb as a function of the doping density," *Applied Physics Letters*, vol. 90, pp. 242104-3, 2007.

ATTENTION: The Singapore Copyright Act applies to the use of this document. Nanyang Technological University Library

[89] S. Gupta, M. Y. Frankel, J. A. Valdmanis, J. F. Whitaker, G. A. Mourou, F. W. Smith, and A. R. Calawa, "Subpicosecond carrier lifetime in GaAs grown by molecular beam epitaxy at low temperatures," *Applied Physics Letters*, vol. 59, pp. 3276-3278, 1991.

[90] S. Faci, C. Tripon-Canseliet, N. Guldner, G. Alquie, S. Formont, and J. Chazelas, "Photoconductive control of generated ultrashort microwave impulses," presented at 2007 International Topical Meeting Microwave Photonics, Victoria, BC, Canada, 2007.

[91] R. W. Klopfenstein, "A transmission line taper of improved design," *Proceedings of the Institute of Radio Engineers*, vol. 44, pp. 30-35, 1956.

[92] G. D. Vendelin, A. M. Pavio, and U. L. Rohde, *Microwave Circuit Design Using Linear and Nonlinear Techniques*. New Jersey: Wiley-Interscience, 2005.

[93] R. E. Collin, "The optimum tapered transmission line matching section," *Proceedings of the Institute of Radio Engineers*, vol. 44, pp. 539-548, 1956.

[94] M. Maeda, "An analysis of gap in microstrip transmission lines," *Microwave Theory and Techniques, IEEE Transactions on*, vol. 20, pp. 390-396, 1972.

[95] H. C. Huang, S. Yee, and M. Soma, "The carrier effects on the change of refractive index for *n*-type GaAs at λ=1.06, 1.3, and 1.55μm," *Journal of Applied Physics*, vol. 67, pp. 1497-503, 1990.

ATTENTION: The Singapore Copyright Act applies to the use of this document. Nanyang Technological University Library

[96] D. T. F. Marple, "Refractive index of GaAs," *Journal of Applied Physics*, vol. 35, pp. 1241-1242, 1964.

[97] J. Van Roey, J. van der Donk, and P. E. Lagasse, "Beam-propagation method: analysis and assessment," *Journal of the Optical Society of America*, vol. 71, pp. 803-10, 1981.

[98] S. Wicaksono, S. F. Yoon, W. J. Fan, and W. K. Loke, "The effect of rapid thermal annealing on GaAsSbN quantum-well and GaAsSbN bulk lattice-matched to GaAs," presented at 2005 International Conference on Indium Phosphate and Related Materials, Glasgow, Scotland, UK, 2005.

ATTENTION: The Singapore Copyright Act applies to the use of this document. Nanyang Technological University Library